Determination of Optimum Plate Heat Exchanger Geometry for OTEC Based on Net Power Maximization

March 2022

Department of Science and Advanced Technology
Graduate School of Science and Engineering
Saga University

Fontaine Kevin Davy - Erik

Table of contents

List of figures

List of tables

Acknowledgments

First, I would like to express my gratitude to my supervisor Professor Yasuyuki Ikegami for giving me the opportunity to fulfill this work. I am thankful for all the advice, guidance and encouragements he provided me throughout these three years.

I would like to thank the members of my committee Professor Yuichi Mistustake, Professor Yoichi Kinoue and Associate Professor Hirofumi Arima for the advice and constructive remarks regarding my thesis and for the time and effort spend for its evaluation.

I am also thankful to Associate Professor Takeshi Yasunaga for his time and understanding, for all the constructive discussions, and for his numerous advice, whether it be related to my work or daily life in Japan.

I would also like to thank Associate Professor Takeshi Akinaga from Akita University for sharing his knowledge during our various meetings.

How not to mention my parents, in Reunion Island, without whom I would not be where I am today. Their financial and moral support has been extremely helpful in fulfilling my ambition.

My thanks also go to my friends; those I met in Japan and those living in France or Reunion island, for all the moments spent together. Their friendship was a great source of support during these years and this work would not have been possible without them.

I am grateful for all those who participated in the achievement of this work, whether it be from an academic perspective or as an essential personal support.

Finally, this work would not have been possible without the funding from the Science and Technology Research Partnership for Sustainable Development (SATREPS), and the Japan International Cooperation Agency (JICA) (grant number JPMJSA1803).

Nomenclature

A	Heat transfer area (m^2)
A_i	Interfacial area (m^{-1})
B	Constant ($m^2K.W^{-1}$)
Bd	Bond number (-)
Bo	Boiling number (-)
C	Capacity rate($J.m^{-3}.K^{-1}$), Coefficient (-)
Co	Convection number (-)
C_{wl}	Wall lubrication coefficient (m^{-1})
c_p	Specific heat at constant pressure ($J.kg^{-1}.K^{-1}$)
D	Diameter (m)
d	Constant (-)
d_q	Diameter (m)
f, f	Friction factor(-), bubble departure frequency (s^{-1})
F	Force density ($N.m^{-3}$)
g	Gravitational acceleration ($m.s^{-2}$)
G	Mass flux ($kg.m^{-2}.s^{-1}$)
h	Enthalpy ($J.kg^{-1}$)
$\bar{\bar{I}}$	Identity matrix (-)
Ja	Jacob number (-)
k	Turbulent kinetic energy ($J.kg^{-1}$)
K	Interphase momentum exchanger coefficient ($kg.m^{-3}.s^{-1}$)
L	Plate length (m)
L_{heat}	Latent heat ($J.kg^{-1}$)

m	Mass flow rate ($kg.s^{-1}$)
$\dot{m}$	Mass exchange rate ($kg.m^{-3}.s^{-1}$)
n	Coefficient (-)
N_b	Active nucleation site density (m^{-2})
P	Pressure (Pa)
Pr	Prandtl number (-)
Q	Heat (W)
Q_{pex}	Intensity of heat exchange ($W.m^{-3}$)
q	Heat flux ($W.m^{-2}$)
R	Interaction force between two phases ($N.m^{-3}$),
R_c	Minimum cavity radius (m)
$R_{fouling}$	Thermal resistance due to fouling ($m^2K.W^{-1}$)
r	Displacement vector (m)
s	Specific entropy ($J.kg^{-1}.K^{-1}$)
S	Cross surface area (m^2)
t_p	Plate thickness (m)
T	Temperature (K)
U	Overall heat transfer coefficient ($W.m^{-2}.K^{-1}$) Time average component of the velocity ($m.s^{-1}$)
v	Velocity ($m.s^{-1}$)
V	Volume (m^3)
w	Power per unit of heat transfer area ($W.m^{-2}$)
W	Gross power output (W)
Wi	Width (m)
x	Vapor quality (-)

α, α	Heat transfer coefficient ($W.m^{-2}.K^{-1}$), phase volume fraction (-)
β	Chevron angle (°)
γ	Coefficient (-)
δ	Mean channel spacing (m)
Δ	Difference operator
ε	Heat exchanger efficiency (-)
η	Efficiency (-)
θ	Contact angle (°)
Θ	Coefficient (-)
κ	Bulk viscosity (Pa.s)
λ	Conductivity ($W.m^{-1}.K^{-1}$)
Λ	Corrugation pitch (m)
μ	Viscosity (Pa.s)
ξ	Coefficient (-)
Π_k	Source term in the turbulence transport equation ($W.m^{-3}$)
Π_k	Source term in the turbulence transport equation ($kg.m^{-3}.s^{-2}$)
ρ	Density ($kg.m^{-3}$)
σ	Surface tension (N/m)
σ_k	Turbulent Prandtl number relative to k (-)
σ_ω	Turbulent Prandtl number relative to ω (-)
τ	Plate shear stress (Pa), stress-strain tensor (-)
ϕ	Enlargement factor (-)
ψ	Scalar placeholder (-)
ω	Turbulence dissipation rate (s^{-1})
Ω	Coefficient (-)

Subscripts

b	Boiling
c	Condenser
c_0	Cell 0
c_1	Cell 1
cen	Centered
cr	Critical
conv	Convection
d	Downstream
D	Drag
dis	Distorted
e	Evaporator
eff	Effective
evap	Evaporation
eq	Equivalent
f	Working fluid, face
g	Given
grav	Gravitational
h	Hydraulic
in	Inlet
LMTD	Logarithmic Mean Temperature Difference
l	Liquid
lo	Liquid only
m	Homogeneous

max	Maximum
out	Outlet
p	Plate, phase p
P	Pump
part	Particle
proj	Projected
q	Phase q
r	Received
sca	Scaled
T	Turbine
td	Turbulent dispersion
u	Upstream
v	Vapor
vis	Viscous
w	(Sea)water
wall	Wall
wl	Wall lubrication
ω	Vorticity

Chapter 1.

INTRODUCTION

Ocean Thermal Energy Conversion (OTEC) is a technology allowing power generation from the natural temperature gradient in the ocean. It consists in a heat engine using the warm surface seawater heated by solar radiation as a heat source, and the cold deep seawater as a cold sink. OTEC power plants can produce energy steadily throughout the year as the temperature of the warm seawater hardly changes in suitable areas, which are tropical seas. Therefore, OTEC has a big advantage compared to other renewable energies already introduced in today's energy mix, which are highly intermittent. In addition to power generation, OTEC produces cold deep seawater as a byproduct that has many uses, such as refrigeration, aquaculture, agriculture, cosmetics and in desalination facilities. Due to its high potential, which was estimated at 7TW of net energy production

(Rajagopalan & Nihous, 2013b), as well as the different by-products it can provide, OTEC is likely to hold a major role in the future economy and energy mix, and can help reaching energy goals for many countries throughout the world.

The concept of OTEC was first briefly discussed by Jacque-Arsène d'Arsonval in 1881 as one of the possible way of harvesting natural energy (d'Arsonval, 1881). First experiments were conducted by George Claude. He started from a demonstration, using two rather small containers filled with warm water and ice in 1926, to a successful on-land experiment in Cuba in 1930, although he only managed to produce 22kW for about 100kW of pumping power. He then tried to transform a cargo into an off-shore power plant that failed due to mechanical damage from the sea in 1935. From there, different experiments and projects were conducted around the world, especially starting from the 1970's. Particularly, in 1979, the first closed cycle OTEC power plant to generate a net power output – about 18kW – was constructed and operated for three months. In 1981, the first OTEC power plant to actually provide electricity to another facility was deployed. For about a year, a school in the Republic of Nauru was supplied in electricity by this power plant (Takahashi, 2000).

Figure 1-1:Mini-OTEC (1979).
source: www.otecnews.org.

In 2013, a 50kW – upgraded to 100kW in 2016 - demonstration power plant was constructed on the island of Kumejima in Japan by Okinawa prefecture.

Figure 1-2: 100 kW power plant in Kumejima: source: http://otecokinawa.com/jp/index.html.

One significant difference compared with the previous power plants is that the deep seawater used by the power plant can be used by many industries on site, which benefits local economy. Indeed, the annual deep seawater related business in the island represents about 20 million USD. (Martin et al., 2016; *Utilizing deep sea water*, 2017).

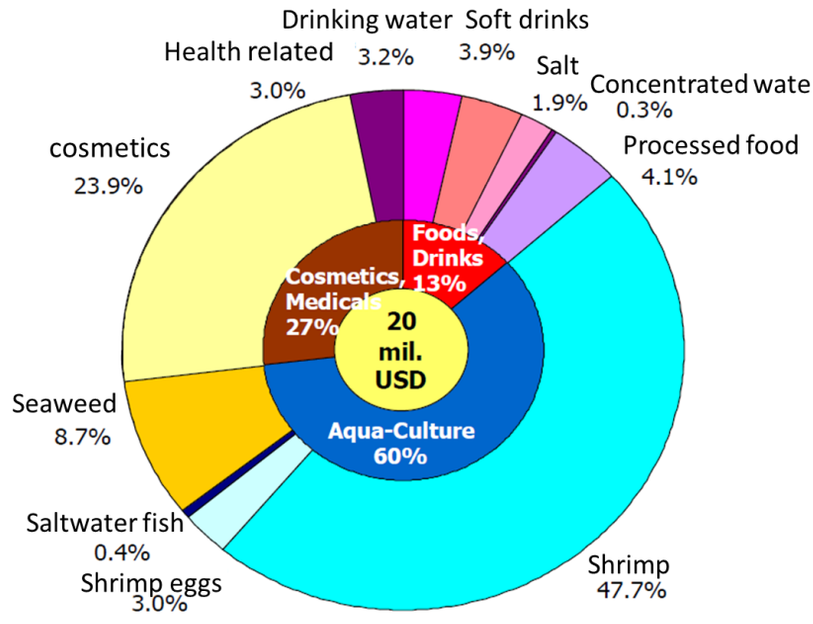

*Figure 1-3: Deep seawater related business (***Utilizing deep sea water***, 2017).*

Another successful project has been carried out in Hawaii, where a 105 kW OTEC power plant was connected to the grid in 2015 and is able to supply enough energy for around 120 homes, and a project to construct a 1MW off shore power plant has also been proposed (*Makai Ocean Engineering*, n.d.).

Figure 1-4: Makai OTEC power plant in Hawaii.
Source: https://www.makai.com/ocean-thermal-energy-conversion/

More projects have been proposed or are currently under construction, however the power plants in Kumejima and Hawaii are the two currently operating power plant with the highest power generation capacity.

Despite these installations, OTEC system is yet to be mature and many challenges still exist, especially for high capacity power plants. As an example, the 10 MW "NEMO" OTEC pilot power plant which was supposed to be operational by 2020 (Roche, 2018) is currently on hold due to the difficulty of manufacturing a 1000 meter long pipe with a 6 meter diameter that can withhold extreme meteorological conditions (*ETM : La centrale NEMO*, 2018).

1.1. OTEC working principles

In today's OTEC projects and experiments, three main different cycle can be observed, which have their own advantages and drawbacks.

1.1.1. The open cycle

The open cycle is derived from George Claude's experiments. In this cycle schematized in Figure 1-5, surface seawater is directly pumped into a vacuum chamber called flash evaporator where the low pressure causes seawater to evaporate. The steam is then extended through a turbine linked to a generator before being condensed using deep seawater. A great advantage of this cycle is the desalinated surface seawater that is generated as a byproduct. However, this cycle only works at low pressure, which implies the use of a large turbine, as well as a vacuum pump for the flash evaporator. Also, the non-condensable gases present in the seawater can decrease the system efficiency (Amano & Tanaka, 2006). These gases need to be expulsed from the system to ensure normal operation.

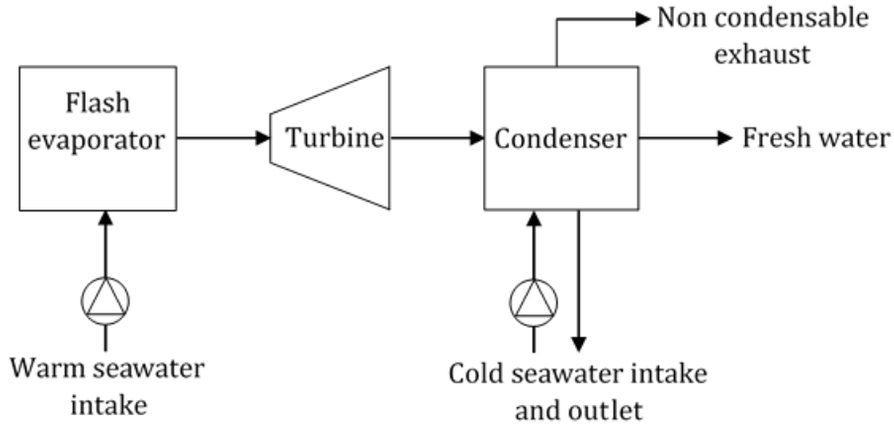

Figure 1-5: Schema of an open cycle OTEC power plant.

1.1.2. The closed cycle

Figure 1-6 shows how a closed cycle OTEC system operates; a low boiling point working fluid, such as ammonia, is heated in a first heat exchanger in which it evaporates. The resulting vapor is then used to operate a turbine before being condensed by the deep sweater through a second heat exchanger. Finally, the working fluid is pumped back into the evaporator for another cycle. This cycle operates at higher pressure, which allows for the use of a smaller turbine.

However, fresh water is not being produced by this cycle, as there is no seawater evaporation.

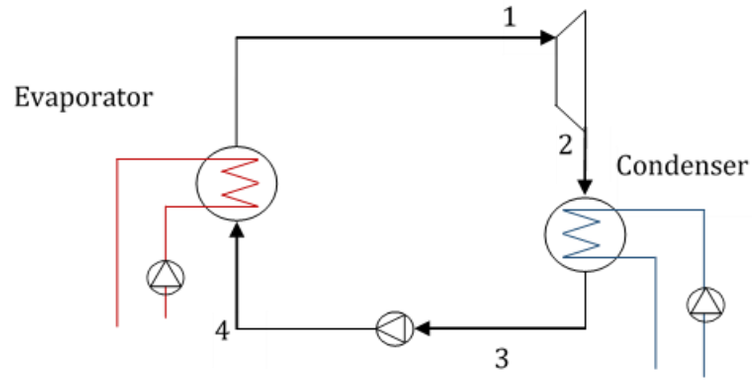

Figure 1-6: Schema of a closed cycle OTEC system.

1.1.3. Hybrid cycles

Two main hybrid cycles are investigated. The first one consists in evaporating the discharged warm seawater from a closed OTEC cycle and using the discharged cold seawater to condense the resulting vapor. This requires additional power, but allow both water desalination and the use of a high pressure system.

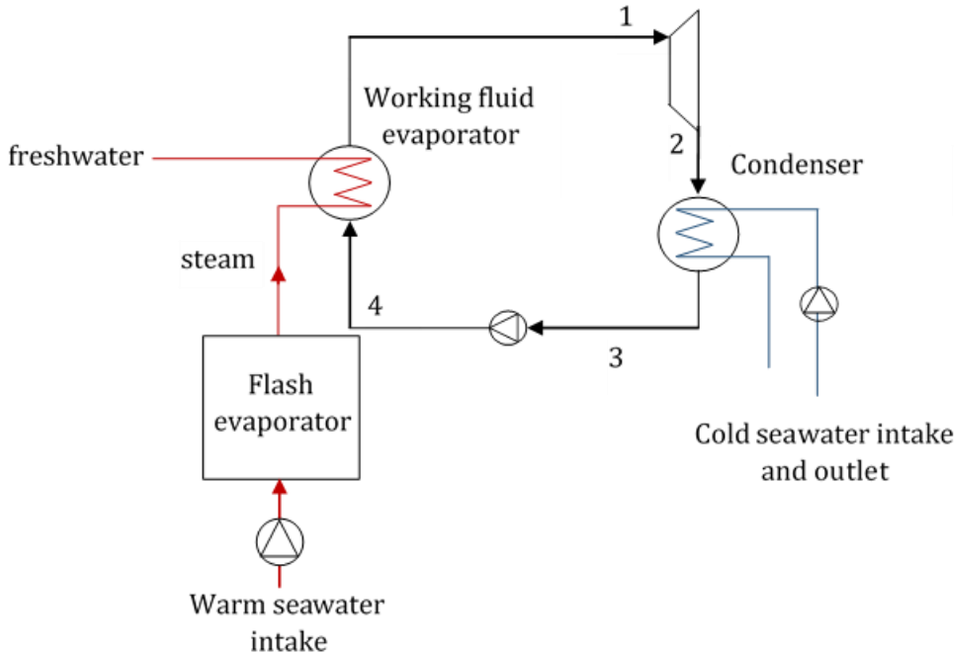

Figure 1-7: Schema of a hybrid cycle OTEC system.

The other hybrid cycle is shown in Figure 1-7. The surface warm seawater is introduced into a flash evaporator the exact same way as for the open cycle. Then, the vapor is used in a heat exchanger to heat a low boiling point working fluid,

which evaporates, whereas the seawater vapor condensates, thus, producing freshwater. As for the closed cycle OTEC system, the resulting working fluid vapor is used to operate a turbine and is then condensed in a second heat exchanger by the cold deep seawater. In addition to the freshwater production, the heat exchange with the working fluid in the evaporator is increased compared with the one in a closed cycle, due to the seawater phase change.

The freshwater produced by a hybrid or open cycle OTEC can be used in agriculture or to produce hydrogen by electrolysis as a mean to store the energy generated by the power plant. Indeed, as these installations can be implemented on an offshore boat or platform, especially for high power facilities, energy storage and/or transportation are essential.

1.1.4. Thermal efficiency

As a heat engine, the thermal efficiency of an OTEC system is dependent on the difference between the heat source temperature, $T_{we,in}$, and the cold sink temperature, $T_{wc,in}$, which is relatively low in the sea. The standard theoretical maximum yield for a heat engine is given by Equation (1-1):

$$\eta = 1 - \frac{T_{wc,in}}{T_{we,in}} \qquad (1\text{-}1)$$

Assuming a surface seawater of 30°C and a deep seawater of 5°C, this maximum theoretical efficiency only reaches 8%. However, a previous study showed that the temperature difference between warm and cold seawater is almost equally divided into two parts; one that induces a pressure difference between the evaporator and the condenser, and the other that causes a high heat transfer rate between the working fluid and both warm and cold seawater (Chih Wu, 1987). As only the pressure difference plays a role for the power generation, the maximum theoretical yield is decreased to 3.5 to 6% (Avery & Wu, 1994; Bernardoni et al., 2019). In conventional thermal power plant, the fuel being rather expensive, a high yield is required to extract the maximum power from a finite amount of fuel. However, in case of an OTEC power plant, there are no fuel cost involved, except from the seawater pumping power, which significantly lower the importance of the efficiency defined in Equation (1-1). It can be more important, in an OTEC system, to focus on the net power output defined as:

$$W_{net} = W_{gross} - W_{elec} \quad (1\text{-}2)$$

Where W_{elec} is the total power used to operate the power plant. Nonetheless, because of the low efficiency, and its dependency on the temperature difference between the surface and deep seawater, OTEC system can only be operated in tropical areas. The map in Figure 1-8 presents the temperature gradient within the ocean and the suitable locations for OTEC power plants. The higher the temperature difference, the higher the power output.

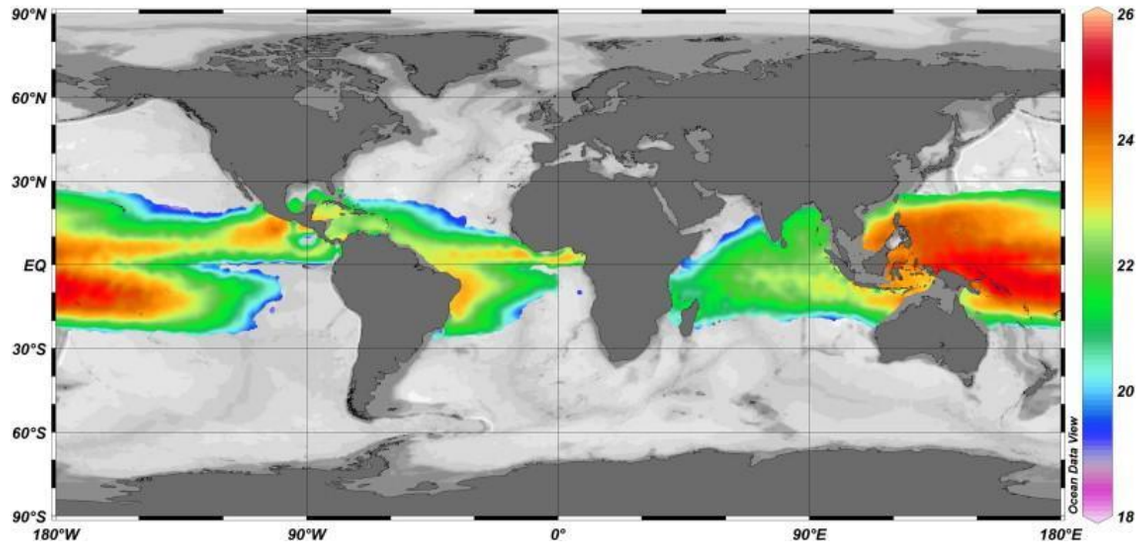

Figure 1-8: World map of annual average temperature gradient (between 20m and 1000m). (Rajagopalan & Nihous, 2013a)

1.2. Heat exchangers

A heat exchanger is a device that allows the transfer of heat from one fluid to another, either by direct contact for immiscible fluids, or by indirect contact for miscible fluids. In OTEC, the working fluid is usually miscible with seawater that is used as heat source and cold sink, and, due to environmental impact the working fluid can have, any leaking or mixing with seawater have to be avoided. Therefore, only indirect contact heat exchangers can be used. Many categories of indirect heat exchangers exist for many different applications; for OTEC, plate heat exchangers present the advantage of being highly compact, thus, reducing the amount of space needed to reach the high heat transfer surface area required by the power plant. This can result in a significant cost reduction, especially for off-shore installations. A plate heat exchanger, as shown in Figure 1-9, consists in a stack of plates between which warm and cold fluids circulate alternatively, and where the heat

transfer occurs. These plates are made in a material with a high conductivity, and usually presents some sort of surface treatment to improve the heat exchange, such as corrugated pattern or fins.

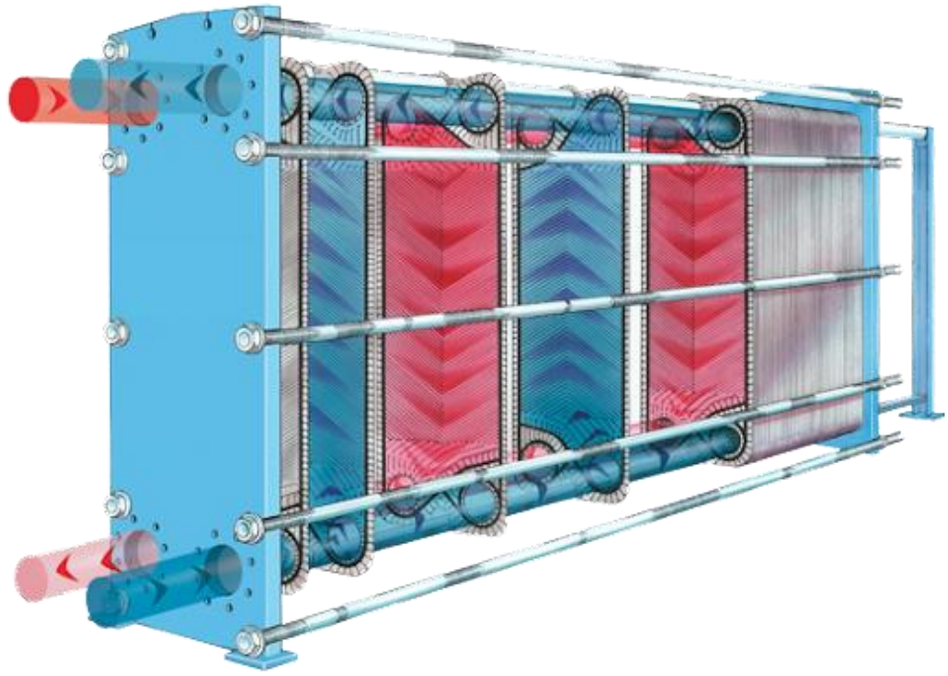

Figure 1-9: Representation of a plate type heat exchanger.

*(***AREVA NP et Tranter, Inc. associent leur expertise pour le remplacement des échangeurs thermiques dans les installations nucléaires.***, 2017)*

In case of a corrugated pattern, the plate is defined by its length, L, width, Wi, corrugation angle, β, corrugation pitch, Λ, and mean channel spacing, δ, which are shown in Figure 1-10 and Figure 1-11 . The performance of a heat exchanger, i.e. the heat transfer performance and the pressure drop, are usually assessed experimentally, and correlations for the Nusselt number and friction factor are given for each heat exchanger.

Both these parameters are interdependent; increasing the heat transfer coefficient requires an increase of the turbulence inside the heat exchanger, which also results in an increase of the pressure drop. Due to the low thermal efficiency of OTEC, these parameters must be carefully considered, as the gross power output and the electrical power required to counteract the pressure drop can be of the same order of magnitude.

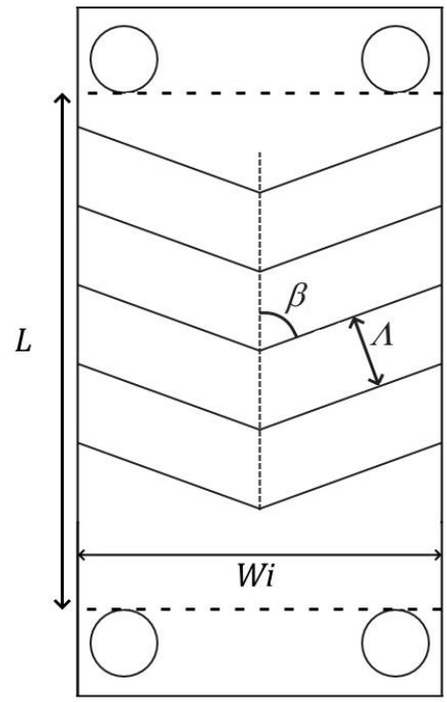

Figure 1-10: Representation of one plate of a heat exchanger.

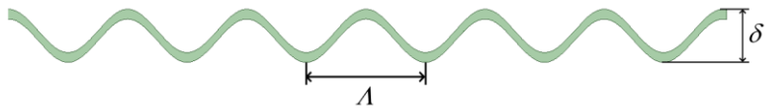

Figure 1-11: Side view of one plate of a heat exchanger.

1.3. Computational Fluid Dynamics

CFD is a useful tool that focuses on modelling all sorts of flow and heat transfer within a specified geometry. It consists in numerically solving the Navier-Stokes equations in a volume defined by a mesh of small elements. The general flow of a CFD study starts with creating the geometry, usually through a computer-aided design (CAD), then the volume defined by the geometry is divided in a mesh of small elements using a meshing software, before being translated for the CFD software itself, in which the relevant models, assumptions, and boundary conditions are set. The equations are then solved through an iterative process until it reaches convergence.

CFD can be very accurate if the model is well defined. However, a trade-off must usually be found between result accuracy and computational time. This is achieved by using simplified models and assumptions. Another important element is the mesh size. Indeed, a very fine mesh usually leads toward a more accurate solution, but at the cost of computational time.

The main advantage of using CFD is that, once the model has been validated, time consuming and highly expensive experimentations are no longer required to predict a flow pattern, with or without heat transfer. Therefore, using CFD it is theoretically possible to compute the heat transfer performance and pressure drop that occur within a heat exchanger. However, although rather simple one phase flow can be modelled using any CFD software, phase-change heat transfer, as it happens in OTEC, is still actively investigated and no clear consensus have been pointed out. The main reason is that most models and closure models are based on experimental data and correlations, which have limited applications. Thus, the importance of model validation against experimental data or other validated models.

There are two main ways of modelling a two-phase flow (Ansys®, 2018b):

- The Euler-Lagrange approach in which a main fluid is computed through Navier-Stokes equations and a secondary phase consists in a large number of dispersed bubbles throughout the main fluid. However, this is inappropriate when high volume fraction is reached, which happens in boiling heat exchangers used for OTEC.
- The Euler-Euler approach in which both phases are taken as interpenetrating continua and volume fraction is considered. In this approach, a set of conservation equations is solved to model each phase. More closure models, however, are required.

  Among the Euler-Euler approach, three main models exist (Ansys®, 2018b):

- The Volume of Fluid model in which both fluid share the same set of momentum equations, and the interface between the two phases is

tracked through the volume fraction. This model is used when the main focus of the computation lies in the two fluids' interface.

- The mixture model in which the momentum equation is solved for the mixture and relative velocity is used for the secondary (dispersed) phase.
- The Eulerian-Eulerian model in which momentum and continuity equations are solved for both phases. Continuity between the two phases are ensured through pressure and interphase exchange coefficients.

In case of OTEC heat exchangers, suitable models are the mixture model and the Eulerian – Eulerian model.

1.4. Literature review

1.4.1. OTEC cycles

In his work, Johnson (1983) compared the performance of different OTEC cycles and combination of cycles. He ranked different OTEC cycle according to their second-law efficiency defined as the actual work to seawater exergy ratio. According to his findings, the cycle that has the potential to extract the most energy from a finite quantity of seawater is the triple stage open Rankine cycle, whereas the closed Rankine cycle is the worse. He also compared the second-law efficiency of the closed Rankine cycle – about 32% – with the one of a coal-fired power plant – about 36% – and concluded that an "OTEC power plant uses the exergy of the ocean thermal resource as efficiently as a conventional coal-fired plant uses the exergy of coal." His ranking, however, does not take into account the power required to operate each cycle, meaning that, although he did identify the triple stage open Rankine cycle as the one that would extract the most part of the seawater exergy, and, therefore, the one that would lead to the highest gross power output, results might be different in terms of net power output as the power consumption for each cycle is different. Moreover, in this analysis, the temperature difference within both heat exchanger is assumed to be 2K rather than computed for more accuracy.

Although Johnson concluded that the Rankine open cycle had the best potential regarding seawater exergy use, it was shown that the closed cycle led to

a higher net power output. Indeed, in their work, Seungtaek et al. (2020) assessed the economic feasibility of single and double stage open cycles, as well as single stage closed cycle OTEC power plants in different suitable areas. First, they compared the gross power output, power consumptions, and, in case of open cycles, freshwater production in each region by applying the same design conditions. Their results showed a higher gross power output for the open cycle but also a higher power consumption due to the vacuum pump, inducing a higher net power output for the closed cycle. The double stage open cycle was found to lead to an even lower net power output, although it resulted in a significant increase in the freshwater production. It was also found that the amount of produced freshwater decreased as the surface seawater temperature increased. Then, they compared OTEC systems of 1, 10 and 50 MW at the different locations in terms of benefits to cost ratio, net present value, and internal rerun rate. Best indicators were achieved for different cycles, depending on the electricity and water price of each location. However, it was found that, as the power rating of the system increased, the proportion of closed cycles presenting the highest economic indicators increased as well. If their work allows great insight in OTEC system design, in their power analysis, the same conditions were applied for each site rather than optimized ones. Indeed, depending on the site and cycles, the net power output changes from one design to another. Moreover, in their economic analysis, the annual operating cost was assumed to be 5%, rather than computed based on an assessment of the power consumption of the system, meaning that the difference in operating power might not have been captured properly.

One of the other OTEC cycles, schematized in Figure 1-12, is the Kalina cycle, which introduce the regeneration of the working fluid (Kalina Alexanfer I., 1982). It uses a non-azeotropic mixture of ammonia and water as the working fluid that first evaporates using the heat of the warm seawater in the evaporator, resulting in an ammonia rich vapor which expands through a turbine to generate electricity. Then, this vapor goes into the a recuperator where it is cooled down before being mixed with a low ammonia concentration solution, thus, raising the condensation temperature. This mixture goes into the absorber before being divided into two different flow; the major part of the flow is directed through the recuperator and

then the separator, whereas the rest is mixed with the separator to dilute the rich ammonia vapor at its outlet. The mixture finally goes into the condenser before being pumped back to the evaporator. The use of a non-azeotropic mixture leads to a decrease of the irreversible losses in the heat exchanger and, therefore, to a better thermal efficiency.

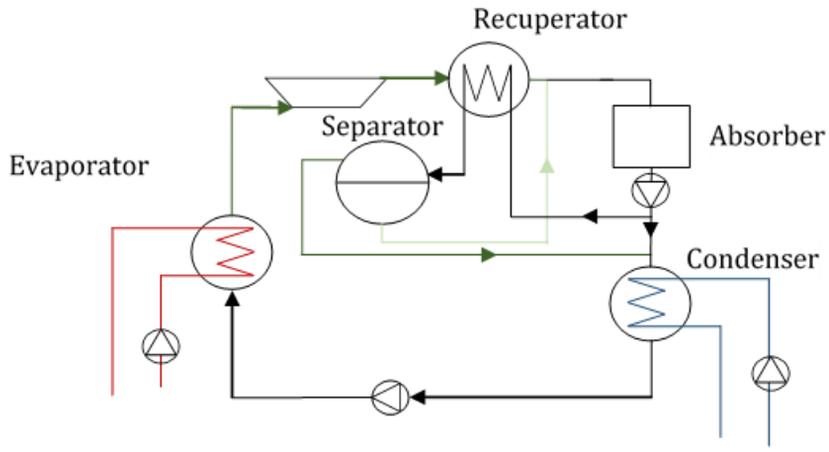

Figure 1-12: Schematic drawing of a Kalina cycle.

A comparison of the Kalina cycle with the closed Rankine cycle as well as a review of the research on the former cycle has been realized by Zhang et al. (2012). They found this cycle to be an improvement compared to the Rankine cycle in most cases, especially for low temperatures. However, these low temperatures that were reported remained significantly higher – around 100°C – than the temperatures at OTEC conditions. The Kalina cycle was improved by Uehara et al. (1995) who managed to increase the thermal efficiency of the cycle by around 10%, notably by including a second turbine, in order to reduce the condenser heat load. The cycle they invented was then referred to as the Uehara cycle.

Although those cycles do lead to an increase in the cycle thermal efficiency, it has been shown that the use of a non-azeotropic mixture leads to a decrease in the heat transfer coefficient, and, therefore, the amount of heat that can be harvested from a given quantity of seawater. Indeed, Anowar Hossain et al. (2013) investigated the evaporation heat transfer of a mixture of R1234ze(E) and R32 in a horizontal tube, and found that the heat transfer coefficient was higher than the one of R1234ze(E) for low vapor quality but lower as the vapor quality increases. Compared to R32, the mixture heat transfer coefficient was lower on the whole vapor quality range. Azzolin et al., (2017) realized a similar study on the

condensation heat transfer of the same mixture, and concluded that the heat transfer coefficient was lower when using non-azeotropic mixture, although the gap between the mixture and pure fluids tend to decrease as the vapor quality is low. Because of this decrease in the heat transfer coefficient, further study to clarify whether the increase in the efficiency achieved using non-azeotropic working fluids is enough to overweight the decrease in the heat transfer coefficients.

As an alternative to reduce the irreversible losses, Ikegami et al. (2018) investigated the multistage Rankine cycle and compared its performance with the single stage Rankine and Kalina cycles. By computing the maximum utilizable power, they confirmed the decrease in the irreversible losses using the double stage and Kalina cycles over the single stage Rankine cycle. They found these two cycles to achieve a higher power output than the single stage Rankine cycle. The Kalina cycle was found to lead to a slightly higher power output than the double stage Rankine cycle, and authors concluded that, due to the lower heat transfer coefficient when using non-azeotropic mixtures, the double stage Rankine cycle would be preferred. It should be noted, however, that the pressure loss of all fluids in the heat exchangers were neglected, therefore, only a comparison of the gross power output was achieved, and results considering the net power output might differ from one cycle to another. Specifically, with an additional cycle, the gross power output, power consumption and power plant price increase, therefore, it is still yet to know if the increase in the gross power output is greater than the combined increased pumping power and price. Moreover, the actual heat transfer coefficient was not computed in their study, thus, it is still unclear whereas which of the double stage Rankine cycle and Kalina cycle would be more appropriate.

Table 1-1 summarizes the different research investigating the OTEC cycles.

Table 1-1: Summary of research on OTEC cycle.

Authors	Achievements summary	Unsolved issues
Johnson, (1983)	Realized the ranking of different cycles in terms of their second law efficiency and identified the triple stage open cycle as the one with the more potential and the single stage closed Rankine cycle as the worse one.	The temperature difference in both heat exchangers is assumed to be 2 K rather than being computed. Moreover, the ranking in terms of second law efficiency do not identify which cycle presents the highest net power output as the power consumption depends on the cycle
Seungtaek et al., (2020)	Compared open and closed cycles at different locations and found that the closed cycle OTEC presents a higher net power output. Also compared cycles using different economic indicators which showed a tendency of the closed cycle to present a higher economical value as the power plant capacity increases. At low capacity, open cycles were found to be more attractive due to the freshwater production.	In the thermodynamic analysis, the same conditions were applied at each site rather than optimal ones. The economic analysis did not account for the actual operating power, as the annual operating cost was assumed to be equal to 5% of the capital cost.

Authors	Achievements summary	Unsolved issues
Kalina Alexanfer I., (1982)	Proposed a new cycle using non-azeotropic working fluid which decreased the irreversible losses, leading to a better cycle efficiency.	The use of non-azeotropic working fluid decreases the heat transfer coefficient within the heat exchanger.(Anowar Hossain et al., 2013; Azzolin et al., 2017) It is unclear whether the increase in the cycle efficiency is enough to overweight the decrease in the heat transfer coefficient.
Zhang et al., (2012)	Realized a review of different research on the Kalina cycle and compared its efficiency with the Rankine cycle leading to the confirmation of the increase in thermal efficiency using the Kalina cycle.	The investigated temperatures were mostly higher than OTEC conditions.
Uehara et al., (1995)	Proposed a new cycle as an improvement of the Kalina cycle by introducing a new turbine to decrease the condenser heat load, leading to a further increase in the cycle efficiency.	As for the Kalina cycle, further analysis are required to as the increase of the thermal efficiency is achieved at the cost of a decrease in the heat transfer coefficient.
Ikegami et al., (2018)	Identify the double stage Rankine cycle as almost as efficient as the Kalina cycle and confirm the thermal efficiency increase of those cycles compared to the single stage Rankine cycle.	The pressure drop of both fluids in the heat exchangers were not considered and the actual heat transfer coefficients were not computed, therefore, the cycle leading to the highest net power output could not be identified.

1.4.2. Working Fluid

The ideal working fluid used in the heat exchanger to extract and released the heat from and into the seawater must meet certain conditions in terms of environmental impact, security, and thermodynamic properties. Dijoux et al. (2017) conducted an investigation to find which fluid would be the most suitable for OTEC. They concluded that ammonia, R507a and R1234yf are suitable working fluid, although no fluid could meet all condition. In their study, Bernardoni et al. (2019) also found ammonia to be a suitable working fluid.

1.4.3. OTEC optimization and heat exchangers

In OTEC, many studies identify heat exchangers as one of the key elements of the system to investigate.

Sinama et al. (2015) investigated the minimization of the destroyed exergy in each component of an OTEC cycle, and, thus, identified the flow pump and heat exchangers as ideal target for optimization. They also realized an optimization of the cycle in terms of heat exchanger pinch, heat exchanger efficiency and warm seawater temperatures in order maximize the net power output and exergy efficiency. They found that these two targets would lead to different optimum parameters, and stated that the maximization of the net power output would be preferable. However, in their analysis, the overall heat transfer coefficient was assumed rather than computed, which is likely to lead to a lower accuracy in the power output calculation. Moreover, an optimization of the heat exchanger pitch or heat exchanger efficiency does not easily translate into an optimum heat exchanger geometry as both the pinch and the efficiency depends on several flow variables.

Sun et al. (2012) proposed an optimization design of the Rankine cycle in which the enthalpies are computed from the working fluid state points of the cycle. For an arbitrary fixed value of the product of the overall heat transfer coefficient and heat transfer area, they could derive the optimum saturation temperature that maximize the power generated by the cycle. They concluded that the power generated by the cycle was mainly a function of the inlet seawater temperatures, warm seawater mass flow rate, and heat exchangers performances. However, the overall heat transfer coefficient being assumed rather than computed, coupled

with the fact that the only considered pumping power was due to the pressure difference between the working fluid at the evaporator and condenser, thus, not including pressure drops within the heat exchangers, their optimization fails to capture the trade-off that exist between the heat transfer coefficient and pressure drop and might lead to thinking that the heat exchanger with the highest heat transfer coefficient would be the most suitable.

Bernardoni et al. (2019) realized an optimization of an OTEC power plant to maximize the net power output to heat transfer area ratio. Thus was realized according to the warm seawater temperature difference at the inlet and outlet of the evaporator, the cold seawater temperature difference at the inlet and outlet of the condenser and both heat exchangers pinch points. They analyzed different working fluids and identified ammonia as the most suitable one for OTEC. They then computed the Levelized Cost Of Energy (LCOE) of the resulting power plant, defined as the ratio between the sum of the operating cost over its lifetime and its capital cost, and its net energy production over its lifetime. Using these two analysis, they could identify heat exchangers not only as the components in which most of the exergy is destroyed, but also as the most expensive ones. However, their optimization does not give clear insight regarding which heat exchanger would be optimum for OTEC, and the LCOE was based on thermodynamic optimization results rather than using the LCOE directly as the objective function, which would be more accurate.

Due to the interdependency between the heat transfer coefficient and pressure drop, it is required to compute the net power output of an OTEC power plant for different heat exchangers in order to choose those that will be used. In their OTEC performance evaluation of a Carnot cycle based on finite-time thermodynamics (FTT), Yasunaga et al. (2018) identified the theoretical relationship between heat transfer performance, pressure drop and OTEC net power output, and that a compromise must be found to achieve a higher net power output. This implies the necessity of knowing both the heat transfer performance and pressure drop of a heat exchanger, which can be found in the literature (Morisaki & Ikegami, 2013; Nilpueng & Wongwises, 2010; Solotych et al., 2016). They also proposed a performance index evaluation for OTEC system based on a

Carnot cycle, allowing for a comparison of the cycle performance using different heat exchangers of known characteristics. However, the overall heat transfer coefficient as well as pressure drop were approximated using an exponential function with coefficients that depends on each heat exchanger, and experimental data are required for fitting purposes. Moreover, the net power evaluation does not reflect real conditions as only the Carnot cycle was investigated.

In their in-depth optimization of a closed-cycle OTEC power plant for different temperatures, Uehara & Ikegami (1990), minimized the cost of the produced electricity based on an objective function defined as the ratio between the heat transfer area and the net power output. Their method accounts for the majority of the significant parameters, which are, the working fluid pressure difference between the evaporator and condenser, as well as its pressure drop within the condenser and pipes, the seawater pressure drop within both heat exchangers and pipes, the heat transfer coefficients of the working fluid and seawater in both the evaporator and condenser, and the computation of the turbine efficiency based on the turbine parameters. They could compute the optimized net power output and operating condition for a power plant of a given capacity for a specific set of heat exchangers, including the required heat transfer area. However, their method does not include the working fluid pressure drop within the evaporator and presents the drawback of being highly computer expensive due to the high number of iteration processes implied.

Wu et al. (2019) investigated the minimization of the required pumping power of an evaporator for OTEC based on constructal theory. They used a dimensionless pumping power, defined as the ratio between the plate pumping power at the considered optimization parameters and plate initial pumping power as the objective function and heat transfer rate as a constraint. Their optimization was realized in respect to the chevron angles, corrugation pitch, effective volume as well as heat transfer width and length of the plate and was applied for different working fluids. However, their method does not focus directly on increasing the net power output of the OTEC system, even though the heat rate is included as a constraint. As pumping power decrease, the heat transfer coefficient is likely to decrease as well, which might lead to a lower net power output.

Wu, Feng, Chen, & Ge (2020) realized an optimization of the condenser, still based on constructal theory. They used a composite function of the entropy change rate and pumping power as the objective function to account for both the heat transfer coefficient and pressure drop. They used number of active plates as well as heat transfer length and width as optimization parameters, and investigated the effect of chevron angle, corrugation pitch, and effective volume on this composite function. However, the optimum values also depend on the weighting coefficient of the composite function which need to be assessed correctly. Moreover, the condenser is investigated as an isolated component rather than part of the OTEC whole system.

Finally, Wu, Feng, Chen, Tang, et al. (2020) realized the constructal thermodynamic optimization of an OTEC system operating under the dual pressure Rankine cycle. They used the net power output as the objective function, and investigated plate heat transfer length of all components, the volume fraction of the high pressure turbine, as well as the heat transfer area fractions of the condenser and high temperature evaporator. They also investigated the effect of the working fluid mass flow rate, mean vapor fractions, turbine wheel diameter ratio as well as seawater inlet temperature on the system. They compared their results with what was obtained for a single pressure system, and concluded that the dual pressure Rankine cycle would lead to a higher power output. However, the optimization of the net power output does not account for the expensive cost of the heat exchangers, i.e., although a maximized net power output is obtained, this might not be preferable if it results in a larger, and thus more expensive, heat exchanger. Moreover, they did not investigate the effect of plate parameters such as chevron angles, corrugation pitch, or mean channel spacing.

Table 1-2 summarizes different studies regarding heat exchangers in OTEC cycles.

Table 1-2: Summary of studies regarding OTEC cycles.

Authors	Achievements summary	Remaining issues
Yasunaga et al., (2018)	Proposed a performance index evaluation for OTEC system based on a Carnot cycle allowing for heat exchanger comparison after deriving the theoretical relationship between net power output, heat transfer coefficient and pressure drop.	The overall heat transfer coefficient and pressure drop are approximated using exponential functions and require experimental data. Real cycles are not investigated.
Sinama et al., (2015)	Identified flow pumps and heat exchangers as components that require optimization and realized an optimization of the OTEC cycle in terms of heat exchanger pinch point, heat exchanger efficiency and warm seawater temperature.	The overall heat transfer coefficient is assumed rather than computed and the optimization parameters cannot be easily used for heat exchanger choice or design parameter.
Sun et al., (2012)	Proposed an optimization design of the Rankine cycle relying on the computation of the different cycle states, and derived the optimum saturation temperatures that maximize the net power output.	The overall heat transfer coefficient was assumed rather than computed, the pressure drop within the heat exchangers were not computed and the optimization of the saturation temperatures did not give insights on the choice or optimum design of the heat exchangers.

Authors	Achievements summary	Remaining issues
Bernardoni et al., (2019)	Realized a thermodynamic optimization of an OTEC cycle in terms of seawater temperature difference along the heat exchangers and heat exchangers pinch point, and proceeded to compute the LCOE of the resulting power plant, which helped identify heat exchangers as a the component that requires optimization the most.	The thermodynamic optimization do not give clear insight on the choice or optimum design of heat exchangers, and the LCOE was based on a the thermodynamic optimization rather than being used as the objective function.
Uehara & Ikegami, (1990)	In depth OTEC optimization resulting in accurate results for a given gross power output and given heat exchangers, for which mass flow rates, heat transfer areas, temperatures, and turbine parameters are computed.	Experiments are required to derive heat transfer coefficient and pressure drop correlations, and the optimization includes several iterative steps making the optimization process highly expensive in terms of computation time. Moreover, the pressure drop within the evaporator is not computed.

Authors	Achievements summary	Remaining issues
Wu et al., (2019)	Realized the minimization of the evaporator pumping power using constructal theory, and considering chevron angles, corrugation pitch and effective volume	The evaporator is considered as a standalone component rather than included in an actual cycle, and the heat transfer coefficient is not well accounted for.
Wu, Feng, Chen, & Ge, (2020)	Performed the optimization of a condenser for OTEC based on constructal theory, and using a composite function as the objective function, allowing for the investigation of heat exchangers design parameters.	The condenser is considered as a standalone component rather than included in an actual cycle, and the composite function does not represent well the system behavior, notably because of the weighting coefficient involved.
Wu, Feng, Chen, Tang, et al., (2020)	Realized the thermodynamic optimization of OTEC net power output of a dual pressure system in terms of plate lengths, heat transfer area fraction, and volume fraction of high pressure turbine.	The net power output is maximized without any consideration for the actual required heat transfer area, and the effect of heat exchanger design parameters were not investigated.

1.4.4. Flow boiling Computational Fluid Dynamics

As research on phase-change is a major subject to itself, in this thesis, only the boiling heat transfer coefficient is investigated. Many authors investigated flow boiling in the literature, using different geometries and different fluids.

Li et al., (2006) modified the two-fluid (Euler-Euler) method implemented on CFX-4.3 to compute the flow boiling of nitrogen in a vertical tube based on the RPI wall boiling model. They changed the way bubble diameter was computed as well as some closure parameters, such as the nucleation site density or the ratio between the area around the nucleation site affected by quenching and the bubble projected area at bubble departure. They could improve the overall model accuracy and pointed out that phase-change models are highly sensitive to the active nucleate site density closure model. Namely, they noticed an increase in their model accuracy using the Kocamustafaogullari – Ishii model instead of the Lemmert and Chwala model.

Krepper & Rzehak (2011) simulated the DEBORA experiments (Garnier et al., 2001; Manon, 2000) to check the applicability of CFD to subcooled wall boiling flow and identify weaknesses. They compared their simulations in terms of wall superheat, gas fraction, velocities, liquid temperature and bubble size. They confirmed the potential of the Eulerian – Eulerian model although it requires some closure parameters that can have a significant impact on the simulation results. This is mainly due to the fact that most closure models are based on experimental correlations.

Končar & Matkovič (2012) realized an analysis of the flow boiling of HFE-301 in a vertical rectangular channel with one heated wall based on the RPI model, and found good agreement with experiments for the parameters linked to the heat flux and Reynolds variation but an over prediction of the turbulence when using the SST k-ω model along with the Sato model.

Yun et al. (2012) combined Klausner et al.'s (1993) force balance model for bubble departure size and Hibiki & Ishii's model (2003) for active nucleation site in their simulation of R12 flow boiling inside a pipe. They proposed a new velocity wall function, which require the use of two empirical coefficients to improve

turbulence modelling in a heated pipe. Like Krepper & Rzehak (2011), they used the DEBORA experiments as a reference for their calculations (Garnier et al., 2001; Manon, 2000). Results were compared in terms of local void fraction, bubble velocity and diameter, phase velocity, and temperatures.

Yeoh et al. (2014) realized an evaluation of the RPI wall boiling model for an annular geometry using water to find that it can predict the volume fraction and bubble sauter diameter distribution accurately but not the heat flux partitioning, which is the principle of the RPI model.

Nemitallah et al. (2015) investigated water flow boiling characteristics, namely the wall temperature, void fraction, average temperature, vapor phase velocity, heat transfer coefficient and mass transfer rate for a heating pipe with a non-uniform heat flux. They showed that a non-uniform heat flux distribution lead to a modification of the heat transfer coefficient and void fraction distribution.

Braz Filho et al. (2016) conducted a study to predict subcooled flow boiling characteristics for water in a vertical tube using two-fluid Eulerian model in Fluent. When comparing vapor quality, liquid bulk temperature, and wall temperature to the experimental data from Bartolemej & Chanturiya (1967), they concluded that CFD is a promising tool to characterize subcooled flow boiling although void fraction was under predicted by the model they used.

Colombo & Fairweather (2016) assessed the accuracy of CFD models in terms of vapor quality, vapor velocity, liquid temperature profile and Sauter mean diameter using a large number of experimental data points from different studies in the literature. They pointed out the principal drawback of such models; the high dependency on experimental closure models, which makes it difficult to predict boiling flow characteristics for a wide range of experiments using the exact same model. Despite the need of improvement in modelling some of the phenomenon, they also confirmed the potential of CFD in the prediction of such multiphase flow.

Gilman & Baglietto (2017) proposed a more complete mechanistic model for water boiling phenomena, which was lacking in previous models, and obtained a more robust and more accurate model. They also realized a sensitivity analysis showing that the bubble frequency is the parameter that need to be accurately

assessed. They used the data for a vertical rectangular duct from Phillips (2014) as reference in their calculations.

Thakrar et al. (2017) realized a blind comparison of different model combinations using default values and no "posteriori user calibration". Calculation were realized on a rectangular duct geometry using water on the code STAR-CCM+. They showed that if the more mechanistic model combination is able to accurately predict the mean void fraction, no model combination could lead to an acceptable prediction on a local scale, leading to a failure to capture a change in the flow pattern.

Colombo et al., (2019) compared three force balance model for the prediction of bubble departure diameter required for the RPI wall boiling model. The study was based on water and R12 in a vertical pipes using STAR-CCM+ code. Comparison was realized based on bubble departure diameter, wall temperature, bubble departure frequency, void fraction and heat fluxes. They showed that models taking the contact diameter as a fraction of the bubble diameter instead of a constant led to more accurate result.

Table 1-3 summarizes different CFD flow boiling studies.

Table 1-3: Summary of flow boiling CFD studies.

Author	Title	Geometry	Phase change model	Heat flux	Achievement summary
Li et al., (2006)	Nitrogen	Vertical tube. L = 220 mm D = NS	CFX: Eulerian RPI wall boiling model Modified k-ε (Sato)	Uniform	Improvement of model accuracy by changing bubble diameter equations as well as closure models such as nucleation site density and quenching affected site to projected bubble area ratio. Namely, the closure model of Kocamustafaogullari – Ishii seemed to provide a better accuracy.
Krepper & Rzehak, (2011)	R12	Pipe D_{in} = 19.2 mm L = 5m Heated length = 3.5m Manon(2000), Garnier et al. (2001)	CFX Eulerian RPI wall boiling model k-ω SST	Uniform	Confirmed the great potential of CFD but identify closure models as a significant weakness as it is based on experimental correlations and therefore need to be adapted to each simulation.
Končar & Matkovič, (2012)	HFE-301	Vertical rectangular channel 530 x 8.7 x 7.6 mm heater 175 x 7 mm	CFX Eulerian RPI wall boiling model k-ω SST	Uniform	Found good agreement for parameters linked to heat flux and Reynolds variation using the k – ω SST model along with the Sato model despite an over prediction of the turbulence.

Author	Title	Geometry	Phase change model	Heat flux	Achievement summary
Yun et al., (2012)	R12	Pipe D_{in}: 19.2 mm L = 5m Heated length = 3.5m See Garnier et al (2001).	Star-CD Eulerian RPI wall boiling model k-ε	Uniform	Combined Klausner's force balance model for bubble departure size diameter with Hibiki and Ishii's model for active nucleation and proposed a new velocity wall function to improve turbulence modelling.
Yeoh et al., (2014)	Water	Pipes: D_{in} = 12.7/19mm D_{ext} = 24.5/37.5mm L= 306/1670mm	Multiple Size Group boiling model RPI boiling model	Uniform	Found the RPI wall boiling model to be unable to accurately predict the partition of heat transfer, despite being the model's principle. Nonetheless they could accurately predict the bubble sauter-diameter.
Nemitallah et al., (2015)	Water	Pipe : L = 2m D_{int} = 15.4mm D_{ext} = 25.4mm	Fluent Eulerian RPI wall boiling model k-ε	Uniform and non-uniform	Investigated the effect of a non – uniform heat flux and showed its impact in the heat transfer coefficient as well as vapor quality.
Braz Filho et al., (2016)	Water	Vertical tube : D = 15.4 mm L=2 m	Eulerian RPI wall boiling model k-ω SST	Uniform	Identified an under prediction of the vapor quality using the RPI wall boiling model, although they confirmed the potential of CFD for flow boiling applications.

Author	Title	Geometry	Phase change model	Heat flux	Achievement summary
Colombo & Fairweather, (2016)	R12 R113 Water	Multiple :Pipe, annular channel	Star CCM + Eulerian RPI wall boiling model Reynold stress model	Uniform	Investigated the accuracy of CFD models using a large number of experimental and pointed out the dependence on experimental closure models as a major drawback to predict flow characteristics for a wide range of experiments using the same model.
Gilman & Baglietto, (2017)	Water	Vertical rectangular: 1000 x 30 x 10 mm Heated surface: 20 x 10 mm	Star CCM+ Eulerian RPI wall boiling model Cebeci and Bradshaw (1977)	Uniform	Proposed a new mechanistic wall heat transfer framework to reduce the sensitivity to closure models and increase the accuracy and robustness. Identified the need of further improvement for bubble frequency

Author	Title	Geometry	Phase change model	Heat flux	Achievement summary
Thakrar et al., (2017)	Water	Vertical rectangular 1550 x 44.5 x11.1 mm Heated length: 1260mm	Star –CCM+ Eulerian RPI wall boiling model k-ε/RSTM	Uniform	Realized a blind comparison of different model combinations using default values and showed that mechanistic models provided better accuracy for mean vapor quality but failed at predicting local values, and thus, the change in flow pattern.
Colombo et al., (2019)	Water R12	2 vertical pipes: D = 0.0154/0.0192 m	Star CCM+ Eulerian RPI wall boiling model k-ε	Uniform	Compared three force balance models for the prediction of bubble departure diameter and found that models taking the contact diameter as a fraction of bubble diameter instead of a constant led to a better accuracy.

1.4.5. Conclusion

- Different cycles have been investigated previously. Although the open cycle is more efficient at harvesting seawater thermal energy, practically, its net power output is lower than the one of a closed cycle because of the required energy to operate the vacuum pump. The cycle choice should be different for each site depending on the location specific needs; the open cycle remains a relevant option where access to freshwater is a significant issue. Among the closed cycles, some attempt of increasing the thermal efficiency were made by introducing non-azeotropic mixtures, but doing so induced a decrease in the heat transfer coefficient within the heat exchangers. It was shown that the use of a double stage closed Rankine cycle could lead to a thermal efficiency comparable, yet somehow lower, to those using non-azeotropic mixtures without the drawback of lowering the heat transfer coefficient in the heat exchangers. No studies could clearly indicate which cycle would be more suitable for OTEC. A comparison between Kalina, Uehara, single Rankine, and multistage Rankine cycles in terms of net power output, taking into account the heat transfer coefficient as well as pressure drop is required.
- Studies that focuses only on the working fluid are scarce but identify ammonia as one of the most suitable working fluid and, as such, is the fluid of choice in this thesis.
- Heat exchangers were clearly identified as one of the key element in OTEC as it represents a significant part of the price, and has a significant impact on the net power output of the system. The heat transfer coefficient and pressure drop have been shown to be linked, and a balance between these two characteristics must be achieved to maximize the net power output of an OTEC power plant. For many studies, it was found that the heat transfer coefficient and pressure drop, if considered, were assumed or simplified rather than computed, leading to a lower accuracy in the power output assessment. Besides, economics analysis studies were scarce and did not use economic indicator as

objective functions. In-depth analysis can be found in the literature but appear to come with a high computational cost, and the development of a simpler method is required. Moreover, OTEC cycle optimization targeted values such as saturation temperatures, heat exchanger pinch points, heat exchanger efficiency, and seawater temperature difference along both heat exchangers. Only a few studies investigated heat exchangers geometry, and they either focus on isolated components, use strong assumptions, and/or do not consider all relevant design parameters. A method to derive an optimum heat exchanger geometry leading to the highest net power output to heat transfer area ratio is required for OTEC system design. Finally, studies that did compute, at least to some extent, heat transfer coefficients and pressure drops were found to highly rely on experimental correlations from the literature.

- Although numerous studies have been realized and are often based on the same general model, which is the RPI wall boiling model in a mixture or Eulerian – Eulerian approach, the use of empirical correlation as closure model implies a great variety of different possibilities in predicting heat transfer or flow characteristics when phase change is involved. Most studies focus on water flow boiling in a heating pipe or a vertical duct, however, no studies considering more complex geometry, such as chevron type heat exchangers, were found. Studies investigating ammonia flow boiling using CFD were not found either.

1.5. Research topics

Considering the previous research, it was found that the following topics still require investigations:

- Comparison of different cycles, including those using non-azeotropic working fluids in terms of net power output to heat transfer area ratio.
- Simplification of the optimization process and inclusion of heat transfer coefficients and pressure drops of both the seawater and working fluid.
- Optimization of heat exchangers' design parameters for a maximum power output to heat transfer area ratio.

- Optimization of the system with economic indicators as objective functions.
- Decrease the need for experiment for heat transfer coefficient and pressure drop correlations.

CFD appears to be a suitable tool for this last point. However, more research is required on the subject. Considering the previous research, main topics to investigate for OTEC are as follow:

- Ammonia flow boiling.
- Flow boiling in plate heat exchangers geometry.
- Flow boiling using non uniform heat fluxes.
- Improvement of the model accuracy, notably by reducing its dependency to closure models from experimental correlations.

1.6. Research objectives

A comparison using different cycles should be based systems operating at optimum parameters, as those parameters are likely to differ from one cycle to another. Moreover, optimization using economic indicators as objective functions should be performed once a thermodynamic optimization has been completed, and significantly vary on the power plant location. For these reasons, in this thesis, after this introduction, a second chapter is dedicated to the development of a simplified method for OTEC optimization based on both the Carnot and Rankine cycles, which allows for OTEC performance comparison using different heat exchangers. Results for the ideal and real cycles can also be compared. In this first chapter, the working fluid side is not considered by means of different assumptions, and seawater heat transfer coefficients and pressure drops are computed using heat exchanger specific correlations.

A third chapter focuses on the method accuracy improvement for the Rankine cycle by introducing the working fluid heat transfer coefficient and pressure drop in both heat exchangers. In this chapter, heat exchanger specific correlations are replaced by global ones to allow for the determination of plate heat exchangers optimal geometry to maximize the power plant net power output.

Finally, a fourth chapter demonstrate the possibility of using CFD to generate accurate flow boiling heat exchanger specific correlations to be used to improve the accuracy and possibilities of the optimization method. The demonstration is based on a vertical duct heated uniformly, using ammonia as a working fluid, as the change of fluid is believed to be the first step in the development of a complete simulation for the flow boiling of ammonia in an actual heat exchanger using non uniform heat flux.

Chapter 2.

OTEC CYCLE OPTIMIZATION

In this chapter, a method to compare a closed cycle OTEC system performance given its heat exchangers' specifications is introduced and showcased for three different heat exchangers for the Carnot and Rankine cycles.

2.1. Objective functions for OTEC

Prior to any computation, an objective function must be determined. This function will then be optimized in order to find its maximum. In OTEC, the net power output is equal to the difference between the gross power output generated by the turbine and the required power to operate the system. The seawater pumping power needed to ensure a sufficient flow rate within the heat exchangers is significant, and highly depends on the heat exchanger. This high pumping power is due to the pressure drop within the seawater pipes that lead the seawater

towards the heat exchangers, and the pressure drop within the heat exchangers themselves. In addition to seawater, the working fluid also circulates within the heat exchangers, and pumping is required to counteract the pressure drop that occurs.

In this chapter, the following assumption are considered:

- The heat transfer coefficient of the working fluid is much greater than the seawater one because of the phase change that occurs (Frank P. Incropera et al., 2006a).
- The thermal resistance due to fouling is negligible.
- The pressure drop on the working fluid side is negligible (Bernardoni et al., 2019; Sinama et al., 2015; Uehara et al., 1995).
- Seawater properties within a heat exchanger are taken constant and equal to the heat source or cold sink properties due to the low temperature difference at heat exchangers' inlet and outlet.
- Due to its rather low impact on the heat exchanger choice, the pressure drop occurring within the pipe, depending mainly on the pipe length, is not considered

2.1.1. Carnot cycle

In the ideal case of the Carnot cycle represented in Figure 2-1, the heat exchange is assumed to be isothermal, and both the compression and expansion processes are assumed to be isentropic, as depicted in Figure 2-2.

Considering this chapter's assumptions, the expression of the net power output generated by the OTEC system is given by Equation ***(2-1)***(Yasuyuki Ikegami & Adrian Bejan, 1998):

$$W_{net} = W_{gross} - W_P \qquad (2\text{-}1)$$

with W_P, the pumping power required to counteract the pressure drop occurring within the heat exchangers.

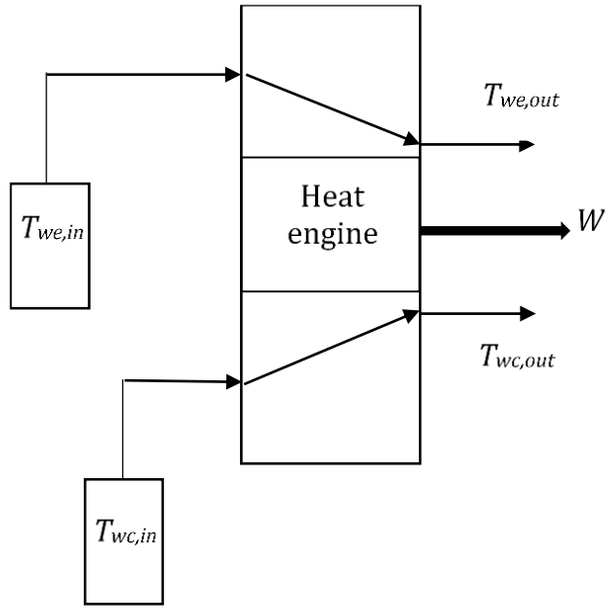

Figure 2-1: Model of the OTEC system.

The gross power output generated by the cycle is equal to the balance between the heat provided by the warm seawater, Q_e and the heat released into the cold seawater, Q_c, as defined in Equation (2-2) (Frank P. Incropera et al., 2006b):

$$W_{gross} = Q_e - Q_c = C_{we}\epsilon_{\mathrm{we}}\left(T_{we,in} - T_{fe}\right) - C_{wc}\epsilon_{\mathrm{wc}}(T_{fc} - T_{wc,in}) \qquad (2\text{-}2)$$

where ε is the heat exchanger efficiency equal to the ratio of the actual heat exchange and the maximum theoretical heat exchange for an infinite counterflow heat exchanger with no losses. C is the heat capacity rate, i.e. the product of the mass flow rate, m by the specific heat capacity c_p, and T refers to a temperature. Subscripts *w*, *f*, *e, c*, *in*, and *out* refer to the seawater, the working fluid, the evaporator, the condenser, an inlet and an outlet, respectively.

In both heat exchangers, the working fluid undergoes a phase change, thus, the efficiency can be expressed as in Equations (2-3) and (2-4): (Frank P. Incropera et al., 2006b)

$$\epsilon_{\mathrm{e}} = 1 - exp(-\mathrm{NTU_e}) \qquad (2\text{-}3)$$

$$\epsilon_{\mathrm{c}} = 1 - exp\,(-\mathrm{NTU_c}) \qquad (2\text{-}4)$$

with NTU, the number of transfer units defined as in Equation (2-5):

$$\mathrm{NTU} = \frac{UA}{C} \qquad (2\text{-}5)$$

where U is the overall heat transfer coefficient, and A is the heat transfer area of the heat exchanger.

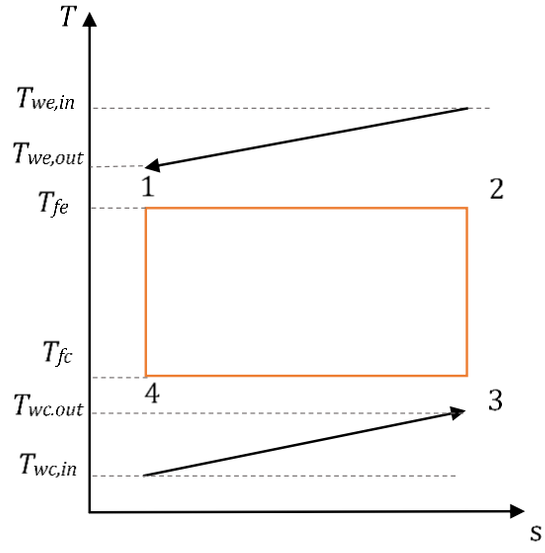

Figure 2-2: Temperature – entropy diagram of a Carnot cycle.

For heat exchangers of a given efficiency, it is possible to find the relation between inlet seawater temperatures and working fluid temperatures for which the gross power output is maximized using the Lagrange multiplier method as shown in Equation (2-6) to (2-9) (O. M. Ibrahim et al., 1992):

The constraint function shown in Equation (2-6) is the entropy balance, Δs, as it is null without irreversibilities:

$$\Delta s = \frac{C_{we}\epsilon_{we}\left(T_{we,in} - T_{fe}\right)}{T_{fe}} - \frac{C_{wc}\epsilon_{wc}\left(T_{fc} - T_{wc,in}\right)}{T_{fc}} = 0 \qquad (2\text{-}6)$$

The Lagrange multiplier Λ is then introduced and verifies Equation (2-7):

$$\frac{\partial W_{gross}}{\partial T_{fe}} = \Lambda \frac{\partial \Delta s}{\partial T_{fe}} \quad and \quad \frac{\partial W_{gross}}{\partial T_{fc}} = \Lambda \frac{\partial \Delta s}{\partial T_{fc}} \qquad (2\text{-}7)$$

Equations (2-2), (2-6) and (2-7) lead to the relationship in Equation (2-8):

$$\frac{T_{fc}}{T_{fe}} = \sqrt{\frac{T_{wc,in}}{T_{we,in}}} \qquad (2\text{-}8)$$

This is then introduced in Equation (2-2) to express the maximum power output the heat engine can generate as shown in Equation (2-9) (O. M. Ibrahim et al., 1992; Yasunaga et al., 2018; Yasuyuki Ikegami & Adrian Bejan, 1998):

$$W_{gross,max} = \frac{\left(\sqrt{T_{we,in}} - \sqrt{T_{wc,in}}\right)^2}{\frac{1}{C_{ws}\epsilon_{\mathrm{we}}} + \frac{1}{C_{ws}\epsilon_{\mathrm{wc}}}} \quad \textit{(2-9)}$$

Heat exchangers being one of the most expensive component of an OTEC system, in order to decrease the price of the power plant, it is more relevant to compare values of the maximum net power output divided by the heat exchanger surface area rather than the maximum net power output itself. Moreover, heat exchangers, including those for which this method is tested, have different surface area which, in case of plate heat exchangers, can be modified by the addition or subtraction of plates. Besides, a net power output normalized by the surface area lead to a more efficient comparison. Therefore, the objective function, derived from Equations (2-1) and (2-9), is expressed in Equation (2-10) as:

$$w_{net} = \frac{1}{(As_e + As_c)}\left(\frac{\left(\sqrt{T_{we,in}} - \sqrt{T_{wc,in}}\right)^2}{\frac{1}{C_{we}(1 - e^{-\mathrm{NTU_{we}}})} + \frac{1}{C_{wc}(1 - e^{-\mathrm{NTU_{wc}}})}} - W_{P_{we}} - W_{P_{wc}}\right) \quad \textit{(2-10)}$$

with *As,* the heat exchanger surface area defined as $As = LWi(plate\ number - 2)$. W_P is defined as in Equation (2-11):

$$W_P = \frac{2\mathrm{f}L\mathrm{Re}_{\mathrm{w}}^3\mu_w^3 S}{D_{eq}^4\rho_w^2\eta_{\mathrm{P,w}}} \quad \textit{(2-11)}$$

with D_{eq}, the heat exchanger equivalent diameter computed as twice the mean channel spacing δ, L, the length of the plate, $\eta_{\mathrm{P,w}}$ the seawater pumping power efficiency, and Re, the Reynolds number defined as:

$$\mathrm{Re}_{\mathrm{w}} = \frac{\rho_w v_w D_{eq}}{\mu_w} \quad \textit{(2-12)}$$

where ρ_w is the seawater density, v_w, the seawater mean velocity, and μ_w, the seawater dynamic viscosity. The friction factor, f, *i*s defined as

$$\mathrm{f} = \frac{\tau}{\frac{\rho_w v_w^2}{2}} \quad \textit{(2-13)}$$

with τ, the wall shear stress of the plate. In this chapter, however, the friction factor is computed using an experimental correlation of the from:

$$\mathrm{f} = \Omega \mathrm{Re}^{\xi} \tag{2-14}$$

with Ω and ξ two constants depending on the heat exchanger.

As shown in Equation (2-5), the NTU depends on the overall heat transfer coefficient *U*, which itself is a function of the plate thickness *t*, the resistance due to fouling, $R_{fouling}$, and both fluids heat transfer coefficients, α_w and α_f.

$$\frac{1}{U} = \frac{1}{\alpha_w} + \frac{t}{\lambda_p} + \frac{1}{\alpha_f} + R_{fouling} \tag{2-15}$$

The fouling part being neglected, and α_f being assumed to be much greater than α_w, it comes,

$$\frac{1}{\alpha_w} + \frac{t}{\lambda_p} + \frac{1}{\alpha_f} + R_{fouling} \approx \frac{1}{\alpha_w} + \frac{t}{\lambda_p} = \frac{1}{\alpha_w} + B \tag{2-16}$$

with B a constant equal to the ratio of the plate thickness over the thermal conductivity of the plate.

The seawater side heat transfer coefficient can be deducted from the Nusselt number, $\mathrm{Nu_w}$, which reflects the ratio between the convective heat transfer coefficient and its conductive component, and is defined in Equation (2-17):

$$\mathrm{Nu_w} = \frac{\alpha_w D_{eq}}{\lambda_w} \tag{2-17}$$

Similarly to the friction factor, the Nusselt number is calculated from an experimental correlation that depends on the Reynolds and Prandtl numbers:

$$\mathrm{Nu} = \mathrm{d}\mathrm{Re}^{\gamma}\mathrm{Pr}^{\mathrm{n}} \tag{2-18}$$

with d, γ, and n being coefficients specific to each heat exchanger. The Prandtl number, defined as the ratio between the kinematic viscosity and thermal diffusivity is given in Equation (2-19):

$$\mathrm{Pr} = \frac{\mu_w c_p}{\lambda_w} \tag{2-19}$$

Using Equations (2-5) and (2-16) to (2-19), the NTU can be written as:

$$NTU = \frac{UA}{C} = \frac{D_{eq}}{\mathrm{Re}\mathrm{Pr}\lambda_w S} \frac{A\mathrm{d}\mathrm{Re}^{\gamma}\mathrm{Pr}^{\mathrm{n}}\lambda_w}{D_{eq} + BA\mathrm{d}\mathrm{Re}^{\gamma}\mathrm{Pr}^{\mathrm{n}}\lambda_w} = \frac{\mathrm{d}\mathrm{Re}^{\gamma-1}\mathrm{Pr}^{\mathrm{n}-1}AD_{eq}}{\left(D_{eq} + BA\mathrm{d}\mathrm{Re}^{\gamma}\mathrm{Pr}^{\mathrm{n}}\lambda_w\right)S} \tag{2-20}$$

S being the total cross surface area of the heat exchanger.

Finally, using Equations (2-20) and (2-10), the objective function, equals to the net power output by unit of heat exchanger surface area can be expressed as in Equation (2-21).

$$w_{net} = \frac{1}{As_{ws} + As_{cs}} \left(\frac{\left(\sqrt{T_{we}} - \sqrt{T_{wc}}\right)^2}{\frac{1}{\left(\frac{\mathrm{RePr}\lambda S}{D_{eq}}\left(1 - exp\left(-\frac{\mathrm{dRe}^{\gamma-1}\mathrm{Pr}^{n-1}AD_{eq}}{(D_{eq} + BA\mathrm{dRe}^{\gamma}\mathrm{Pr}^{n}\lambda)S}\right)\right)\right)_{we}} + \frac{1}{\left(\frac{\mathrm{RePr}\lambda S}{D_{eq}}\left(1 - exp\left(-\frac{\mathrm{dRe}^{\gamma-1}\mathrm{Pr}^{n-1}AD}{(D + BA\mathrm{dRe}^{\gamma}\mathrm{Pr}^{n}\lambda)S}\right)\right)\right)_{wc}} - \left(\left(\frac{2\Omega\mathrm{Re}^{3+\xi}L\mu^3 S}{D_{eq}^4\rho^2\eta_{\mathrm{P,w}}}\right)_{we} - \left(\frac{2\Omega\mathrm{Re}^{3+\xi}L\mu^3 S}{D_{eq}^4\rho^2\eta_{\mathrm{P,w}}}\right)_{wc}\right) \right) \quad \textit{(2-21)}$$

The objective function, thus, only depends on the seawater inlet properties and temperatures. It is important to note that this function cannot precisely assess the actual net power output of a power plant as it is based on an ideal cycle. Although it is possible to introduce an irreversibility factor, which takes into account all source of irreversibilities in the system, such solution is not really practical due to the difficulty in estimating this factor. Another way is to proceed with the optimization using a real cycle such as the Rankine cycle.

2.1.2. Rankine cycle

In the Rankine cycle described in Figure 2-3, heat exchange is no longer isothermal and both compression and expansion processes induce a change in entropy, as shown in Figure 2-4. It is assumed, however, that the working fluid at the outlet of both heat exchangers are in a saturated state. For such a cycle, the net power output can be expressed as in Equation (2-22).

$$w_{net} = \frac{1}{A_e + A_c} \left(\underbrace{m_f(h_2 - h_3)}_{W_g} - \underbrace{m_f(h_1 - h_4)}_{W_{P,f}} - \left(\frac{2\Omega\mathrm{Re}^{3+\xi}L\mu^3 S}{D_{eq}^4\rho^2\eta_{\mathrm{P,w}}}\right)_{we} - \left(\frac{2\Omega\mathrm{Re}^{3+\xi}L\mu^3 S}{D_{eq}^4\rho^2\eta_{\mathrm{P,w}}}\right)_{wc} \right) \quad \textit{(2-22)}$$

With m_f, the mass flow rate of the working fluid, $W_{P,\mathrm{f}}$ the working fluid pumping power due to the pressure difference between the evaporator and condenser, and

h_1, h_2, h_3 and h_4 the specific enthalpy values of the corresponding points in Figure 2-3 and Figure 2-4. The specific enthalpy values at points 2 and 4 are assessed from the temperature at those points for a fluid in a saturated state using the software REFPROP (E. W. Lemmon et al., 2018).

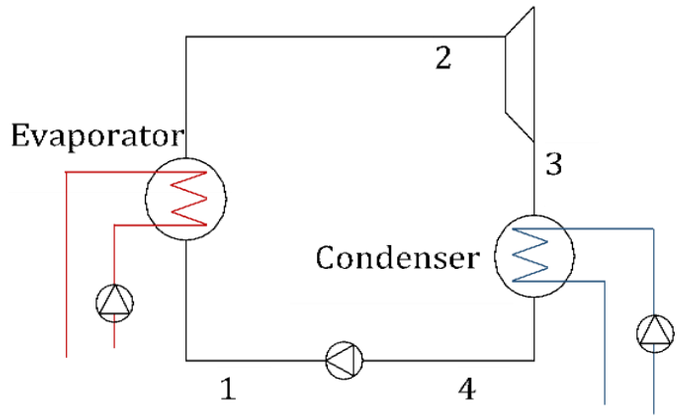

Figure 2-3: Description of the Rankine cycle.

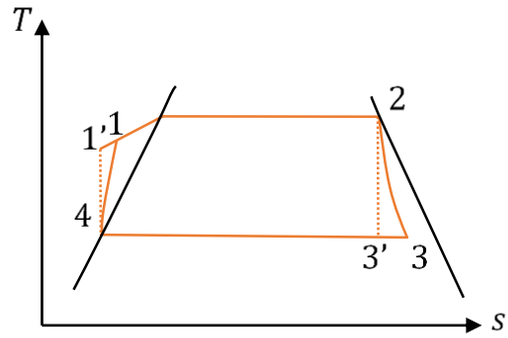

Figure 2-4: Temperature – entropy diagram of a Rankine cycle.

Then, enthalpies at points 1 and 3 are calculated using the working fluid pump and turbine efficiencies, respectively $\eta_{p,f}$ and η_t, according to equation (2-23):

$$h_3 = h_2(1 - \eta_T) + \eta_T h_3' \text{ and } h_1 = h_4 + \frac{h_1' - h4}{\eta_{p,f}} \qquad (2\text{-}23)$$

where h'_1 and h'_3 are the enthalpy values of the corresponding points in Figure 2-3 and Figure 2-4. These are calculated from REFPROP. For the point 3', the specific enthalpy value is computed at the temperature at point 4 and the entropy at point 2, as 3' is the result of an isentropic transformation from point 2. For point 1', both

the pressure at point 2 and entropy at point 4 are required and calculated from REFPROP using the corresponding temperatures and assuming a saturated state.

The saturation temperature in the condenser, $T_4 = T_3$, is derived from the following equality:

$$Q_{wc} = C_{wc}\left(T_{wc,out} - T_{wc,in}\right) = UA\underbrace{\frac{(T_4 - T_{wc,out} - (T_{wc.in} - T_4)}{ln\left(\frac{T_4 - T_{wc,out}}{T_4 - T_{wc,in}}\right)}}_{\Delta T_{LMTD}} \quad (2\text{-}24)$$

where ΔT_{LMTD} is the logarithmic mean temperature difference.

Thus,

$$UA\frac{T_{wc,in} - T_{wc,out}}{ln\left(\frac{T_4 - T_{wc,out}}{T_4 - T_{wc,in}}\right)} = -C_{wc}(T_{wc,in} - T_{wc,out}) \quad (2\text{-}25)$$

Therefore, using Equations (2-4), (2-5)and (2-25), T_4 can be deduced:

$$T_4 = \frac{T_{wc,in} - T_{wc,out}e^{\mathrm{NTU_{wc}}}}{\epsilon_{\mathrm{wc}}} \quad (2\text{-}26)$$

Using the same method applied to the saturation temperature in the evaporator, it comes:

$$T_2 = \frac{T_{we,in} - T_{we,out}e^{\mathrm{NTU_{we}}}}{\epsilon_{\mathrm{we}}} \quad (2\text{-}27)$$

2.2. Optimization process

Now that both objective functions have been expressed, it is possible to proceed with the optimization itself. For both cycles, optimization inputs remain the same i.e. inlet seawater temperatures and properties as well as heat exchanger specifications. Result for three versatile plate heat exchangers from Kushibe & Ikegami (2006) are studied and compared. Their specifications are given in Table 2-1.

The first plate heat exchanger (PHE 1) was designed for high pressure and temperature and is used as an evaporator in power generation based on hot springs, PHE 2 is a herringbone heat exchanger, and PHE 3 was invented by Prof. Uehara to be both a condenser and an evaporator (Kushibe & Ikegami, 2006).

Seawater properties are calculated at a salinity of 35 ppt and atmospheric pressure using the seawater properties Software developed by the Massachusetts Institute of Technology (2016), and based on the work presented by Sharqawy et al. (2010) and Nayar et al. (2016). A temperature sensitivity analysis is performed later on.

Table 2-1: Heat exchangers specifications.

Heat Exchanger	**PHE 1**	**PHE 2**	**PHE 3**
Length L (mm)	960	718	1 765
Width Wi (mm)	576	325	605
Thickness t (mm)	0.7	0.5	0.6
Mean channel spacing δ (mm)	4.00	3.95	2.68
Material	SUS316	Titanium	Titanium
Thermal conductivity λ_p ($W.m^{-1}.K^{-1}$)	16.3	21	21
Pattern	Herringbone (72°)	Herringbone (30°)	Fluting and drainage
Number of plates	120	20	52
Total heat transfer area A (m^2)	100.3	3.96	40.6
Total cross surface area S (m^2)	0.140	0.012	0.041
d (Nusselt correlation coefficient)	0.111	0.058	0.051
γ (Nusselt correlation coefficient)	0.8	0.8	0.8
n (Nusselt correlation coefficient)	1/3	1/3	1/3
Ω (friction factor correlation coefficient)	1.4863	6.5059	0.7371
ξ (friction factor correlation coefficient)	-0.0540	-0.3292	-0.1274

The optimization is run within Matlab R2019b (The MathWorks, Inc., 1990 - 2019) and is based on the SQP (Sequential Quadratic Programming) algorithm using the function "fmincon" (MathWorks®, n.d.). As the name implies, "fmincon," is an algorithm that search for the minimum of a given function, which, in this chapter is $-w_{net}$. To ensure that the result is indeed a global minimum and not a local one, calculations are performed for several starting point randomly

generated within the specified boundaries. Once the optimization is done, outputs are the maximum net power output to heat transfer area ratio and the set of variables for which such a maximum is reached.

2.2.1. Carnot cycle

As shown in Equation (2-21), the objective function for the Carnot cycle only depends on the seawater Reynolds numbers in the heat exchangers. These variables are limited so that the corresponding velocity remains between 0.2 m/s and 1.8 m/s; a range reachable in plate heat exchangers. Due to the relatively simple function formulation, no constraints are required for this cycle.

2.2.2. Rankine cycle

In addition to both seawater Reynolds numbers, the working fluid mass flow rate is also a variable in the Rankine cycle case. Moreover, contrarily to the Carnot cycle, seawater temperatures at heat exchangers' outlets are required when optimizing this cycle. They are introduced as variables in the optimization, raising the total of variables to five; $\mathrm{Re_{we}}$, $\mathrm{Re_{wc}}$, $T_{we,out}$, $T_{wc.out}$, and m_f. Temperature boundaries are taken between the inlet warm seawater temperature and the inlet cold seawater temperature, and the working fluid mass flow rate is limited to a value corresponding to a seawater velocity of 1.8 m/s.

For the working fluid properties, as calling the REFPROP library accounted for most of the computational time, polynomial correlations were interpolated using data from REFPROP within a range that cover OTEC operational conditions in terms of temperature.

Because of the introduction of three additional variables, two heat balance constraints – Equations (2-28) and (2-29) – are added to the optimization.

$$C_{ws}\left(T_{we,in} - T_{we,out}\right) = m_f(h_2 - h_1) \qquad \textit{(2-28)}$$

$$C_{cs}\left(T_{wc,out} - T_{wc,in}\right) = m_f(h_3 - h_4) \qquad \textit{(2-29)}$$

During the optimization, described in Figure 2-5, random initial values for the parameters are taken, then, evaporation and condensation temperatures are computed to allow for the assessment of the objective function, as well as the constraints violation. Next, the algorithm computes another set of variables in an attempt to decrease the objective function and/or the constraints violations.

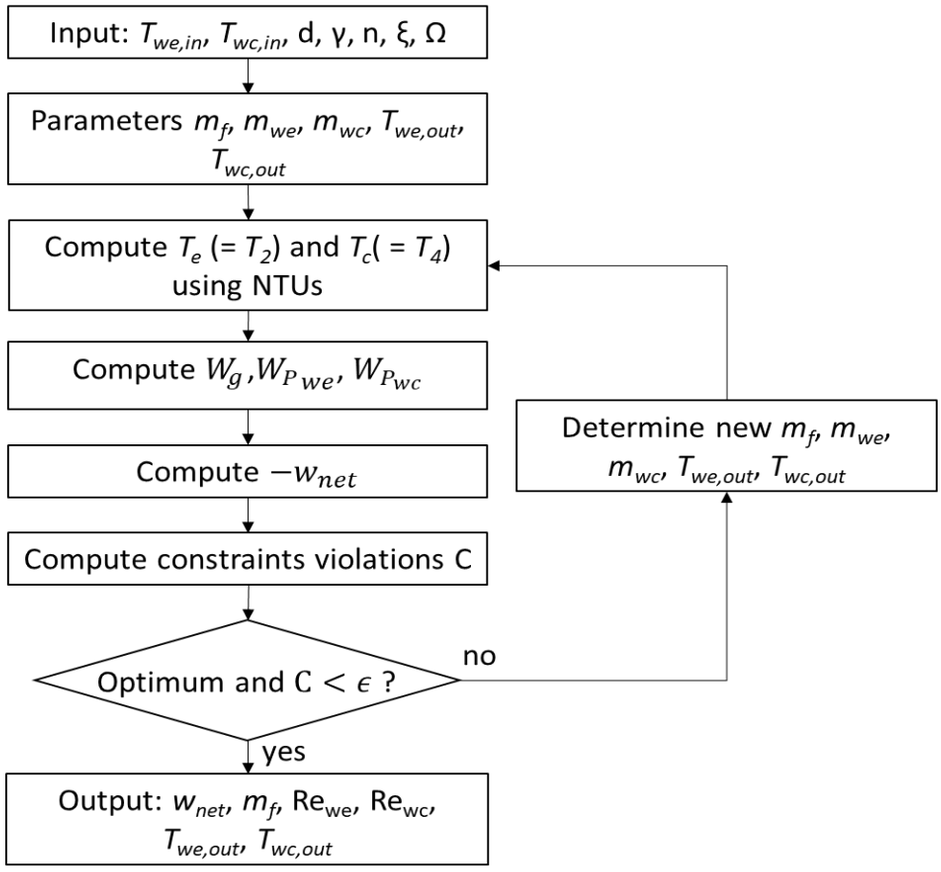

Figure 2-5: Flow chart of the optimization process for the Rankine cycle.

2.3. Comparison with standard method

Here, the method developed in the previous section is compared with a standard method from the literature, which is summarized in Figure 2-6 (Uehara & Ikegami, 1990). Once input data are provided, parameters are assessed, and used to compute the heat transfer area of both heat exchangers. The net power output is then computed, followed by the objective function given in equation (2-30).

$$\gamma = \frac{A_e + A_c}{W_{net}} \qquad (2\text{-}30)$$

As long as an optimum is not reach, new parameters are computed and the whole process starts again. This type of scheme is rather common in optimization processes. However, the complexity of the method comes from the computation of the heat transfer area, which is described in Figure 2-7 for the evaporator. The Figure 2-8 shows a representation of all the heat values that are used within the process.

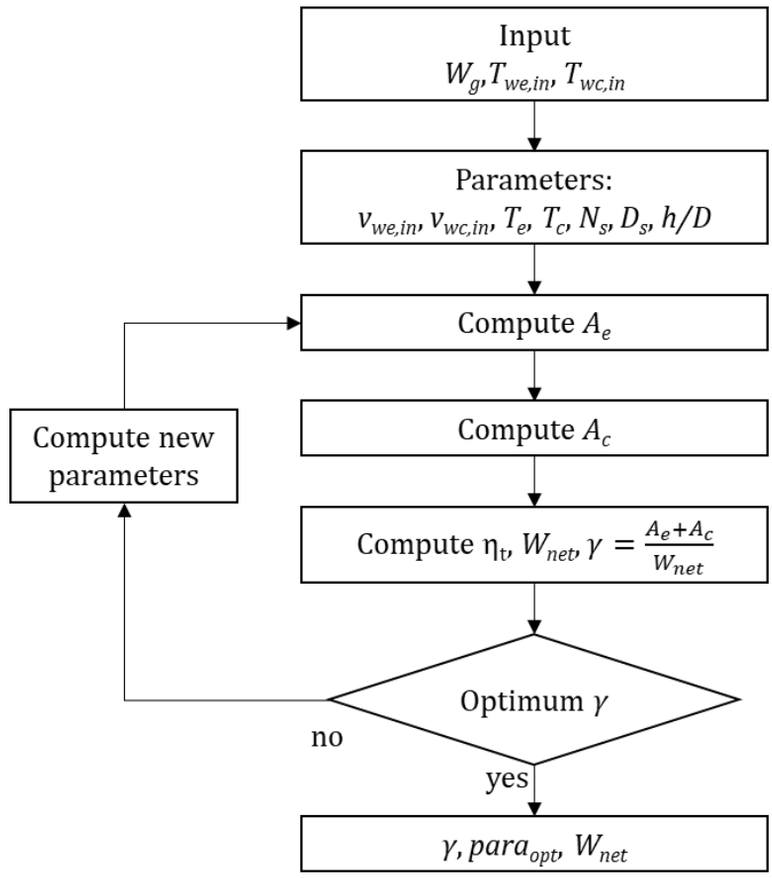

Figure 2-6: Flow chart of the method developed by Uehara & Ikegami (1990).
Ns, Ds, h/D are the turbine specific speed, specific diameter, and blade height to diameter ratio, respectively.

The working fluid side wall temperature, as well as the seawater outlet temperature are first assumed, and the heat transfer area is computed using Equation (2-31). Then, the heat received by the boiling working fluid Q_b, the heat through the plate Q_p and the heat due to convection on the seawater side, $Q_{we,conv}$ are computed. Next, the working fluid side wall temperature is modified until the equality between $Q_{we,conv}$ and Q_b is obtained. In a similar way, the seawater outlet temperature is changed until the equality between $Q_{we,conv}$ and Q_p is obtained. At each iteration where the seawater outlet temperature is modified, the process of computing the working fluid wall temperature according to $Q_{we,conv}$ and Q_b is once more required.

$$A_e = \frac{Q_{we,lost}}{U\Delta T_{LMTD}} \qquad (2\text{-}31)$$

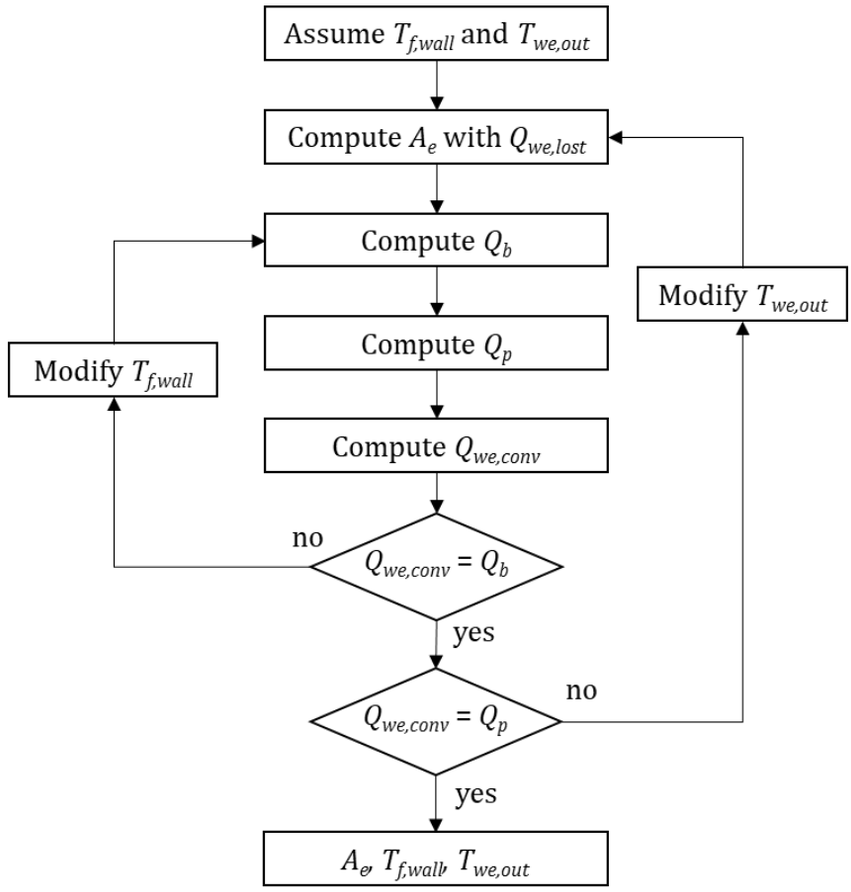

Figure 2-7:Flow chart of the heat transfer area computation process for the evaporator.

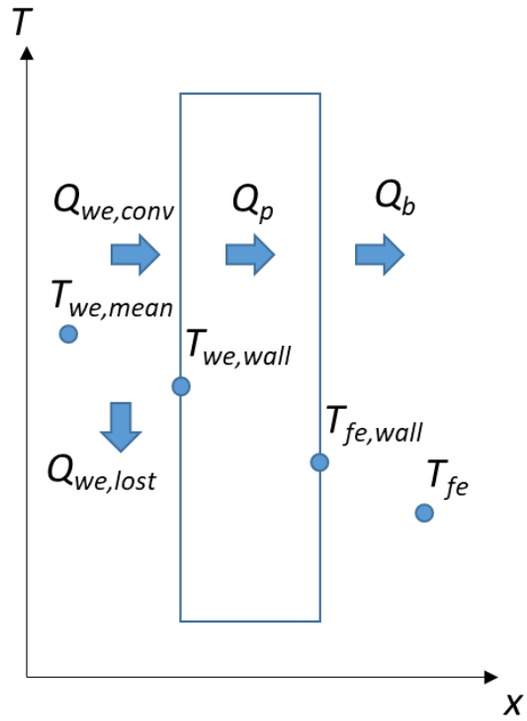

Figure 2-8: Representation of the heat flux involved in the heat transfer area computation process.

A similar process is used for the condenser, adding to the complexity and computational time required to perform the optimization. In comparison, the method developed in this chapter consists in the maximization of a single objective function that depends on two variables for the Carnot cycle, and the maximization of an objective function depending on five variables and subject to two constraints for the Rankine cycle. In each iteration, the objective function and constraints are only computed once before different parameters are assessed. The fact that the required temperatures are introduced as parameters and controlled through constraints functions rather than being assumed and modified as it is the case in the method from Uehara & Ikegami (1990), further decreases the required computation time.

2.4. Optimization Results

2.4.1. Carnot cycle results

After optimization, the normalized net power output w_{net} is plotted as a function of both Reynolds number in Figure 2-9, Figure 2-10, and Figure 2-11. Heat transfer coefficients, friction factors, pressure drops, pumping powers, and mass flow rates are summarized in Table 2-2.

Although these results cannot predict the net power output of an actual OTEC power plant nor the optimum parameters, as it is based on an ideal Carnot cycle and as the pressure drop within the pipes are neglected, results show that, for a wide range of Reynolds numbers, the net power output can easily reach a negative value. The Reynolds number range for such an outcome is even wider in an actual power plant, which shows how critical the choice and control over the seawater mass flow rate are. Indeed, depending on which heat exchanger is used, the net power output can be very sensitive to a change in Reynolds numbers. According to Figure 2-9 and Figure 2-10, although it is not the heat exchanger leading to the maximum net power output, PHE 2 is by far less sensitive to a Reynolds number variation, and can be preferred in case Reynolds numbers cannot be fixed or controlled easily.

Table 2-2: Seawater heat transfer coefficients, friction factors, pressure drops, and mass flow rates inside the heat exchangers.

	PHE 1	PHE 2	PHE 3
α_{we} (kW/m²·K)	18.01	11.46	9.717
α_{wc}(kW/m²·K)	12.75	8.102	6.849
f_{we} (−)	0.833	0.327	0.248
f_{wc} (−)	0.868	0.402	0.269
ΔP_{we} (kPa)	112.6	53.98	111.6
ΔP_{wc} (kPa)	116.7	66.36	120.0
W_{Pwe} (kW)	11.46	0.613	3.78
W_{Pwc} (kW)	11.81	0.751	4.030
m_{we} (kg/s)	104.0	11.61	34.57
m_{wc} (kg/s)	104.0	11.63	34.52

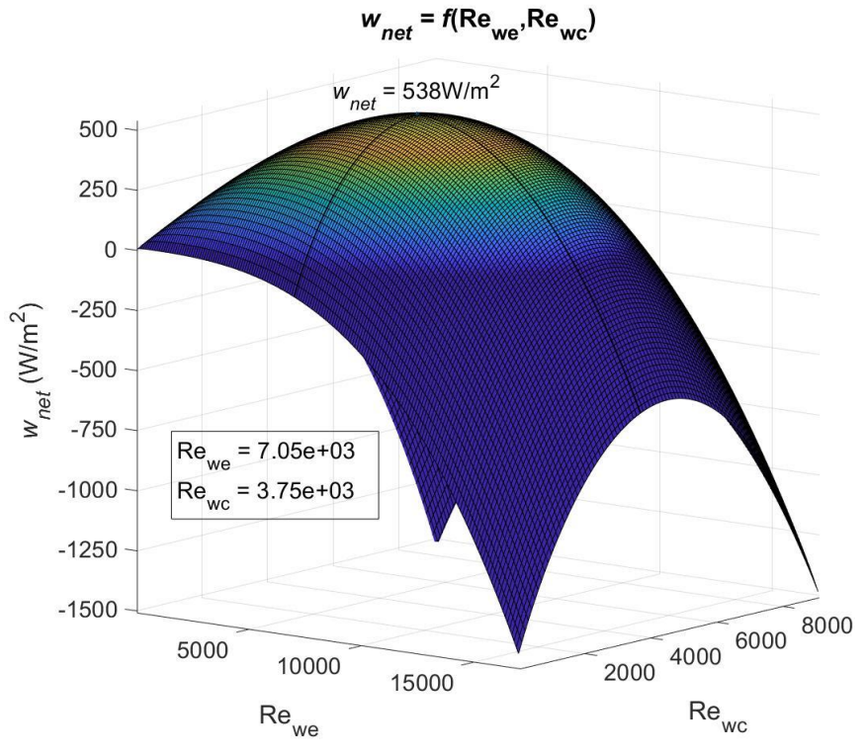

Figure 2-9: Maximum net power output per square meter of heat transfer area for an OTEC power plant as a function of Reynolds numbers using PHE1 as both evaporator and condenser.

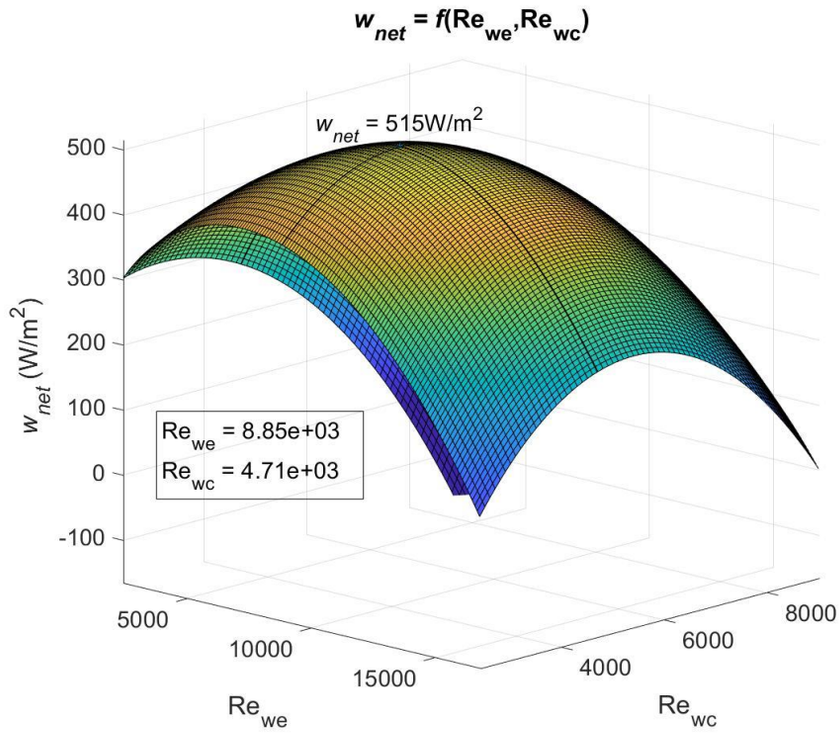

Figure 2-10: Maximum net power output per square meter of heat transfer area for an OTEC power plant as a function of Reynolds numbers using PHE2 as both evaporator and condenser.

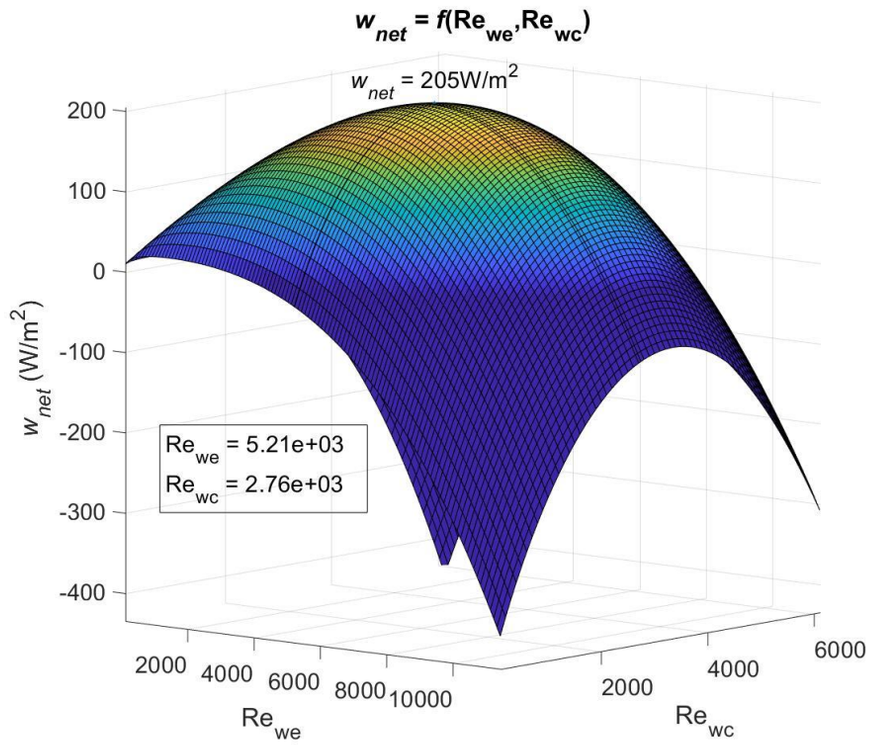

Figure 2-11: Maximum net power output per square meter of heat transfer area for an OTEC power plant as a function of Reynolds numbers using PHE3 as both evaporator and condenser.

Based on the OTEC system maximum net power output per unit of heat exchanger surface area, $w_{net,max}$, it is possible to compare heat exchangers performances. Results in Figure 2-9 to Figure 2-11 show that $w_{net,max}$ varies significantly from one heat exchanger to another. An especially huge difference can be noticed between PHE 3 and the two others; PHE 1 and PHE 2 respectively lead to a $w_{net,max}$ that is 162% and 151% higher than PHE 3. Indeed, although PHE 3 presents the lowest friction factor, it also has the lowest heat transfer coefficient. Besides, PHE 3's plate length is more than twice the length of the other plates, and its equivalent diameter is also smaller. These explain the higher pressure drop in PHE 3 than in PHE 2, as the pressure drop increases with the plate length as well as the squared velocity, which tends to be higher when the equivalent diameter is small.

PHE 2 leads to a $w_{net,max}$ that is only 4.2% lower than PHE 1 despite a heat transfer coefficient 36 to 37% lower, which is explained by a friction factor 53 to 61% lower in case of PHE 2. Regarding the optimum Reynolds numbers, values for PHE 1 are found to be 20% lower than for PHE 2. From this, a heat exchanger that could lead to a higher $w_{net,max}$ than PHE 1, while also having a lower heat transfer coefficient, is easily conceivable given a low enough pressure drop. Such a heat exchanger would have the advantage of being less sensitive to a change in the Reynolds numbers. However, a high pressure drop heat exchanger would require relatively low optimum Reynolds numbers i.e. a lower pumping power to counteract the pressure drop within the pipes and/or lower pipe diameter.

The results of the sensitivity analysis to see the effect of a change in the seawater temperature are shown in Figure 2-12, Figure 2-13, and Figure 2-14.

Results show that a decrease of 2 K induces a 20% decrease in $w_{net,max}$ compared to a decrease of 35% found by Yeh et al. (2005) for the same temperature difference, but a warm seawater temperature 5 K lower. For a temperature drop from 301 K to 298 K, Sinama et al. (2015) found a 40% decrease in the net power output compared to 33% for the same temperatures in the current work. This figure is a little higher and reach 44% in the work from Uehara & Ikegami (1990), still for the same temperature change. Finally, VanZwieten et al., (2017) showed a decrease of 20% and 16% in $w_{net,max}$ when the temperature

changed from 20.12 °C to 21.72 °C and from 20.12 °C to 21.37 °C, respectively, against a 17% drop in this study when a 1.5 °C change occurred in the current work. However, all these authors considered the pressure drop within the water pipes as well as, to some extent. the working fluid circulation pump, which can explain the discrepancy between their work and this chapter's results.

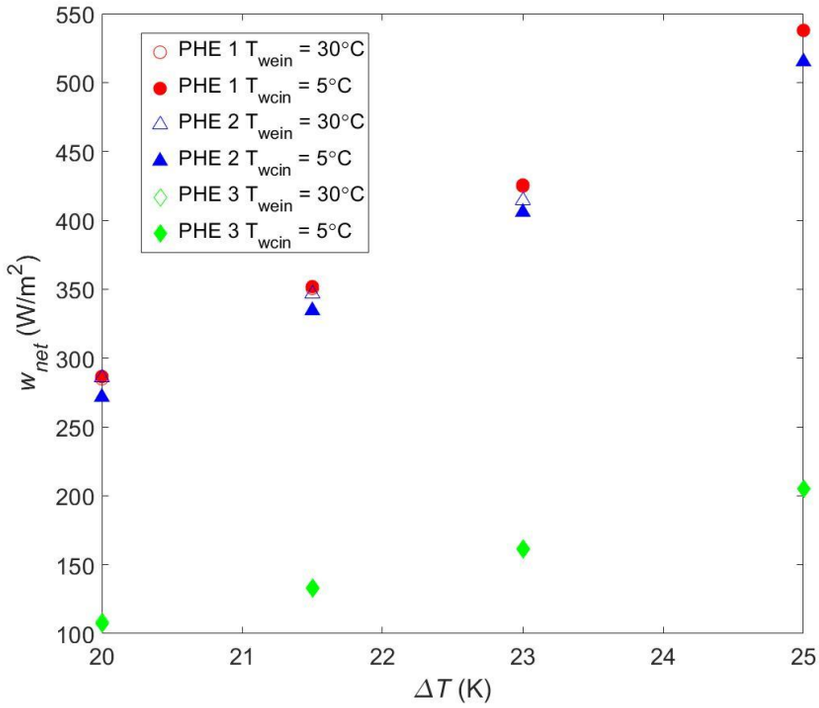

Figure 2-12: Maximum net power output per square meter of heat transfer area as a function of the seawater temperature difference for the Carnot cycle.

A change in the seawater temperature also affects the optimum Reynolds numbers even though the Reynolds numbers difference from one heat exchanger to another remains the same. Indeed, a temperature decrease has limited effect on the pressure drop within the heat exchanger, whereas it significantly decreases the gross power output. As the friction factor hardly changes, the higher the temperature difference, the more an increase of the Reynolds number results in an increase of the heat transfer coefficient.

Finally, the seawater temperature does not affect which heat exchanger lead to the highest $w_{net,max}$. However, the change in the optimum Reynolds numbers as well as the increase of the range for which $w_{net,max}$ is negative, adds to the importance of carefully selecting and controlling the seawater flow rate.

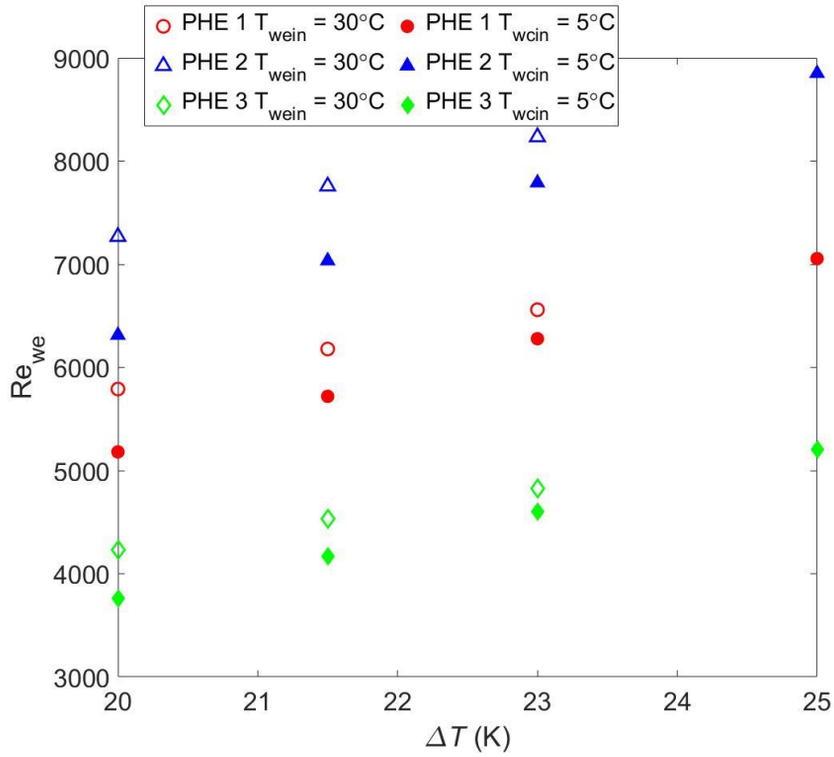

Figure 2-13: Seawater Reynolds number in the evaporator as a function of the seawater temperature difference.

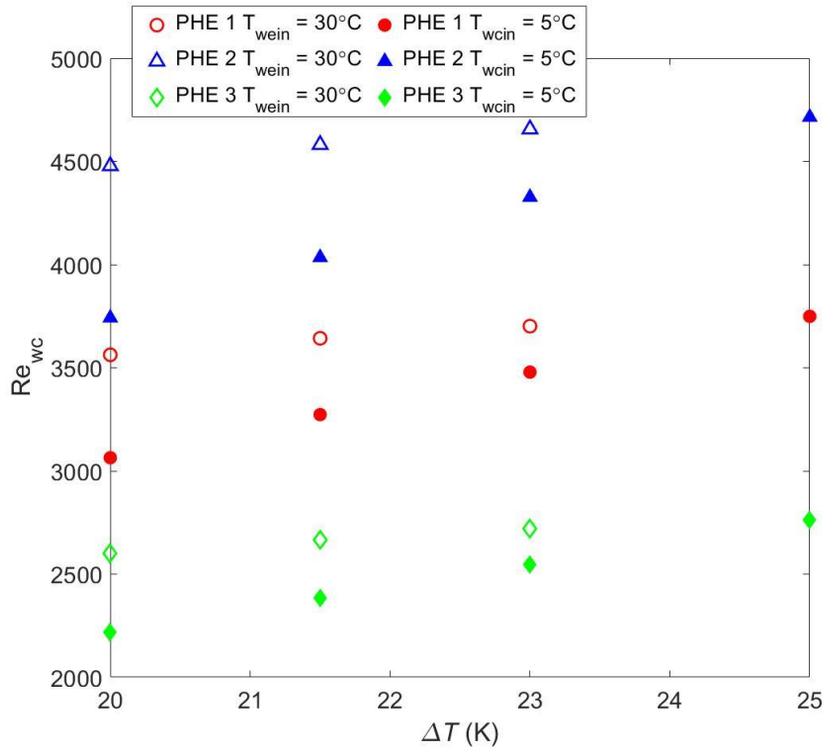

Figure 2-14: Seawater Reynolds number in the condenser as a function of the seawater temperature difference.

2.4.2. Rankine Cycle Results

The optimization was once more performed for the same plate heat exchangers. Constraints violations for optimization results at an inlet warm seawater of 303.15 K and an inlet cold seawater temperature of 278.15, for all heat exchangers are given in Table 2-3. These values are relatively low compared with those of the constraints components, which vary between ten to the power five to ten to the power six, indicating that constraints were successfully met.

Table 2-3: Constraints violation for all three heat exchangers at $T_{we,in}$ = 303.15 K and $T_{wc,in}$ = 278.15 K.

	PHE 1	PHE 2	PHE 3
evaporator heat balance	3×10^{-7}	5×10^{-9}	-1×10^{-9}
condenser heat balance	6×10^{-8}	6×10^{-8}	2×10^{-9}

The values obtained from the Rankine cycle optimization are summarized in Table 2-4 for the three tested heat exchangers (Kushibe & Ikegami, 2006).

Table 2-4: Comparison between the Carnot and Rankine cycles.

	PHE 1		PHE 2		PHE 3	
	Carnot	**Rankine**	**Carnot**	**Rankine**	**Carnot**	**Rankine**
$w_{net,max}$ (W/m^2)	538	408	515	392	205	155
Re_{we}	7054	6453	8850	7998	5207	4731
V_{we} (m/s)	0.743	0.679	0.943	0.852	0.818	0.743
Re_{wc}	3749	3443	4714	4264	2763	2520
V_{wc} (m/s)	0.738	0.678	0.940	0.851	0.812	0.741

As expected for a real cycle, values $w_{net,max}$ found for the Rankine cycle optimization is lower than for the Carnot cycle. Besides, the change in optimum Reynolds numbers suggests that calculation to accurately assess $w_{net,max}$ should be realized after selecting the suitable heat exchangers to find the actual optimum operating conditions.

Heat transfer coefficient, friction factors, pressure drop as well as pumping power are given in Table 2-5. In the Carnot cycle, as no losses occurs, the amount of power generated for a given seawater flow rate is higher than what the Rankine cycle can generate. The friction factor, however, is computed the same way for

both cycles. Therefore, the Carnot cycle allows for higher Reynolds numbers within the plates, leading to a lower heat transfer coefficient and lower power output in case of the Rankine cycle.

Table 2-5: Heat transfer coefficient, friction factors, pressure drop and pumping power for the Carnot and Rankine cycle and for all heat exchangers.

	PHE 1		PHE 2		PHE 3	
	Carnot	**Rankine**	**Carnot**	**Rankine**	**Carnot**	**Rankine**
α_{we} (kW.m^{-2}.K^{-1})	18.01	16.82	11.46	10.57	9.717	9.00
α_{wc} (kW.m^{-2}.K^{-1})	12.75	11.91	8.102	7.477	6.849	6.366
f_{we} (-)	0.833	0.837	0.327	0.338	0.248	0.251
f_{wc} (-)	0.868	0.873	0.402	0.415	0.269	0.272
ΔP_{we} (kPa)	112.6	94.76	53.98	45.58	111.6	93.25
ΔP_{wc} (kPa)	116.7	98.94	66.36	56.12	120.0	100.9
W_{Pwe} (kW)	11.46	11.03	0.613	0.592	3.78	3.582
W_{Pwc} (kW)	11.81	11.50	0.751	0.728	4.030	3.865

Similarly to the Carnot cycle optimization, a sensitivity analysis was conducted and results are presented in Figure 2-15, Figure 2-16 and Figure 2-17.

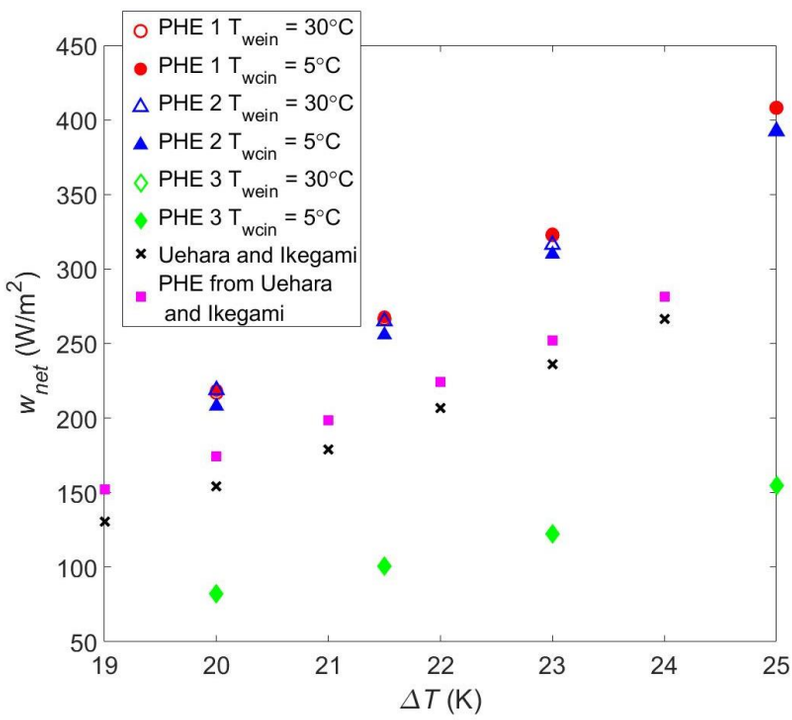

Figure 2-15: Maximum net power output per square meter of heat transfer area as a function of the seawater temperature difference.

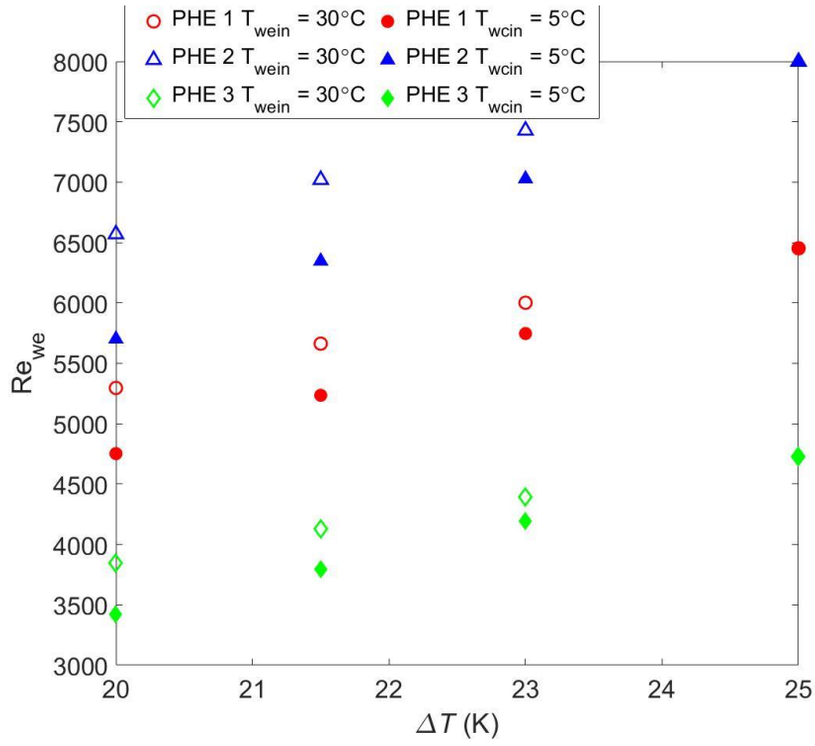

Figure 2-16: Seawater Reynolds number in the evaporator as a function of the seawater temperature difference.

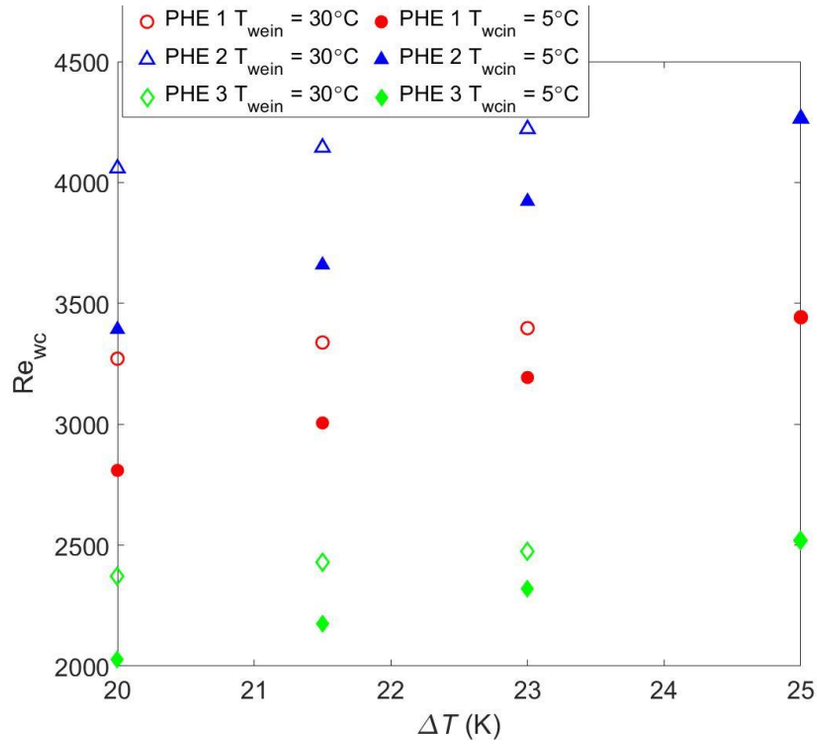

Figure 2-17: Seawater Reynolds number in the condenser as a function of the seawater temperature difference.

Regarding $w_{net,max}$, in addition to this optimization, a comparison with the study realized by Uehara & Ikegami (1990) is made in Figure 2-15. Results found

in the current optimization range from 81 W/m² to 408 W/m² for PHE 3 at the lowest temperature difference and PHE 1 at the highest temperature difference, respectively. Uehara & Ikegami (1990) found a $w_{net,max}$, of 153.9 W/m² and 236 W/m² for a ΔT of 20 °C and 23 °C, respectively. This situates the heat exchanger they considered between PHE 2 and PHE 3, which lead to a $w_{net,max}$, of 81 W/m² and 208 W/m², respectively, at a ΔT of 20 °C, and 121 W/m² and 310 W/m², respectively, at a ΔT of 23°C . These values are in the range of what is found in the current study, and are significantly lower compared to PHE 1. Optimization using the same heat exchangers as those from Uehara & Ikegami (1990) was also realized as seen in Figure 2-15, and it was found that the current method tend to overestimate the net power output to heat transfer area ratio.

Another comparison can be realized with the study of Bernardoni et al., (2019) who showed a net power output of 167W/m² and a gross power output of 278 W/m² for a ΔT of 24°C, which is lower than the 310 W/m² found with PHE 2 at a ΔT of 23°C. Again, their work included working fluid side heat transfer and pressure drop as well as pressure drop within the water pipe, although only the latter contributed to decreasing the gross power output.

Both these studies are more accurate than the presented one; their goal was to precisely assess the net power output of the system, either to calculate a reliable LCOE in the case of Bernardoni et al. (2019), or for a very specific OTEC power plant design in the case of Uehara & Ikegami (1990). The current study, however, focuses on comparing the performance of heat exchangers, therefore, such accurate assessment is not as relevant. In comparison, there is still plenty of room for increasing the OTEC system performance regarding the choice or optimization of the heat exchangers in their methods. Regardless, the trend obtained by Uehara and Ikegami is consistent with what was found in this work as shown in Figure 2-15.

As for the Carnot cycle, a temperature change has a significant effect on the maximum net power output of the OTEC system. A 20% decrease in $w_{net,max}$ occurs with a decrease of two degrees in the temperature difference, and a 46–47% decrease is observed with a decrease of five degrees in the temperature difference, depending on the heat exchanger. These values correspond to what was found for

the Carnot cycle. The heat exchanger leading to the highest value of $w_{net,max}$ do not vary with the temperature although the gap between two different heat exchangers varies along with the temperature. The optimum Reynolds number also tends to increase as the temperature increases, which confirms the need of an accurate assessment of the optimal operating point for each specific power plant. The Reynolds numbers difference between one heat exchanger to another seems to remain the same as with the Carnot cycle, with values 19% to 41% lower than PHE 2 for PHE 1 and PHE 3, respectively.

Although the maximum net power output and optimum Reynolds numbers vary from the Carnot cycle to another, the preferable heat exchanger remains the same. Indeed, the ratio of $w_{net,max}$ achieved using a Rankine cycle over the one achieved using the Carnot cycle is found to be fairly constant, with figures around 0.76 for all heat exchangers and for all the computed ΔT. It is therefore possible, for heat exchanger selection, to base the calculation on the Carnot cycle only.

With the Rankine cycle optimization, it is also possible to check the boiling and condensation temperatures, which are shown in Figure 2-18 and Figure 2-19.

Inside the evaporator, the heat transfer coefficient increases as the warm seawater temperature increases, and more energy can be transferred from the warm seawater to the working fluid, leading to an increase of both the operating pressure and boiling temperature, and, therefore, an increase of the gross power output generated by the turbine. A similar phenomenon is observed in the condenser; as the cold seawater temperature decreases, the amount of energy that can be transferred to the seawater increases, reducing both saturation temperature and pressure, thus, leading to an increase in the turbine gross power output.

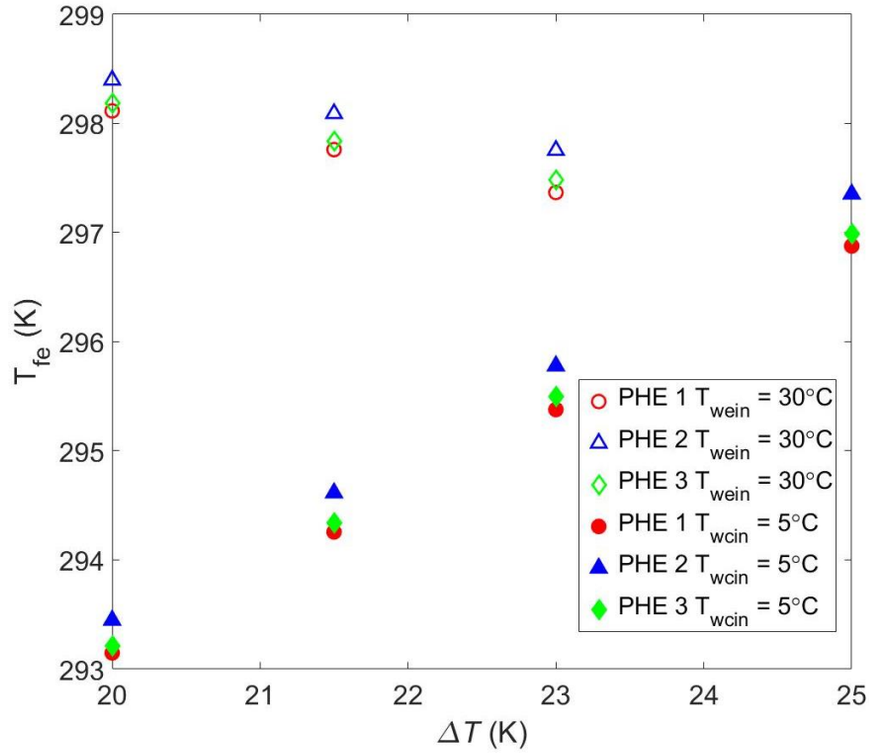

Figure 2-18: Working fluid boiling temperature as a function of the seawater temperature difference.

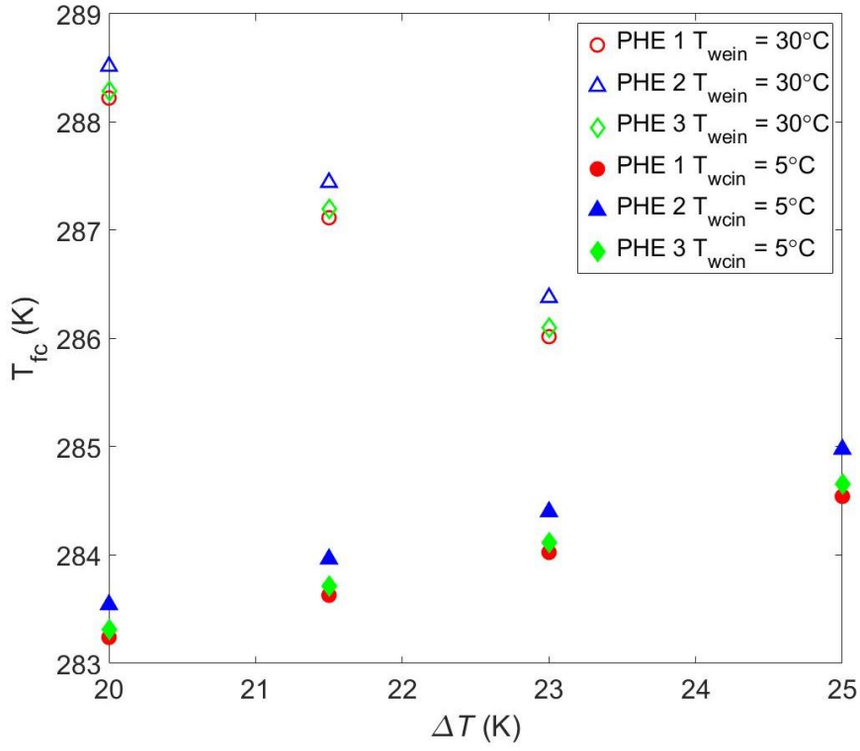

Figure 2-19: Working fluid condensation temperature as a function of the seawater temperature difference.

In OTEC power plants, the pressure drop plays a major role in the choice of a heat exchanger. A study solely focusing on the heat transfer performance might reach to a completely different conclusion regarding which heat exchanger to use as the power output would increase without limit with the Reynolds numbers. The limitation induced by the pressure drop within the heat exchangers can be seen easily in the Carnot cycle results; without pressure drop consideration, the net power output cannot be negative nor decrease as the Reynolds numbers increase. However, Figure 2-9 to Figure 2-11 present parabolic graphs that include areas of negative net power output.

2.5. Conclusion

The goal of this section was to develop a method to compare heat exchanger performance based on the OTEC system's maximum net power output to heat transfer area ratio. An objective function of the net power output per unit of heat exchanger surface area has been derived for both the Carnot and the Rankine cycle. These functions considered both the seawater heat transfer coefficient and pressure drop within the heat exchangers, and were maximized through Matlab(The MathWorks Inc., 1990 -2019). The method was then showcased for three heat exchangers from the literature at four temperature differences. Each value of temperature difference included two points and considered an increase of the cold seawater temperature or a decrease of the warm seawater temperature. The evaluation method that was developed differs from others thanks to its relative ease of use. The following conclusions were made.

- For the sole purpose of a heat exchanger comparison, calculations based on the Carnot cycle for any source temperature were sufficient, as the cycle and temperature difference do not have an impact on the choice of the heat exchanger even though they do change the power output and optimum operating conditions. The Rankine cycle calculations presented a maximum net power output to heat transfer area ratio 24% lower than for the Carnot cycle. For both cycle, a decrease in the net power output of ~10% each time a temperature difference decrease of 1 °C was observed. The evolution of the power

output as a function of the temperature difference was found to follow the same trends as found in other studies.

- The maximum net power output was found to highly depends on the chosen heat exchangers. For the highest temperature difference, the most suitable heat exchanger among the three considered led to a maximum power output 162% and 165% higher than the worst heat exchanger for the Carnot and Rankine cycles, respectively.
- Due to the trade-off that exists between the heat transfer coefficient and the pressure drop, the heat exchanger presenting the highest heat transfer coefficient is not necessarily the one that will lead to the highest maximum net power output. In this study, for the Carnot cycle, PHE 2 competed with PHE 1 as it led to a maximum net power output that was only 4.2% lower than the one of PHE 1, even though its heat transfer coefficient was 36% lower.
- Heat exchangers with a high pressure drop and those with a low pressure drop have been found to have their own advantages and drawbacks. High pressure drop heat exchangers require lower Reynolds numbers, and, therefore, a smaller pumping power and/or a smaller pipe diameter are needed. Low pressure drop heat exchangers are less sensitive to a change in the Reynolds numbers, which can be useful in case a change in the operating conditions is needed. This is even more important as the results showed that negative net power output can be reached for low enough Reynolds numbers.

If the most suitable heat exchanger was found, assessments of the maximum power output and the optimum operating point are not accurate enough to be used for OTEC design. Working fluid heat transfer coefficient as well as fouling thermal resistance were neglected; however, as they can have a significant impact on the OTEC performance, they should be further studied in the future. In addition, the comparison can only be done with existing heat exchangers, as specific correlations for the heat transfer coefficient and the pressure drop are needed; thus, it is difficult to know in advance what the effect of a specific design will be.

Chapter 3.

ACCURACY IMPROVEMENT AND OPTIMIZATION OF HEAT EXCHANGER GEOMETRY.

The method in Chapter 2 allows the comparison of different heat exchangers once the heat transfer and pressure drop correlations are known. However, it does not take into account the heat transfer coefficient and pressure drop of the working fluid. Neither does it allow an optimization of the plate heat exchangers' geometry design parameters. The goal of this chapter is to tackle these two issues by introducing the working fluid heat transfer coefficient and pressure drop

correlations, and changing waterside correlations from heat exchanger specific ones to global ones. These correlations use the plate heat exchanger chevron angle β as well as the enlargement factor ϕ which is defined as:

$$\phi = \frac{A_{eff}}{A_{proj}} \tag{3-1}$$

With A_{eff}, the effective heat transfer area and A_{proj}, the projected heat transfer area.

This enlargement factor can be approximated using the following equation from Amalfi et al. (2016a):

$$\phi \approx \frac{1}{6}\left(1 + \sqrt{1 + Z^2} + 4\sqrt{1 + \frac{Z^2}{2}}\right) \tag{3-2}$$

Where the parameter Z is defined as a function of the mean channel spacing δ and the corrugation pitch Λ:

$$Z = \frac{\pi\delta}{\Lambda} \tag{3-3}$$

Furthermore, some correlations are based on the hydraulic diameter rather than the equivalent diameter. This hydraulic diameter, D_h, is defined as the equivalent diameter D_{eq} divided by the enlargement factor ϕ. The chevron angle β, corrugation pitch Λ, and mean channel spacing δ are defined in Figure 1-10 and Figure 1-11 along with the length, L, and width, Wi.

3.1. Objective function and Optimization parameters

The objective function is based on the Rankine cycle and is similar to Equation (2-22). However, the effect of the working fluid pressure drop within the heat exchangers on the net power output must be included. To get a better comparison of the plate geometry, the net power output is computed using a single active plate of heat exchanger.

$$w_{net} = \frac{1}{A_e + A_c}\left(\underbrace{m_f(h_2 - h_3)}_{\dot{W}_G} - \underbrace{m_f(h_1 - h_4)}_{\dot{W}_{P,f}} - W_{P_{f\Delta Pe}} - W_{P_{we}} - W_{P_{wc}}\right) \tag{3-4}$$

Where $W_{P,f}$ is the pumping power due to the pressure difference between the evaporator and condenser, and $W_{P_{f\Delta Pe}}$ is the pumping power required to

counteract the working fluid pressure drop within the evaporator. The effect of the working fluid pressure drop in the condenser is discussed in the next section.

In the Rankine cycle optimization of Chapter 2, the seawater outlet temperatures at both heat exchangers are guessed and the saturation temperature of the condenser and evaporator, which are required to compute the gross power output, are derived from the heat exchangers NTU as well as those two guessed temperatures. The NTU is based on water properties which are assumed to be the same as the water inlet properties. In this chapter, the NTU is computed from both the water and working fluid heat transfer coefficients, thus, working fluid properties are required. These properties can be computed through REFPROP. However, to do so, the saturation temperatures in the heat exchangers are required. Therefore, instead of guessing the seawater outlet temperature like in Chapter 2, the optimization process is slightly changed and the working fluid saturation temperatures are guessed. From these temperatures, it is possible to compute heat exchangers' NTUs, which are then used to compute the seawater temperature at the heat exchangers outlet using the relation from Equation (2-24). Introducing the working fluid heat transfer coefficient and pressure drop also require two more variables, the mean vapor quality in both heat exchangers, which are also guessed in the optimization process. A comprehensive flow chart is given in Figure 3-1 at the end of section 3.3

3.1.1. Gross power output

All the 7 parameters are firstly guessed within the following range:

Table 3-1: Boundaries of optimization parameters.

Parameter	Min	Max
Working fluid mass flow rate, m_f (kg/s)	0.0001	5
Warm seawater mass flow rate, m_{we} (kg/s)	v = 0.1m/s	v = 1.8m/s
Cold seawater mass flow rate, m_{wc} (kg/s)	v = 0.1m/s	v = 1.8m/s
Saturation temperature at the evaporator outlet, T_2 (K)	$T_{wc,in}$	$T_{we,in}$
Saturation temperature at the condenser outlet, T_4 (K)	$T_{wc,in}$	$T_{we,in}$
Mean vapor quality in the evaporator x_e (-)	0	1
Mean vapor quality in the condenser x_c (-)	0	1

$T_{we,in}$ and $T_{wc,in}$ are the warm seawater and cold seawater inlet temperature, respectively.

For the evaporator, it is possible to assume equal pressure between the inlet and outlet, and subtract a term corresponding to the required pumping power to the net power output equation as shown in Equation (3-4). However, as the condenser outlet temperature is assumed, and looking at the cycle in Figure 2-4, the working fluid pressure drop in the condenser does not affect the pumping power, but rather induce a decrease in the available pressure difference at the turbine, i.e., the pressure at point 3 is higher than the one for an isobaric heat transfer. Therefore, the specific enthalpy at point 3' – hypothetical point assuming isentropic process – is computed as the enthalpy at pressure $P_3 = P_4 + \Delta P_{cond}$, and at entropy at point 2. Other points on the cycle are computed the same way as in Chapter 2, using the saturation temperatures as well as pump and turbine efficiencies.

3.1.2. Pressure drop

3.1.2.1. Seawater pressure drop

The seawater pressure drop in both heat exchangers is computed with a correlation given in Equation (3-5), which can be used for a wide range of heat

exchangers (Muley & Manglik, 1999). Although the authors stipulated that the correlation is only correct in the 30° - 60° range, Kushibe & Ikegami (2006) found a good agreement between this correlation and their data for PHE1, which presents a chevron angle of 72°.

$$\mathrm{f_w} = (2.917 - 0.1277\beta + 2.016e^{-3}\beta^2)(5.474 - 19.02\phi + 18.93\phi^2 - 5.341\phi^3)\mathrm{Re}^{-\left(0.2+0.0577\sin\left(\frac{\pi\beta}{45}+2.1\right)\right)} \quad (3\text{-}5)$$

The pumping power required to counteract the pressure drop is computed as:

$$W_{Pw} = \underbrace{\frac{2\mathrm{f_w}L\mathrm{Re_w}^2\mu_w^2}{D_{eq}^3\rho_w}}_{\Delta P_w}\frac{\mathrm{Re_w}\mu_w}{\rho_w D_{eq}\eta_{\mathrm{P.w}}} \quad (3\text{-}6)$$

3.1.2.2. Working fluid pressure drop in the evaporator

For the working fluid in the evaporator, the correlation from Amalfi et al. (2016b) given in Equation (3-7) is used. It was derived from a significant amount of experimental points (1698 data points) with different working fluids – including ammonia – chevron angle from 27° to 70°, and mass fluxes from 5.5 to 610 kg.m^{-2}.s^{-1}

$$\mathrm{f_{f,e}} = 15.698(2.125\beta^{*9.993} + 0.955)\mathrm{We_e}^{-0.475}\mathrm{Bd}^{0.255}\rho^{*-0.571} \quad (3\text{-}7)$$

ρ^* is the ratio between the liquid and vapor density. We and Bd are the Weber and Bond numbers, they are non-dimensional numbers often used in multiphase flow and describe the ratio between the fluid inertia and its surface tension, and the ratio between the gravitational forces (buoyancy) and the surface tension forces, respectively. They are given in Equations (3-8) and (3-9).

$$\mathrm{We} = \frac{G^2 D_h}{\rho_m \sigma} \quad (3\text{-}8)$$

$$\mathrm{Bd} = \frac{(\rho_l - \rho_v) g D_h^2}{\sigma} \quad (3\text{-}9)$$

G is the working fluid mass flux and ρ_m is the homogeneous density for which the two-phase flow is treated as a single fluid at the average vapor quality:

$$\frac{1}{\rho_m} = \frac{x}{\rho_v} + \frac{1-x}{\rho_l} \tag{3-10}$$

The pressure drop is computed from the friction factor using Equation (3-11):

$$\Delta P_{fe} = \frac{2\mathrm{f_{fe}} G_e^2 L_e}{\rho_{m_e} D_{h_e}} \tag{3-11}$$

Then, the pumping power required is derived using Equation (3-12):

$$W_{P_{f\Delta Pe}} = \frac{m_f}{\rho_{fe,l}\eta_{\mathrm{P,f}}} \Delta P_{fe} \tag{3-12}$$

3.1.2.3. Working fluid pressure drop in the condenser

For the condenser, the pressure drop is directly computed from the single phase pressure drop of both the vapor and liquid phases, as recommended by Tao & Ferreira (2020) when it comes to ammonia. Same authors also published general heat transfer and pressure drop correlations for condensation in plate heat exchangers, however, the experimental database from which it was derived did not include ammonia as the working fluid (Tao & Ferreira, 2019). Therefore, the frictional pressure drop model they developed was not based on a wide range of experimental data. More exactly, their data points are limited to their own experiment using a plate heat exchanger with a chevron angle of 62° (Tao et al., 2020). Nevertheless, they attempted to give an accurate correlation for ammonia in plate heat exchangers which depends on the chevron angle and Reynolds numbers of both phases. The equations they used to compute the single phase pressure drop are different form the one from Muley & Manglik (1999) and are given in Equations (3-13) to (3-15):

$$\mathrm{f} = \left(\frac{\cos\beta}{\sqrt{0.18\tan\beta + 0.36\sin\beta + \frac{\mathrm{f_{LT1}}}{\cos\beta}}} + \frac{1-\cos\beta}{\sqrt{\mathrm{f_{LT2}}}} \right)^{-1} \tag{3-13}$$

With

$$\mathrm{f_{LT1}} = \begin{cases} 64\mathrm{Re}^{-1} & \text{if } \mathrm{Re} < 2000 \\ (1.8\ln(\mathrm{Re}) - 1.5)^{-2} & \text{if } \mathrm{Re} \geq 2000 \end{cases} \tag{3-14}$$

$$\mathrm{f_{LT2}} = \begin{cases} 3.8(597\mathrm{Re}^{-1} + 3.85) & \text{if } \mathrm{Re} < 2000 \\ 3.8\mathrm{Re}^{-0.289} & \text{if } \mathrm{Re} \geq 2000 \end{cases} \quad \textit{(3-15)}$$

The Reynolds numbers used to calculate the single phase friction factor are defined in Equations (3-16) and (3-17) for the vapor and the liquid phases, respectively:

$$\mathrm{Re_{v,c}} = \frac{G_c x_c D_h}{\mu_v} \quad \textit{(3-16)}$$

$$\mathrm{Re_{l,c}} = \frac{G_c (1 - x_c) D_h}{\mu_l} \quad \textit{(3-17)}$$

The pressure drop of the two-phase flow is then computed as (Tao & Ferreira, 2020):

$$\Delta P_{fc} = \underbrace{\frac{\mathrm{f_l} G_c^2 (1 - x_c)^2 L_c}{2\rho_l D_h}}_{\Delta P_l} + x_c \underbrace{\frac{\mathrm{f_v} G_c^2 x_c^2 L_c}{2\rho_v D_h}}_{\Delta P_v} + 2\sqrt{\Delta P_v \Delta P_l} \quad \textit{(3-18)}$$

3.2. Constraints functions

At this point, the value of the objective function is known for the guessed parameters. However, to obtain a solution that is physically accurate, as in Chapter 2, some constraints on the parameters are added. The constraints are the heat balance in both heat exchangers, which are the same as in Chapter 2, and two more constraints forcing the average quality to be equal to half the absolute value of the difference between the inlet and outlet quality of the heat exchangers, which should be 0.5 in this optimization. All the constraints are given in Equations (3-19) to (3-22).

$$C_{we}\left(T_{we,in} - T_{we,out}\right) = m_f (h_2 - h_1) \quad \textit{(3-19)}$$

$$C_{wc}\left(T_{wc,out} - T_{wc,in}\right) = m_f (h_3 - h_4) \quad \textit{(3-20)}$$

$$\mathrm{x_e} = \frac{1}{2}\left(\frac{C_{we}\left(T_{we,in} - T_{we,out}\right)}{m_f L_{heat,e}}\right) \quad \textit{(3-21)}$$

$$x_c = \frac{1}{2}\left(\frac{C_{wc}\left(T_{wc,out} - T_{wc,in}\right)}{m_f L_{heat,c}}\right) \quad (3\text{-}22)$$

The seawater temperature at the outlet of the heat exchangers are derived in a similar way as Chapter 2, (See Equation (2-24)) and are given in Equations (3-23) and (3-24). One difference is that the working fluid saturation temperature at the condenser inlet is not equal to working fluid saturation temperature at the outlet due to pressure drop, and the assumption that $T_3 - T_4 << T_{wc,out} - T_{wc,in}$ must be taken. This effect is neglected in the evaporator.

$$T_{wc,out} = T_3 - \left(T_4 - T_{wc,in}\right)e^{-NTU_c} \quad (3\text{-}23)$$

$$T_{we,out} = T_2 + \left(T_{we,in} - T_2\right)e^{-NTU_e} \quad (3\text{-}24)$$

NTUs are computed using the Equation (3-25):

$$NTU = \frac{A}{C_w}\left(\frac{1}{\alpha_w} + \frac{t}{\lambda_p} + \frac{1}{\alpha_f}\right)^{-1} \quad (3\text{-}25)$$

3.2.1. Seawater heat transfer coefficient

As for the seawater pressure drop, a global correlation that depends on the chevron angle as well as the enlargement factor is used (Muley & Manglik, 1999):

$$Nu_w = (0.2668 - 0.006967\beta + 7.244 \cdot 10^{-5}\beta^2)(20.78 - 50.94\phi + 41.16\phi^2 - 10.51\phi^3)\mathrm{Re}^{\left(0.728+0.0543\sin\left(\frac{\pi\beta}{45}+3.7\right)\right)}Pr^{\frac{1}{3}}\left(\frac{\mu}{\mu_{wall}}\right)^{0.14} \quad (3\text{-}26)$$

This Nusselt correlation uses the ratio between the mean viscosity, taken as the inlet viscosity, and the viscosity at the wall condition. However, as the temperature difference between the seawater and the ammonia within the same heat exchanger is rather low, so is the difference between seawater inlet and wall temperatures, thus, the viscosity ratio is considered equal to one within the optimization. Seawater heat transfer coefficients are then deduced from the Nusselt number using Equation (2-17).

3.2.2. Working fluid heat transfer coefficient

3.2.2.1. Boiling heat transfer coefficient

As for the working fluid pressure drop within the evaporator, a correlation from Amalfi et al. (2016b) is used. The equation differs according to the Bond number as the boiling flow transitions from micro-scale to macro-scale at a Bond number of 4:

$$\begin{cases} \mathrm{Nu_{fe}} = 982\beta^{*1.101}\mathrm{We}^{0.315}\mathrm{Bo}^{0.320}\rho^{*-0.224} & \mathrm{Bd} < 4 \\ \mathrm{Nu_{fe}} = 18.495\beta^{*0.248}\,\mathrm{Re_v}^{0.135}\mathrm{Re_{lo}}^{0.351}\mathrm{Bd}^{0.235}\mathrm{Bo}^{0.198}\rho^{*-0.223} & \mathrm{Bd} > 4 \end{cases} \quad (3\text{-}27)$$

With $\mathrm{Re_v}$ and $\mathrm{Re_{lo}}$ the vapor Reynolds number and liquid only Reynolds number, respectively. They are defined in Equation (3-28):

$$\mathrm{Re_v} = \frac{GxD_h}{\mu_v} \quad \text{and} \quad \mathrm{Re_{lo}} = \frac{GD_h}{\mu_l} \quad (3\text{-}28)$$

Bo in Equation (3-27) is the boiling number and is defined as:

$$\mathrm{Bo} = \frac{q}{GL_{heat}} \quad (3\text{-}29)$$

The heat transfer coefficient is computed from the Nusselt number by taking the liquid thermal conductivity as reference.

3.2.2.2. Condensation heat transfer coefficient

The condensation heat transfer coefficient has two different components; one governed by convective forces and the other by gravitational forces. When the liquid Weber number defined in Equation (3-30) is higher than a critical value of 0.12, the condensation is taken as fully convective. Otherwise, for a liquid Weber number smaller than 0.12, both mechanisms are involved and the heat transfer coefficient is taken as in Equation (3-31)(Tao & Ferreira, 2020).

$$\mathrm{We_l} = \frac{G^2(1-x)^2D_h}{\rho_l\sigma_c} \quad (3\text{-}30)$$

$$\alpha_{f,c} = \Theta\alpha_{conv} + (1-\Theta)\alpha_{grav} \quad (3\text{-}31)$$

α_{conv} is the convective condensation heat transfer coefficient and α_{grav}, the gravitational condensation heat transfer coefficient. Θ is a value between 0 and 1

and is equal to the maximum between 1 and the ratio between the liquid Weber number and the critical Weber number (0.12).

The gravitational condensation heat transfer coefficient is given in Equation (3-32):

$$\alpha_{grav} = 0.36\mathrm{Co}^{-0.28}\left(\frac{g\rho_l \Delta\rho L_{heat}\lambda_l^3}{\mu_l \Delta T_{wall} D_h}\right)^{0.25} Pr_l^{\frac{1}{3}} \tag{3-32}$$

In this equation, $\Delta\rho$ is the difference between the liquid and vapor densities, Co, is the convection number defined in Equation (3-33) and ΔT_{wall} is the difference between the saturation temperature and wall temperature on the working fluid side, which is computed from the heat flux conservation throughout the plate as shown in Equation (3-34).

$$\mathrm{Co} = \sqrt{\frac{\rho_v}{\rho_l}}\left(\frac{1-x}{x}\right)^{0.8} \tag{3-33}$$

$$q = m_f(h_3 - h_4) = \alpha_{wc}A_c\left(T_{w,c,wall} - T_{w,c,in}\right) = \frac{\lambda_p}{t_p}A_c(T_{f,c,wall} - T_{w,c,wall}) \tag{3-34}$$

From this, it comes:

$$T_{f,c,wall} = T_{w,c,in} + \frac{m_f}{A_c}(h_3 - h_4)\left(\frac{1}{\alpha_{wc}} + \frac{t_p}{\lambda_p}\right) \tag{3-35}$$

The convective condensation heat transfer coefficient α_{conv} in Equation (3-31) is given by the following expression:

$$\alpha_{conv} = \alpha_{lo}(0.17\mathrm{Co}^{-1.12}\mathrm{Fr_l}^{-0.2} + (1-x_c)^{0.748}) \tag{3-36}$$

With α_{lo}, the single phase heat transfer coefficient assuming a fully liquid phase and $\mathrm{Fr_l}$, the liquid Froude number defined as:

$$\mathrm{Fr_l} = \frac{G^2}{\rho_l^2 g D_h} \tag{3-37}$$

The single phase heat transfer coefficient is expressed as:

$$\alpha_{lo} = 0.122(\mathrm{f_{lo}} sin\ 2\beta\ )^{0.374}\mathrm{Re_{lo}}^{0.748}\mathrm{Pr}^{\frac{1}{3}}\left(\frac{\mu}{\mu_{wall}}\right)^{0.167}\frac{\lambda_l}{D_h} \tag{3-38}$$

f_{lo} is the single phase friction factor assuming a fully liquid working fluid and is computed from Equations (3-13) to (3-15) based on Re_{lo} defined in Equation (3-28). Once again, the ratio of viscosity which appears in the heat transfer coefficient equation is assumed to be equal to one due to the small temperature difference on both sides of the plate.

3.3. Optimization Process

Using Equation (3-6) to compute the seawater pumping power, Equation (3-12) to compute the working fluid pumping power due to the pressure drop within the evaporator, and including, as discussed in Section 3.1.1, the working fluid pressure drop within the condenser (Equation (***3-18***) in the determination of specific enthalpies with respect to Section2.1.2, the value of the objective function defined in Equation (3-4) can be evaluated. Then, using the seawater heat transfer coefficient in both heat exchangers as well as working fluid heat transfer coefficient in the evaporator and condenser defined in Equations (3-26), (3-27), and (3-31), respectively, the NTU for both heat exchangers defined in Equation (3-25) can be calculated. This leads to the computation of outlet seawater temperatures in both heat exchangers, as shown in Equations (3-23) and (3-24). These temperatures are used in constraint equations – (3-19) and (3-20) – to ensure physically viable results while performing the optimization.

Input data for this optimization method are the inlet temperatures of the warm and cold seawater, $T_{we,in}$ and $T_{wc,in}$, respectively as well as the heat exchangers design parameters defined in Figure 1-10 and Figure 1-11, namely the heat transfer length L, the width, Wi, the chevron angle β, the mean channel spacing δ, and the corrugation pitch Λ. The effect of these input parameters on the objective function is also investigated throughout Section 3.5. As shown in Table 3-1 there are 7 optimization variables which are the working fluid mass flow rate m_f, the warm and cold seawater mass flow rates, m_{we} and m_{wc}, respectively, the saturation temperature in the evaporator and condenser T_2, and T_4, respectively, and the mean vapor quality in the evaporator and condenser, x_e and x_c, respectively. The comprehensive flow chart of this optimization process is given in Figure 3-1.

As for Chapter 2, seawater properties are computed at a salinity of 35 ppt, inlet seawater temperatures, and atmospheric pressures using the seawater proprieties software developed by the Massachusetts Institute of Technology (2016). The maximum value of the objective function as well as the computation of a new set of optimization parameters at each iteration is realized with Matlab R2019b (The MathWorks, Inc., 1990 -2019), and the function "fmincon", based on a sequential quadratic programing algorithm (MathWorks®, n.d.).

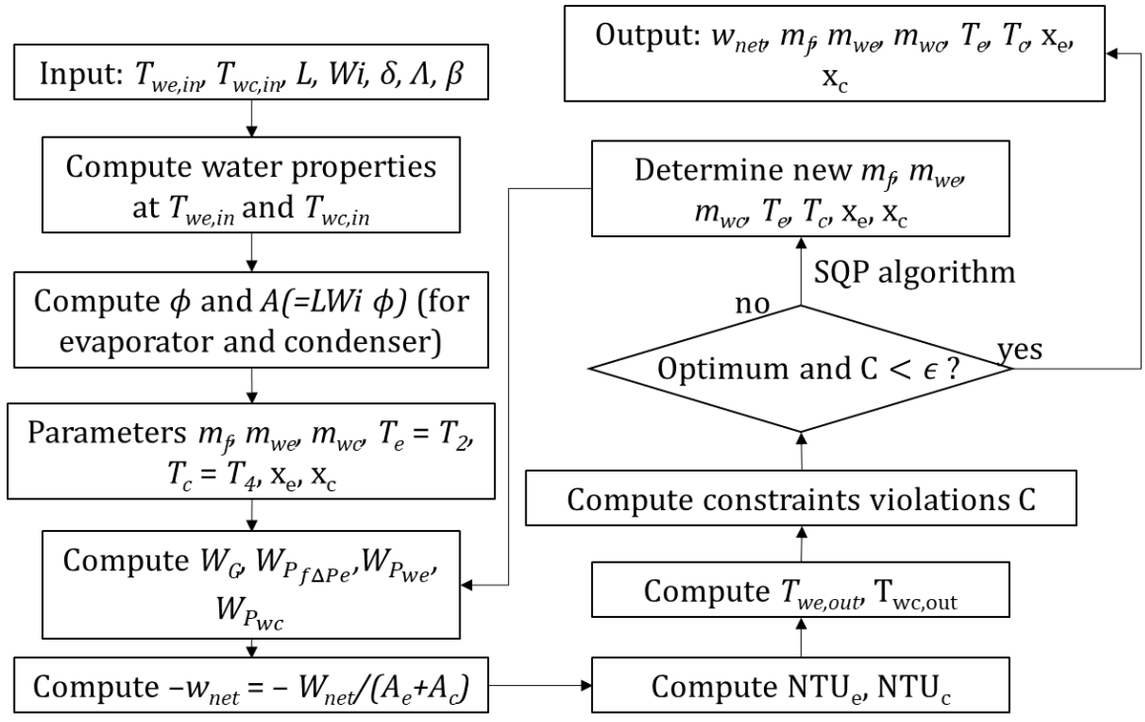

Figure 3-1: Flow chart of the optimization process with global correlations, and including the working fluid heat transfer coefficient and pressure drop.

3.4. Comparison with standard method

Compared with the method from Chapter 2, two more variables and two more constraints are added. Although this accuracy improvement implies to compute more data, namely the working fluid heat transfer coefficient and pressure drop, the optimization process itself is identical, and, therefore, remains simpler, in terms of computation time, than a standard method such as the one developed by Uehara & Ikegami (1990).

3.5. Results and discussion

3.5.1. Comparison between the seawater correlations

Before reviewing the optimization results, a comparison between the correlations from Muley & Manglik (1999) and those used in Chapter 2 was carried out.

Figure 3-2 shows the result of the comparison between the Nusselt correlations used in Chapter 2 and the correlation from Muley & Manglik (1999) for a seawater temperature of 303.15 K at atmospheric pressure. The global correlation from Muley & Manglik (1999) tends to underestimate the Nusselt number for both heat exchangers. Even on a restricted range from 1 000 to 11 000, the maximum percentage error compared with the correlations used in Chapter 2 are of 40% and 43% for PHE 1 and PHE 2, respectively.

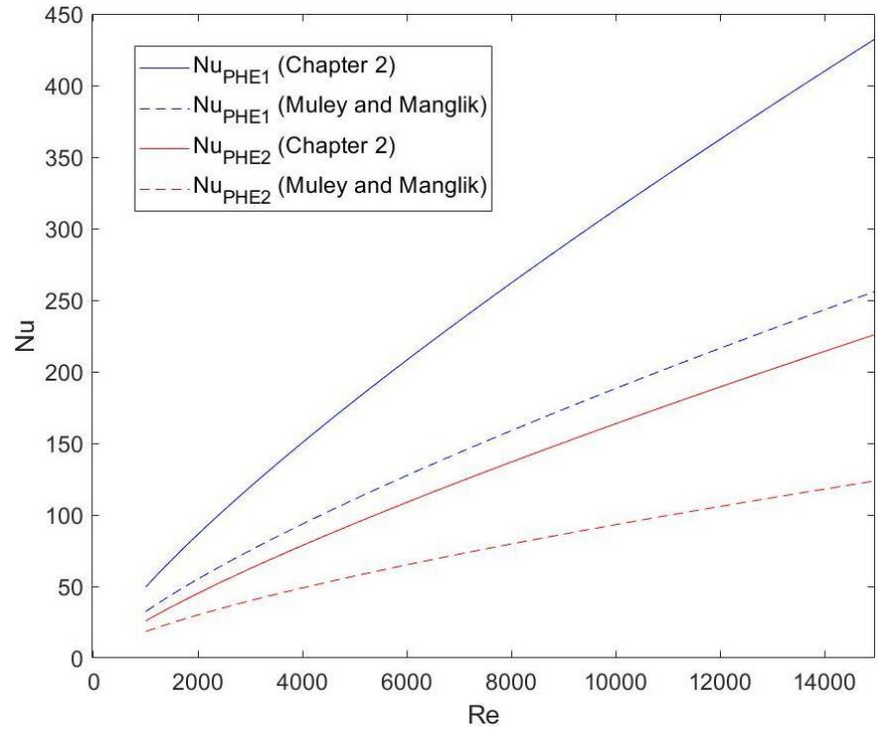

Figure 3-2: Comparison between the Nusselt correlations from Chapter 2 and the one from Muley and Manglik.

Regarding the pressure drop correlations, results are presented in Figure 3-3. The correlation from Muley & Manglik (1999) highly underestimates the friction factor for both heat exchangers with a maximum percentage error on the 1 000 – 10 000 Reynolds number range of 70% and 74% for PHE 1 and PHE 2, respectively.

From Figure 3-2 and Figure 3-3, it clearly appears that using the correlations from Muley & Manglik (1999) will lead to a less accurate prediction of the maximum net power output of an OTEC power plant than specific correlations. However, they present the advantage of including the chevron angle and enlargement factor of the heat exchangers allowing for a comparison based on plate heat exchanger geometry.

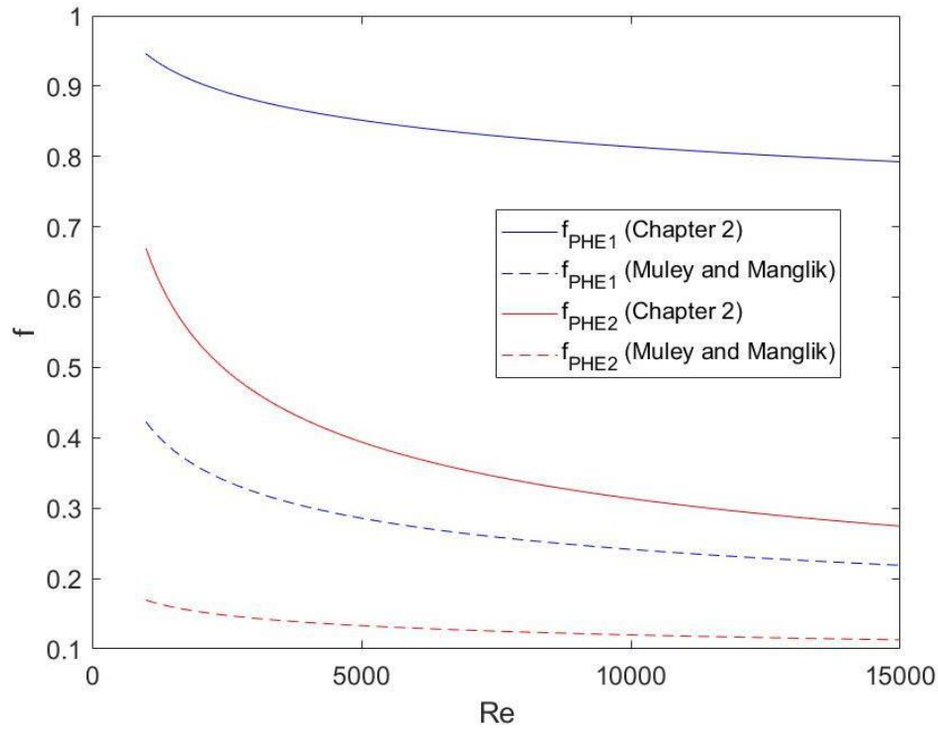

Figure 3-3: Comparison between the friction factor correlations from Chapter 2 and the one from Muley and Manglik.

3.5.2. Optimization of PHE 1 and PHE 2

3.5.2.1. Comparison with previous optimization

Optimization results are compared with those obtained in Chapter 2 as shown in Table 3-2. $Rankine_f$ refers to the Rankine cycle considering the working fluid heat transfer coefficients and pressure drop, whereas $Rankine_w$ refers to the Rankine cycle for which only seawater heat transfer coefficients and pressure drop are considered.

Although $w_{net,max}$ is the maximum net power output per unit of heat transfer area, it will be referred to as the maximum net power output throughout this chapter.

Because the optimization uses correlations based on chevron angles, it is not possible to get results from PHE 3, which does not have a herringbone geometry. Also, for a more accurate comparison, Reynolds numbers given in Table 3-2 and Table 3-3 are based on the equivalent diameter and not the hydraulic diameter, which is used by some of the new correlations. Hydraulic diameter based Reynolds number can be found by dividing the equivalent diameter based Reynolds number by the enlargement factor ϕ of the heat exchangers, which are 1.159 and 1.155 for PHE 1 and PHE 2, respectively.

Table 3-2: Comparison between the result of the Rankine cycle considering the working fluid heat transfer coefficient and pressure drop with results considering only seawater ones.

	PHE 1			**PHE 2**		
	$Carnot_w$	**$Rankine_w$**	**$Rankine_f$**	**$Carnot_w$**	**$Rankine_w$**	**$Rankine_f$**
$w_{net,max}$(W/m²)	538	408	251	515	392	210
Re_{we}	7 054	6 453	5 014	8 850	7 998	5 865
v_{we} (m/s)	0.743	0.679	0.528	0.943	0.852	0.625
Re_{wc}	3 749	3 443	2 724	4 714	4 264	3 240
v_{wc} (m/s)	0.738	678	0.537	0.940	0.851	0.642

Results show a maximum net power output, that is slightly higher than half of what was found for the Rankine cycle when only the seawater side was considered. This shows that, contrary to what was assumed in Chapter 2, the working fluid heat transfer coefficient and pressure drop need to be accounted for when trying to give an accurate prediction of the net power output and optimum operating point of an OTEC power plant. This being said, it should be noted that the plate heat exchanger which lead to the highest net power output remains the same.

The decrease in the seawater Reynolds number can be explained by the fact that the working fluid heat transfer coefficient is no longer assumed to be much greater than the seawater heat transfer coefficient, meaning that there is a limit to the amount of heat that can be given or taken from the working fluid. To be sure that the decrease in the seawater Reynolds number is not due to the different seawater correlations, the optimization was also carried out using the correlations from Chapter 2 for which the results can be seen in Table 3-3.

The results from Table 3-3 confirm that the decrease in the seawater Reynolds number is not caused by the difference between the correlations. Moreover, despite the poor results obtained when comparing the correlations in section 3.5.1, global correlations from Muley & Manglik (1999) only lead to a 5.4% overestimation of the maximum net power output for PHE 1 and a slightly underestimated one of 1.4% for PHE 2.

Table 3-3: Optimization results considering the working fluid side heat exchanger performances using the seawater correlations from Chapter 2.

	PHE 1	**PHE 2**
$w_{net,max}$(W/m²)	238	213
Re_{we}	3 465	4 238
v_{we} (m/s)	0.365	0.451
Re_{wc}	1 924	2 296
v_{wc} (m/s)	0.379	0.458

To further explain the decrease in the maximum net power output as well as in the seawater Reynolds numbers, the heat transfer coefficient of both fluids for both the evaporator and condenser are given in Table 3-4:

Table 3-4: Comparison between seawater and working fluid heat transfer coefficient for both heat exchangers.

	PHE 1		**PHE 2**	
	Seawater	**Working fluid**	**Seawater**	**Working fluid**
α_e (kW.m^{-2}.K^{-1})	9.82	5.26	5.72	3.56
α_c (kW.m^{-2}.K^{-1})	7.22	17.27	4.41	19.67

According to these results, the computed boiling heat transfer coefficient using the correlation from Amalfi et al. (2016b) are found to be smaller than the seawater heat transfer coefficient in the evaporator. This is believed to be the main cause of the decrease of the maximum net power output as well as seawater Reynolds numbers and is in contradiction with the assumption of a working fluid heat transfer coefficient much greater than the seawater heat transfer coefficient made in Chapter 2. Even in the case of the condenser, the working fluid heat transfer coefficient is only 2.4 and 4.5 times higher than the seawater heat transfer

coefficient for PHE1 and PHE 2, respectively, which is not sufficient to validate the assumption.

Regarding the pressure drop values summarized in Table 3-5, the assumption of a negligible working fluid pressure drop is validated in the condenser which presents extremely low values of 217 Pa and 7.6 Pa, which correspond to a working fluid temperature difference within the condenser of 0.01 and 3×10^{-4} K for PHE 1 and PHE 2, respectively. When PHE 1 is used, however, the seawater side pressure drop is 4.6 times higher than the working fluid one, which does not seem to be enough to validate the assumption. However, this pressure drop corresponds to a pumping power of 0.1 W, against 34.4 W for the seawater.

Table 3-5: Comparison of the seawater and working fluid pressure drop for both heat exchangers.

	PHE 1		**PHE 2**	
	Seawater	**Working fluid**	**Seawater**	**Working fluid**
ΔP_e (kPa)	22.61	5.01	10.92	0.590
ΔP_c (kPa)	27.25	0.217	12.82	7.6×10^{-3}

3.5.2.2. Governing heat transfer coefficient equations

As specified in section 3.2.2, the boiling heat transfer coefficient equation changes whether the flow boiling is micro or macro-scale with a transition value when the Bond number, representing the ratio between the buoyancy forces and the surface tension equals to 4. For both heat exchangers, the Bond number is found to be greater than 4, – around 13 for PHE 1 and PHE 2– implying a macro-scale phenomenon. Therefore, the dependency of the heat transfer coefficient on the chevron angle is lower than what could be obtained in the micro-scale case as it can be seen in Equation ***(3-27)***.

Regarding the condenser heat transfer coefficient, it can be divided into a convective and a gravitational component, based on the value of the liquid Weber number, which represent the ratio between the fluid inertia and the surface tension. The Weber number at the computed optimum operating point is 0.0026 and 0.001 for PHE 1 and PHE 2, respectively, way lower than the 0.12 threshold,

and implying a strong dependency on the gravitational component. Moreover, by computing Θ in Equation (3-31), it appears that the heat transfer coefficient almost only depends on the gravitational term, with Θ being equal to 0.02 and 0.008 for PHE1 and PHE2, respectively. This means that a consequent part of the heat exchanger surface is in direct contact with the working fluid vapor rather than being wetted with a liquid film (Tao & Ferreira, 2020).

3.5.2.3. Comparison with results from the literature and temperature difference dependency

The maximum net power output is also computed for different temperatures and compared with the data from Uehara & Ikegami (1990), which is shown in Figure 3-4. The trend is the same as what was found in Chapter 2, and is consistent with the data from Uehara & Ikegami (1990). By including the working fluid side heat transfer coefficient and pressure drop, results are a lot closer to other optimization results.

The result obtained by Bernardoni et al. (2019) – 167 W/m^2 – is slightly higher than what was computed for PHE 1 and PHE 2 at a temperature difference of 20 K and 21 K, respectively.

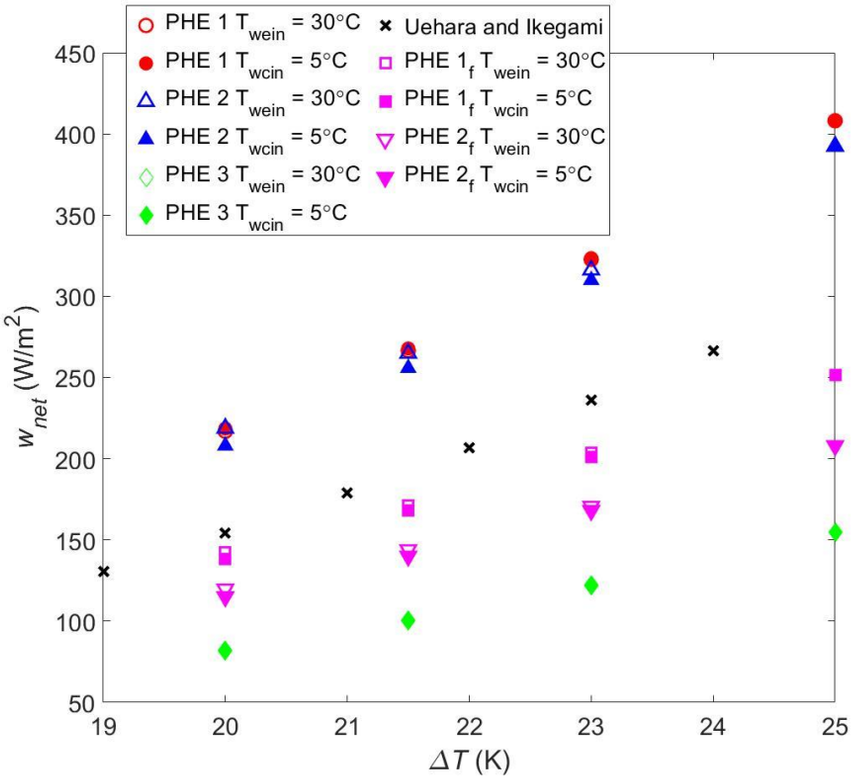

Figure 3-4: Maximum net power output per square meter of heat transfer area as a function of the seawater temperature difference, including results considering working fluid side heat transfer coefficients and pressure drop.

3.5.3. Geometry design parameter optimization

As specified in previously, the advantage of using a global correlation is the possibility of comparing heat exchangers with various geometry designs. The goal of this section is to investigate which plate heat exchanger design parameters are the most suitable for an OTEC power plant. Chevron angle, mean channel spacing, corrugation pitch, and aspect ratio defined in Figure 1-10 and Figure 1-11 are investigated. The default plate is based on PHE 1, then design parameters are changed one at a time.

3.5.3.1. Chevron angle

One of the main feature of plate heat exchanger is the surface treatment. Because of the nature of the correlations, which are based on chevron angles and enlargement factors, only herringbone type plate heat exchanger such as PHE 1 and PHE 2 are investigated. Before doing so, correlations equation must be closely analyzed. The seawater Nusselt number correlation for chevron angle ranging from 1° to 90° for a constant Reynolds number is given in Figure 3-5, on which

correlation limitation are materialized by vertical red lines. The correlation includes a polynomial function of β as well as a sinusoidal function of β in the Reynolds number exponent, which can yield disputable results out of the validity range. Indeed, it is found that the validity range coincide with the rising edge of the correlation. Applying the correlation too far from its validity range will coincide with the falling edge of the correlation, which may not be an accurate description of the physical phenomenon. Even using a chevron angle of 72°, as it is the case with PHE 1, can be disputable, even though Figure 3-2 showed a similar percentage error between Muley & Manglik's (1999) correlation and Kushibe & Ikegami's (2006) correlation when using PHE 1 with a 72° chevron angle and PHE 2 with a 30° chevron angle.

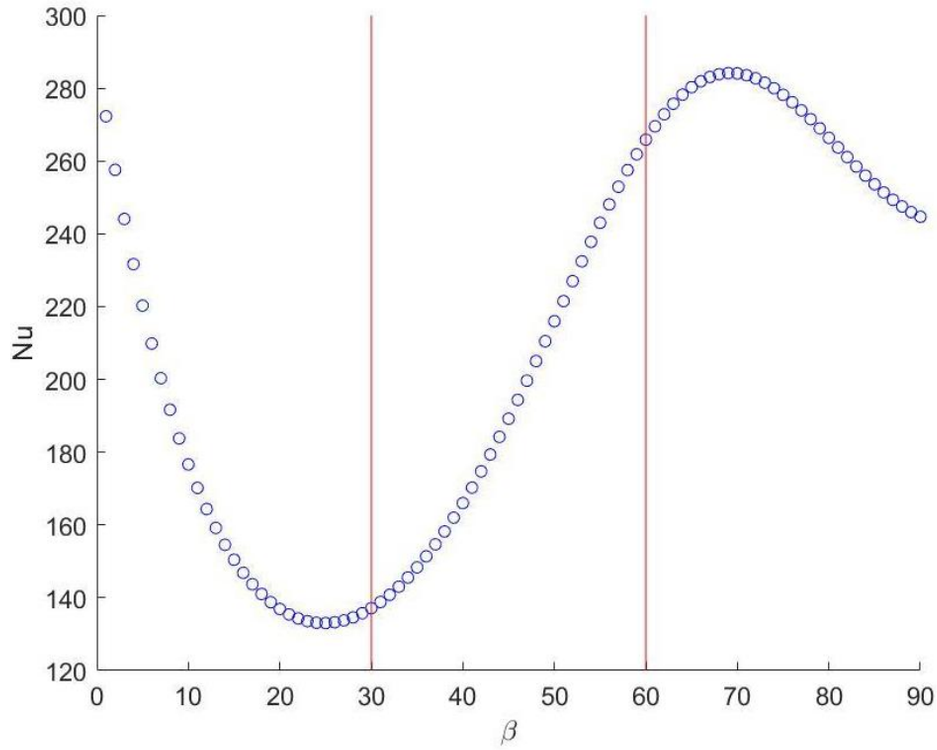

Figure 3-5: Seawater Nusselt correlation at a constant Reynolds number for a chevron angle ranging from 1° to 90°.

Regarding the seawater friction factor, however, the function does not present such an abrupt variation as shown in Figure 3-6, and assuming the correlation to be valid for values within a reasonable range outside of its normal limitation may be a possibility.

Similarly, such an assumption may be possible for the boiling Nusselt and friction factor correlations as the chevron angle dependency is fairly straightforward as seen in Equation (3-7) and (3-27).

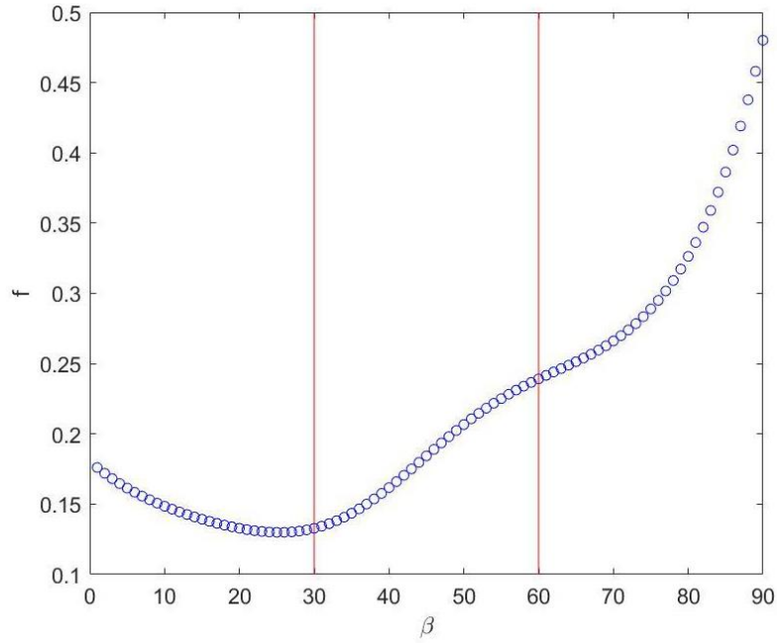

Figure 3-6: Seawater friction factor correlation at a constant Reynolds number for a chevron angle ranging from 1° to 90°.

For the condenser, however, as specified previously, the experimental data on which the heat transfer coefficient and pressure model are based uses a single active plate with a chevron angle of 62° as a heat exchanger. Looking closer at the Equations (3-31), (3-32), (3-36) and (3-38), it appears that only the convective condensation term depends on the chevron angle. Besides, this component was found to have a rather low impact on the overall condensation heat transfer coefficient. Practically, for PHE 1 and PHE 2, the gravitational condensation term was found to be higher than the convective condensation term by several orders of magnitudes.

The chevron angle optimization was carried out for chevron angles ranging from 30° to 72° as seen in Figure 3-7, and optimum values are found for chevron angles of 70° and 68° for the evaporator and condenser, respectively. This only corresponds to an increase of 0.6% in the net power output to heat transfer area ratio. It should be reminded, however, that the base plate, PHE 1, presented chevron angles very close to the optimum. These results do include out of bounds values for the seawater Nusselt number correlation. The heat transfer coefficient,

and, therefore, the maximum net power output, is likely to be underestimated as the chevron angle increases from 60°. Thus, it is very likely that the found optimum does lead to a higher maximum net power output than the 60° - 60° case which would be the optimal point in the strict validity range of the correlation. What remains unknown, however, is whether the maximum net power output increases along with the chevron angle or if an optimum actually exist. A correlation valid on a wider range of values would be needed to further investigate this matter.

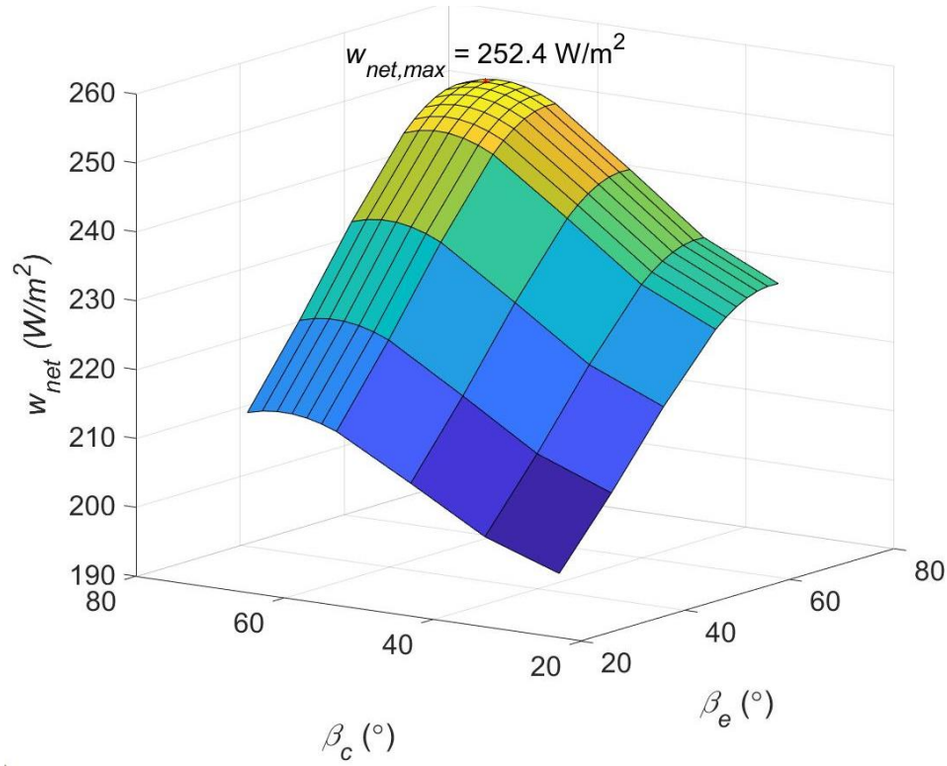

Figure 3-7: Maximum net power output per square meter of heat transfer area as a function of the chevron angles of both the evaporator and condenser.

3.5.3.2. Mean channel spacing

The mean channel spacing is another important design parameter for plate heat exchangers. For seawater correlations, experimental data are based on plates with a mean channel spacing δ of 2.54 mm. This mean channel spacing is used to calculate the enlargement factor, equivalent diameter and heat exchanger channel cross surface area and, although there is no validity range on the mean channel spacing for the seawater correlations, one does exist for the enlargement factor, which spans from 1 to 1.5. The maximum mean plate spacing for a given Λ can de deduced by solving Equation (3-2) for an enlargement factor ϕ equal 1.5. This was done using the Matlab function "fsolve", which can solve nonlinear equation of the

form f(x) = 0. Then, this result is used together with Equation (3-3) to find the maximum mean channel spacing value, which was computed to be 7.7 mm for a corrugation pitch Λ of 15 mm. Compared to chevron angles, for which heat exchangers with values beyond the correlations validity range exist, it is difficult to manufacture plate heat exchangers with an enlargement factor greater than 1.5 (Muley & Manglik, 1999).

Regarding the boiling correlations, enlargement factors of the experimental database varied from 1.04 to 1.53 and mean channel spacing from 1 mm to 4 mm. For the condenser, the plate heat exchanger presented a mean channel spacing of 1.72 mm.

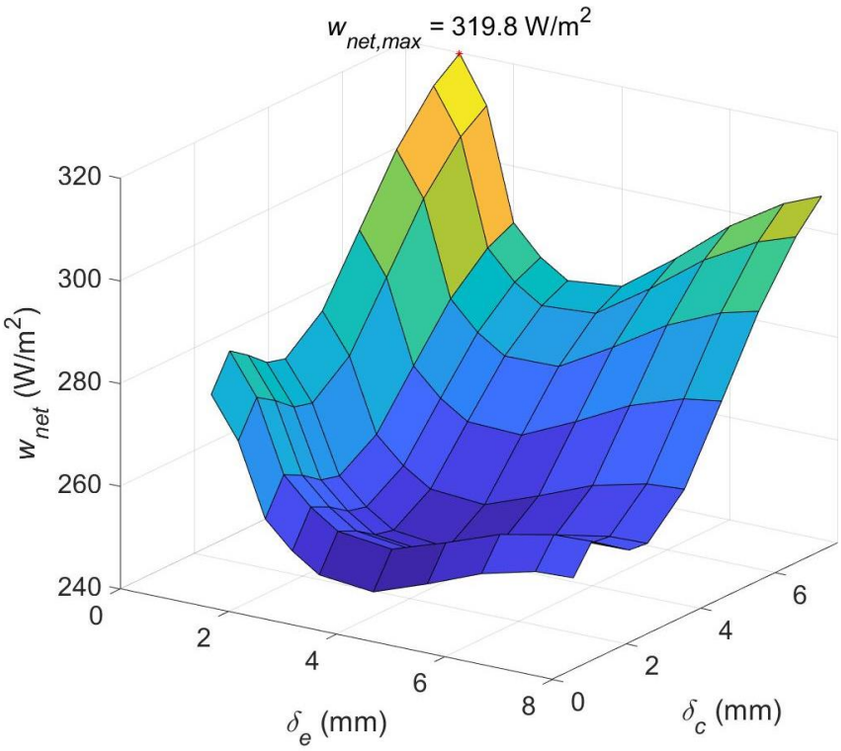

Figure 3-8: Maximum net power output per square meter of heat transfer area as a function of the mean channel spacing δ.

Assuming all correlations valid within the 1 mm to 7.7 mm range, Figure 3-8 shows the results of the optimization. The highest maximum net power output – 320 W/m² – is obtained for 1 mm and 7.7 mm for the evaporator and the condenser, respectively. Compared with PHE1, which presents a mean channel spacing of 4 mm that coincide with a rather low value when looking at the graph, it represents a significant 27% increase in the maximum net power output of the OTEC system.

In the evaporator, the seawater heat transfer coefficient shown in Figure 3-9 increase reaches a minimum for a mean channel spacing, δ_e, between 2 and 4 mm, and increases as δ_e increases or decreases from this minimum, with a highest heat transfer coefficient at a δ_e of 7.7 mm. The seawater pressure drop, however increases as δ_e decreases as seen in Figure 3-10. The working fluid heat transfer coefficient represented in Figure 3-11, however increases as δ_e decreases. The combined effect of the high working fluid heat transfer coefficient, and relatively high seawater heat transfer coefficient when δ_e is around 1 mm results in an optimal value δ_e of 1 mm for the evaporator despite the high pressure drop.

For the condenser, as seawater correlations do not differ, the trend of the heat transfer coefficient and pressure drop is very similar to what is represented in Figure 3-9 and Figure 3-10 for the evaporator, with a highest value of heat transfer coefficient and lowest value of pressure drop reached for a condenser mean channel spacing, δ_c of 7.7 mm. Moreover, the working fluid mass flow rate strongly depends on δ_c, as seen in Figure 3-12. The increase of the mass flow rate due to the increase of δ_c induces a higher net power output to heat transfer area ratio. As the only the negative effect of a high δ_c is the lower values of working fluid heat transfer coefficient that are reached as seen in Figure 3-13, the optimum condenser mean channel spacing value of 7.7 mm is easily conceivable. It should be noted that the working fluid mass flow rate in Figure 3-12 also depends on δ_e, however, a low value of δ_e also results on a relatively high m_f.

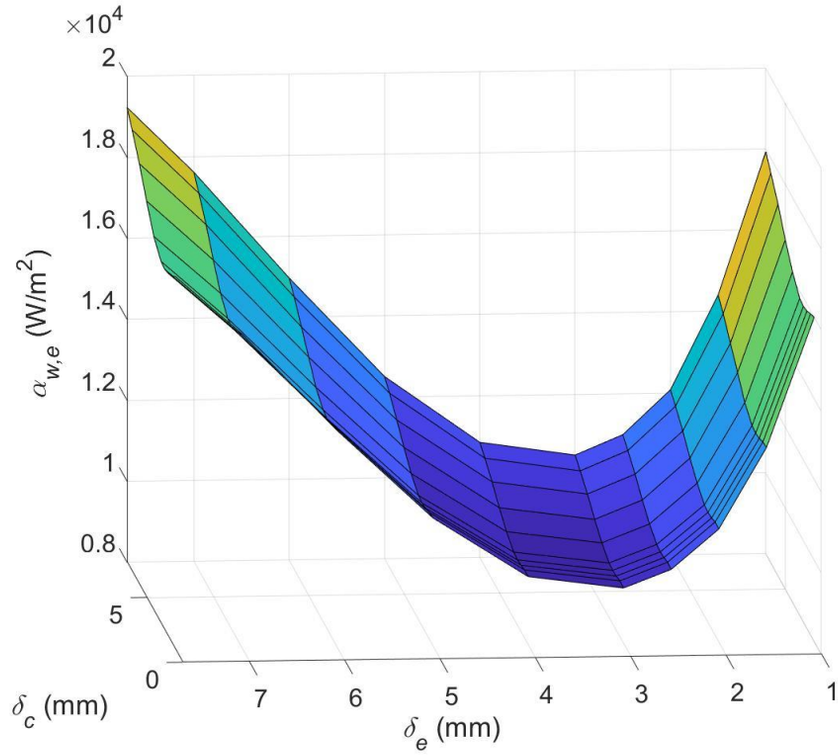

Figure 3-9: Seawater heat transfer coefficient in the evaporator as function of the mean channel spacing of both heat exchangers.

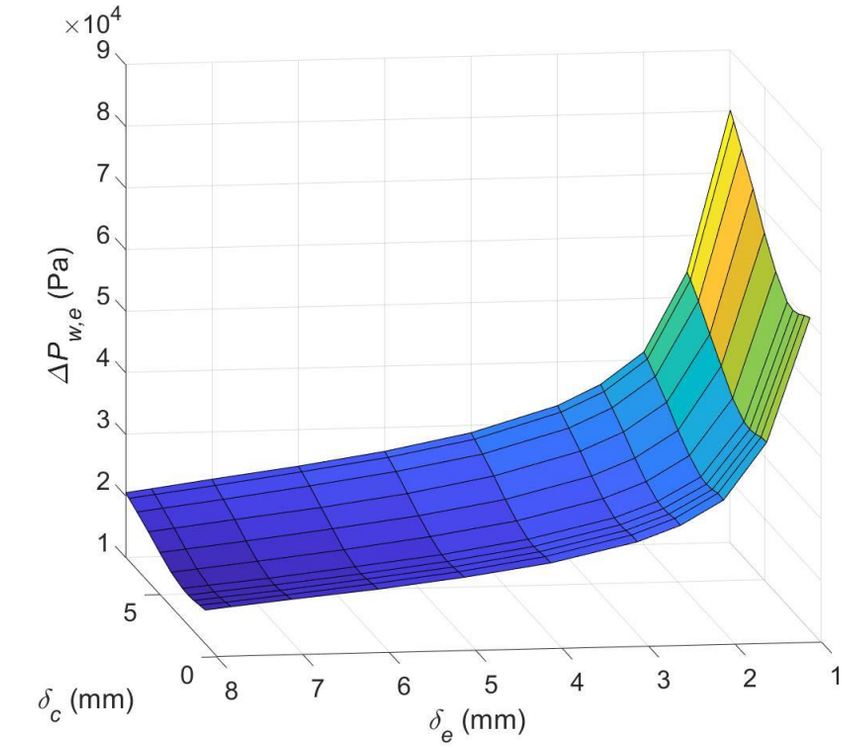

Figure 3-10: Seawater pressure drop in the evaporator as a function of the mean channel spacing of both heat exchangers.

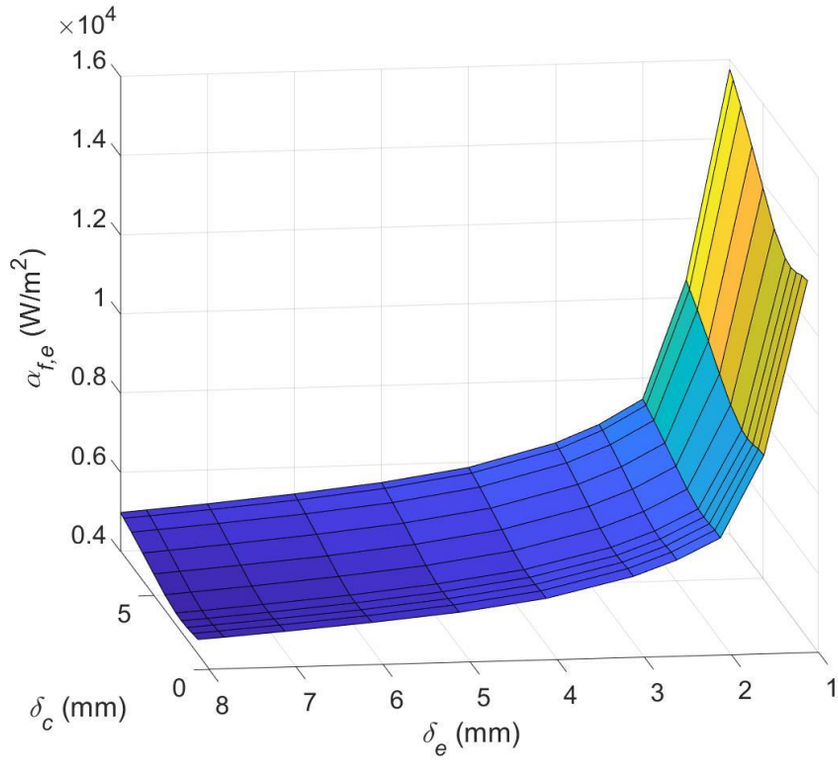

Figure 3-11: Working fluid heat transfer coefficient in the evaporator as a function of the mean channel spacing of both heat exchangers.

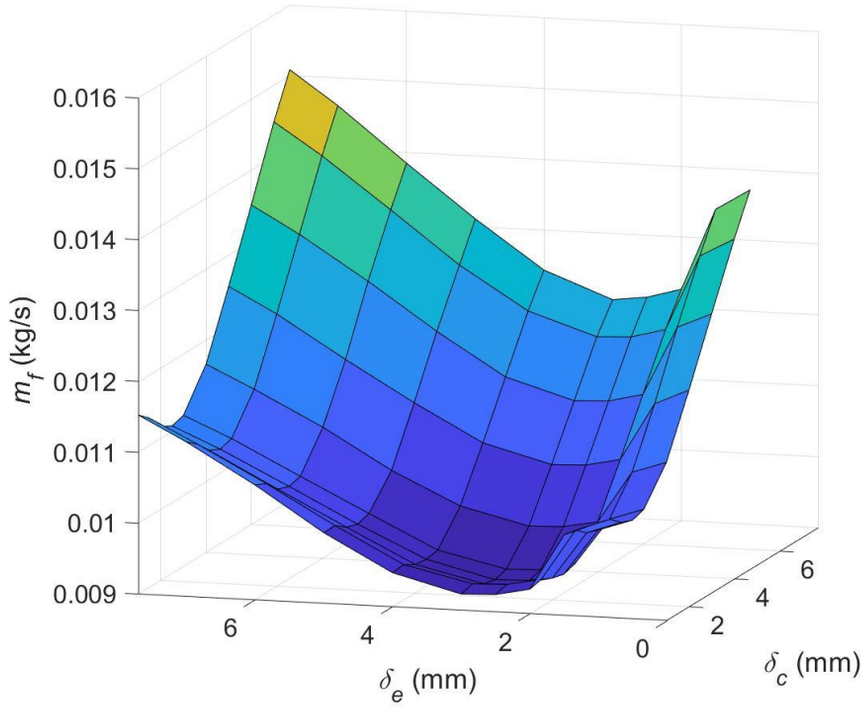

Figure 3-12: Working fluid mass flow rate as a function of the mean channel spacing of both heat exchangers.

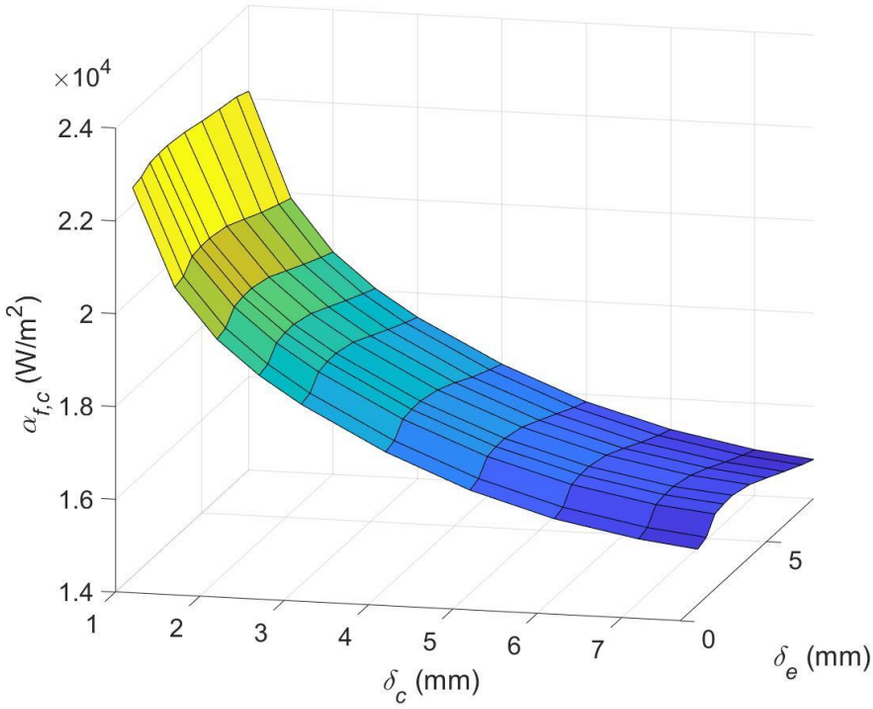

Figure 3-13: Working fluid heat transfer coefficient in the condenser as a function of the mean channel spacing of both heat exchangers.

3.5.3.3. Corrugation pitch

The corrugation pitch, also known as the corrugation wavelength is the second parameter that determines the value of the enlargement factor ϕ. As for the mean channel spacing, for seawater correlations, the validity range is limited by the enlargement factor The enlargement factor ϕ value of 1.5 mm corresponds to a minimum corrugation pitch of 7.7 mm for a mean channel spacing of 4 mm. The actual value of corrugation pitch of the plate heat exchanger used in the experiment was 9 mm (Muley & Manglik, 1999).

Regarding working fluid correlations, the experimental database for the boiling correlations, it regroups plate heat exchangers with corrugations pitch ranging from 3.7 mm to 12 mm, whereas the condensation correlations are based on a plate heat exchanger with a corrugation pitch of 6.67 mm(Amalfi et al., 2016b; Tao & Ferreira, 2020).

The optimization is realized with a corrugation pitch between 7.7 mm and 15 mm, the latter being the corrugation pitch of PHE 1. Results are given in Figure 3-14.

An optimum of 260 W/m² is found for the corrugation pitch of 10 mm and 10.5 mm for the evaporator and the condenser, respectively. This represent a 3.6% increase compared to PHE1.

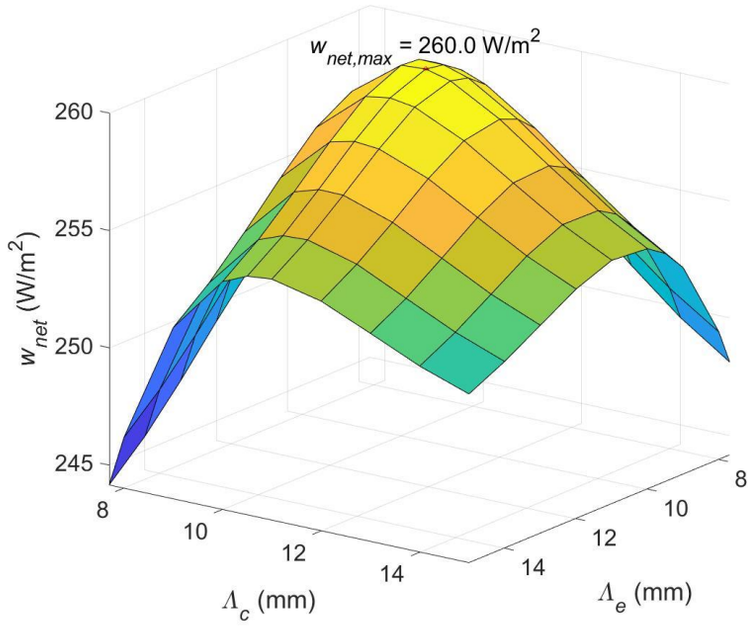

Figure 3-14: Maximum net power output per square meter of heat transfer area as a function of the corrugation pitch, Λ, of both the evaporator and condenser.

As shown in Figure 3-15, the decrease in the corrugation pitches of both the evaporator and condenser lead to the increase of the working fluid mass flow rate in a similar way. This tends to increase the net power output of the system but also impacts the evolution of working fluid heat transfer coefficients in both heat exchangers. Indeed, as seen in Figure 3-16 and Figure 3-17 for the evaporator and condenser, respectively, working fluid heat transfer coefficients in a given heat exchanger depends of the corrugation pitches of both the evaporator and condenser in similar magnitude. The working fluid heat transfer coefficient in the evaporator increases as both corrugation pitches decrease, whereas the opposite trend is observed for the condenser. An increase of the working fluid heat transfer coefficient in the condenser as both corrugation pitches increase is observed, although a minimum value is found around a condenser corrugation pitch, Λ_c of 9

mm, from which the heat transfer coefficient slightly increases along with the decrease of. Λ_c. For the seawater side, the evolution of heat transfer coefficients and pressure drops with respect to the corrugation pitches is very similar in both heat exchangers as the same correlation is used. In the seawater case, the evolution of heat transfer coefficients and pressure drop mainly depend on the corrugation pitch of the considered heat exchanger. Graphs for the condenser are reported in Figure 3-18 and Figure 3-19 for the heat transfer coefficient and pressure drop, respectively. Heat transfer coefficient and pressure drop increase along with the corrugation pitch. In summary, the working fluid mass flow rate, working fluid heat transfer coefficient in the evaporator, and seawater heat transfer coefficient in both the evaporator and condenser contribute to an increase of the net power output as corrugation pitches decrease, whereas the seawater pressure drop in both heat exchangers, as well as the working fluid heat transfer coefficient in the condenser contribute to an increase of the net power output as corrugation pitches increase. These two opposite contribution result in the optimum value found in Figure 3-14.

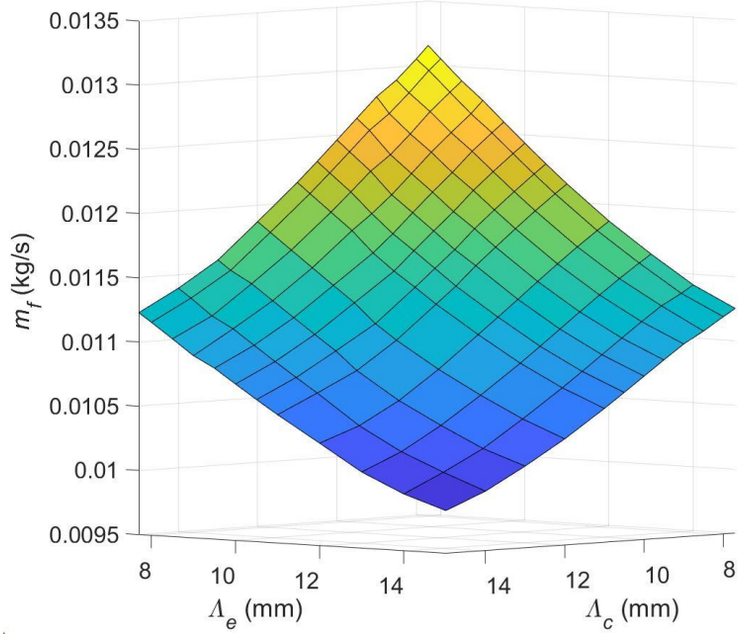

Figure 3-15: Working fluid mass flow rate as a function of the corrugation pitches of both the evaporator and condenser.

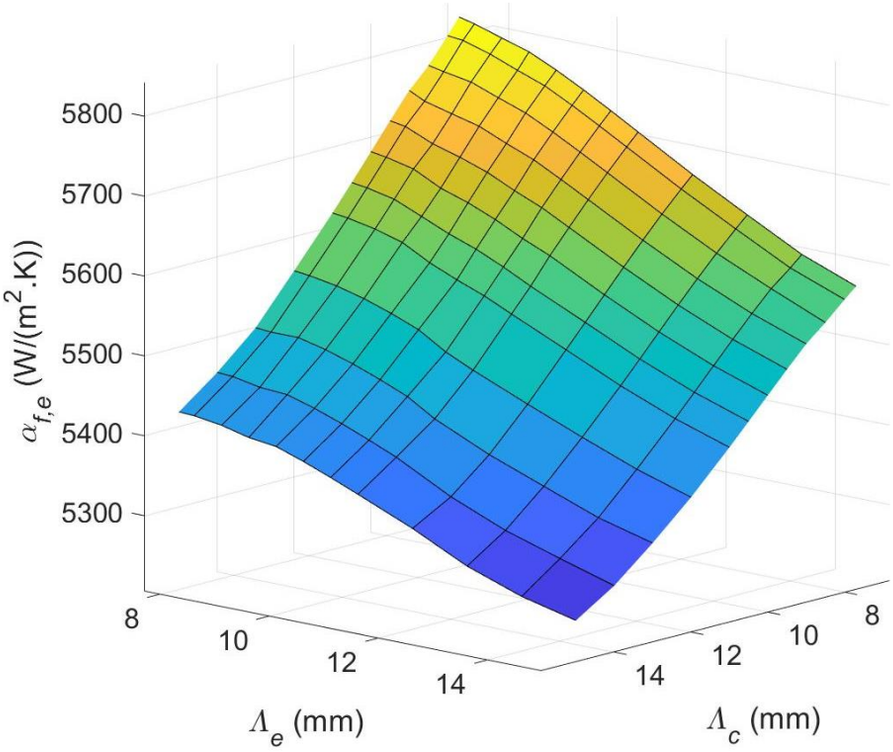

Figure 3-16: Working fluid heat transfer coefficient in the evaporator as a function of the corrugation pitches of both the evaporator and condenser.

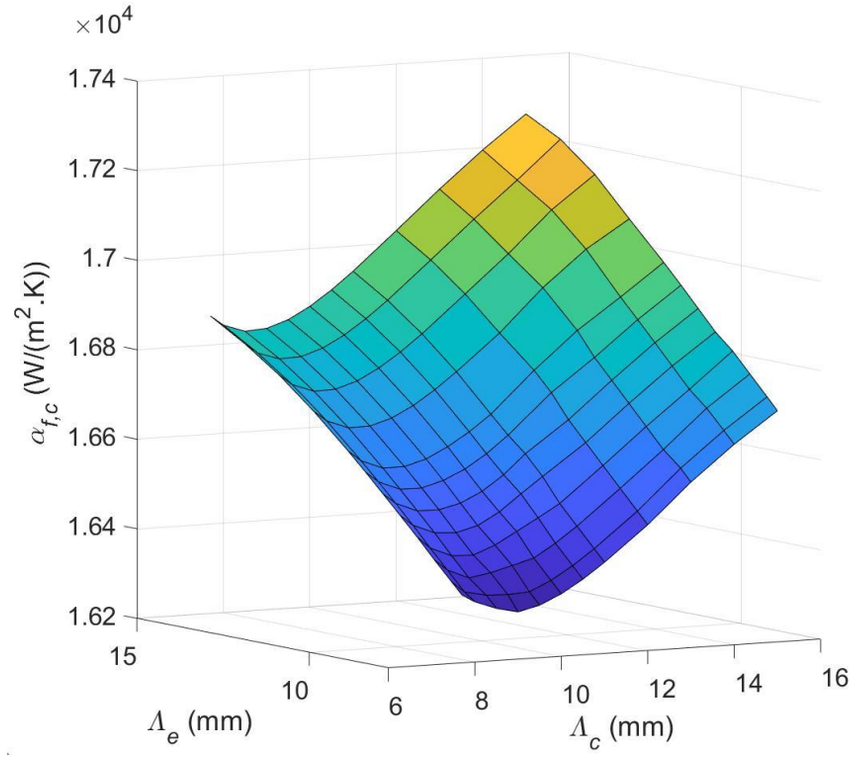

Figure 3-17: Working fluid heat transfer coefficient in the condenser as a function of the corrugation pitches of both the evaporator and condenser.

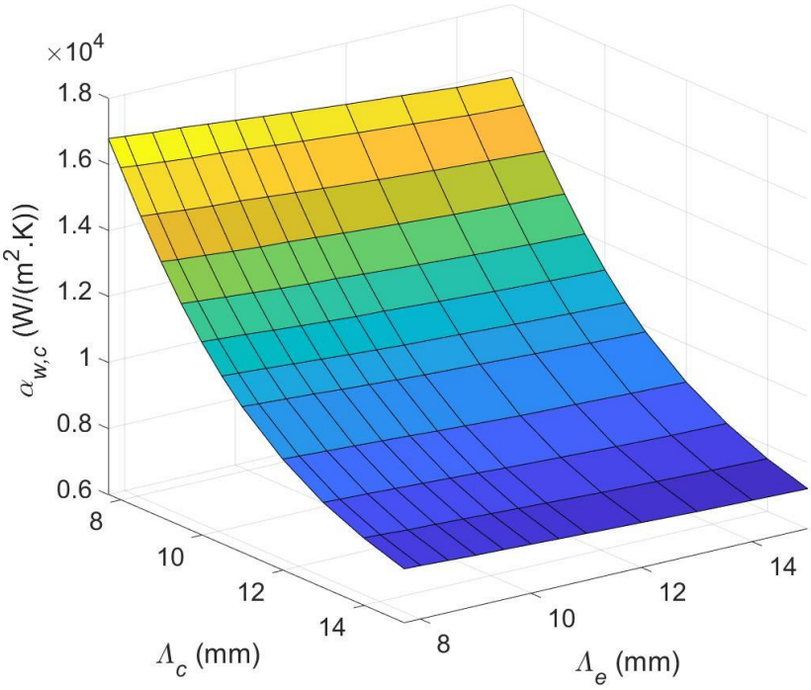

Figure 3-18: Seawater heat transfer coefficient in the condenser as a function of the corrugation pitches of both the evaporator and condenser.

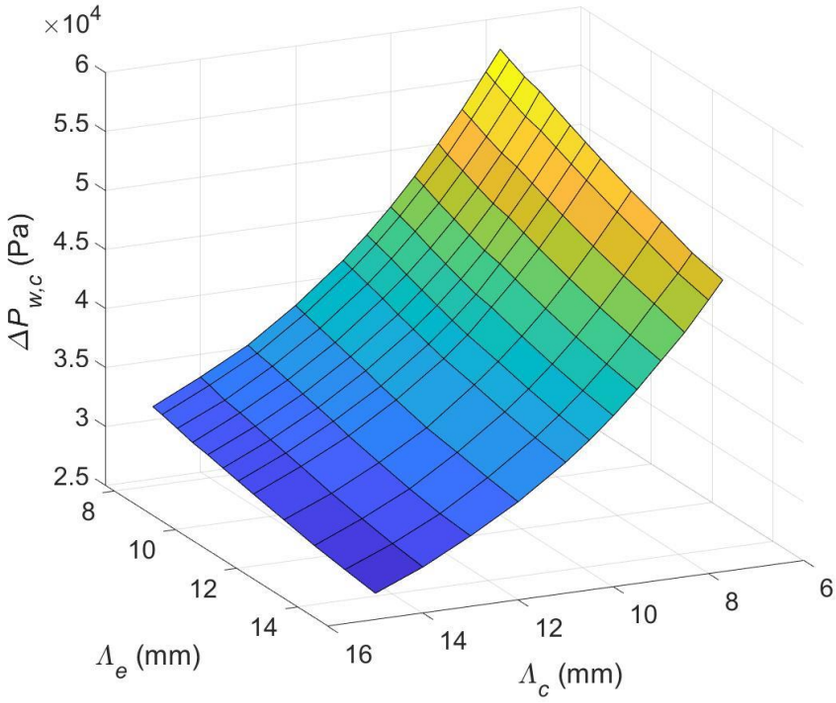

Figure 3-19: Seawater pressure drop in the condenser as a function of the corrugation pitches of both the evaporator and condenser.

3.5.3.4. Aspect ratio

In this section, the aspect ratio, defined as the ratio between the heat transfer length and heat transfer width, is changed for a constant heat transfer area. Correlations should be valid for this value within reasonable ratios. Rather than the actual length and width, the length refers to the dimension parallel to the flow direction, whereas the width refers to the dimension perpendicular to the flow direction. The optimization is realized within a range of 0.2 to 1.6 and 0.2 to 2 for the evaporator and condenser, respectively, and results are given in Figure 3-20. An optimum is found at a ratio of 0.9 for the evaporator, and, for the condenser, the maximum net power output seems to increase along with the aspect ratio without limitation. Practically, however, a certain length is required to allow the heat transfer to take place.

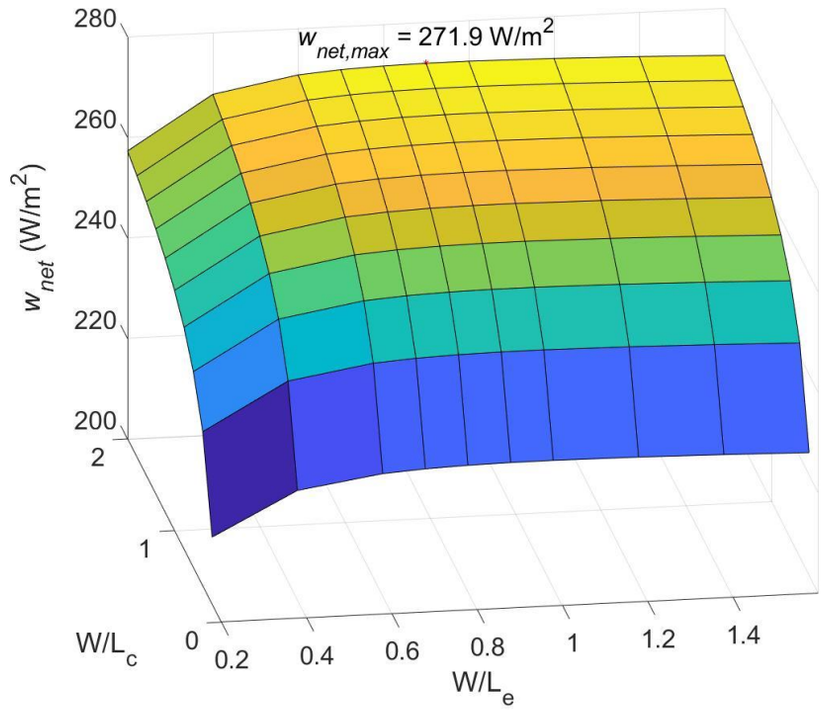

Figure 3-20: Maximum net power output per square meter of heat transfer area as a function of the aspect ratio for both heat exchangers.

For the seawater at a constant velocity within the plate, when the ratio decreases, the heat transfer coefficient as well as friction factor remain the same as it can be seen in Equations (3-5) and (3-26). Only the pressure drop, which becomes a linear function of the plate length, increases. However, as the ratio increases, a higher mass flow rate is allowed for the same velocity within the

plates, which increases both the heat transfer coefficient and the required pumping power. This happens in both the evaporator and condenser, and, because the working fluid pressure drop is negligible, it is possible to conclude from the result in Figure 3-20 that the gain in gross power output is greater than the cold seawater pump power consumption increase, whereas it leads to an optimum value in the evaporator. Indeed, working fluid pressure drop in the condenser has a negligible effect on the net power output to heat transfer area ratio, therefore the increase of the aspect ratio only lead to an increase of the power output.

3.5.3.5. Maximum net power output for the optimum geometry

In this section the optimization is performed again with a plate presenting all the optimum parameters found in this chapter. For the condenser length to width ratio, as no optimum value was found, this parameter is arbitrary fixed at 1. Another issue is the relation between optimum values of the condenser mean channel spacing and corrugation pitch which are 7.7 mm and 10.5 mm, respectively, leading to an enlargement factor ϕ of 1.86, way outside correlations validity range and feasibility. To find out the optimal point, the optimization is realized for mean channel spacing ranging from 1 mm to 7.7 mm and corrugation pitch ranging from the minimum value to get an enlargement factor of 1.5 and 20 mm. Results are given in Figure 3-21.

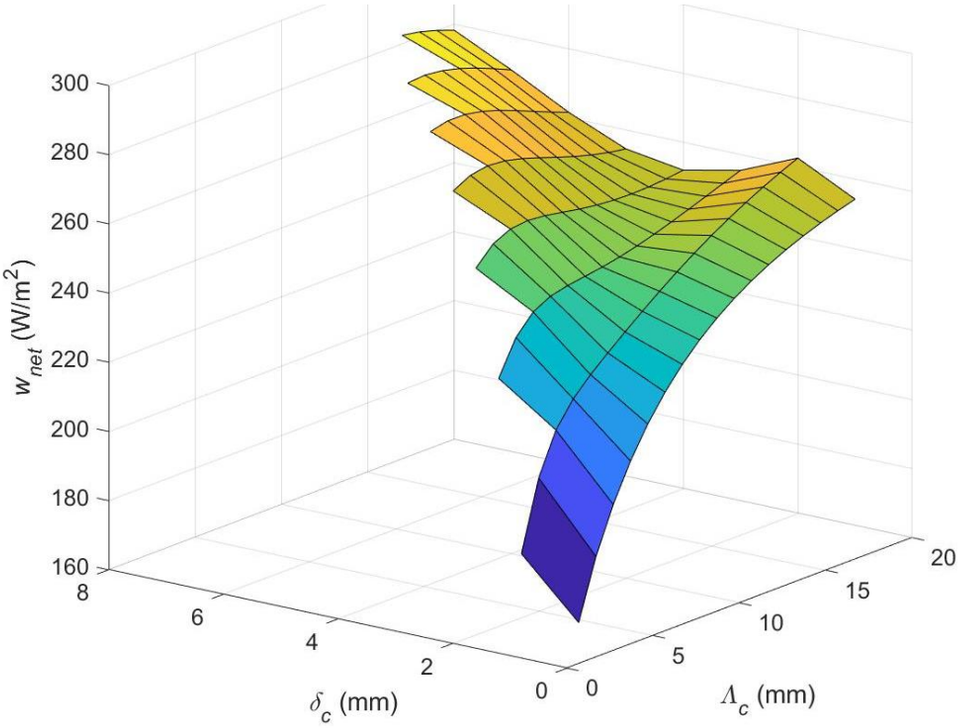

Figure 3-21: Maximum net power output per square meter of heat transfer area as a function of the condenser corrugation pitch Λ_c and mean channel spacing δ_c.

As discussed previously, in the condenser, the net power output to heat transfer area ratio tends to increase as the mean channel spacing increases. However, the optimum value around 10.5 mm for the corrugation pitch is not observed here. Indeed, the optimum corrugation pitch vary along with the mean channel spacing. In fact, at 4 mm, value for PHE 1 on which the geometry is based, the optimum is found at a corrugation pitch of between 10 and 11 mm. In the current case however, the net power output to heat transfer area ratio reach its highest value for the highest δ_c and lowest corrugation pitch considered.

The same is done with the evaporator. Results are summarized in Figure 3-22 in which the same trend as Figure 3-8 can be observed for δ_e. In this case as well, the optimum value of mean channel spacing is conserved, while the optimum corrugation pitch differs. Here the optimum corrugation pitch is found to be the highest one for a δ_e of 1 mm.

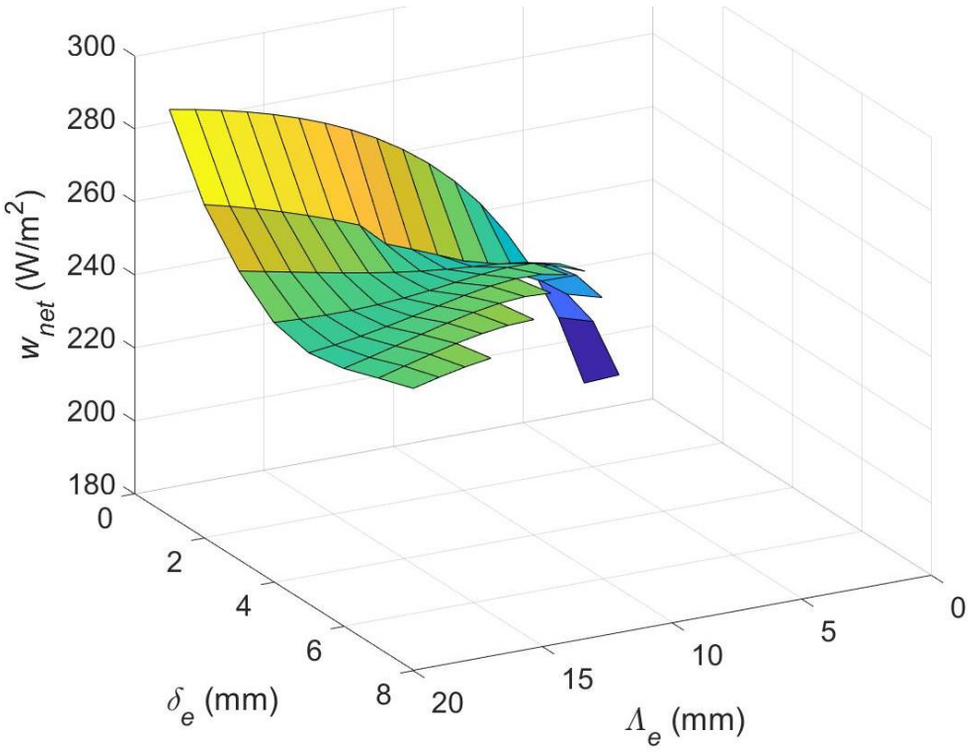

Figure 3-22: Maximum net power output per square meter of heat transfer area as a function of the evaporator corrugation pitch Λ_e and mean channel spacing δ_e

Interestingly, the maximum net power output in the evaporator is found to increase as the enlargement factor ϕ get closer to 1, which would correspond to a smooth plate without any surface treatment whereas, for the condenser, the maximum net power output increases as the enlargement factor gets larger.

Another point requiring further investigation is the plate aspect ratio. Indeed, as discussed previously, the aspect ratio highly depends on the pressure drop within the plates, which itself depends on the plate geometry that is changed when using all optimum parameters. Using the optimum values of chevron angles, mean channel spacing and corrugation pitches given in Table 3-6, the aspect ratio is once more investigated and results are displayed in Figure 3-23. As the enlargement factor of the evaporator gets closer to one, the friction factor decreases as well. This lower friction factor allows for a higher velocity within the plates, and, therefore, a higher mass flow rate. In PHE 1, the increase of the gross power output and pumping power led to an optimum aspect ratio. However, in case of the optimum geometry, as the rate at which the pressure drop increases when the velocity increases is lowered thanks to the low friction factor, the opposite trends do not lead to an optimum, at least within the investigated range.

Table 3-6: Optimum geometry parameters

	Evaporator	**Condenser**
chevron angle β (°)	70	68
mean channel spacing δ (mm)	1	7.7
corrugation pitch Λ (mm)	20	17

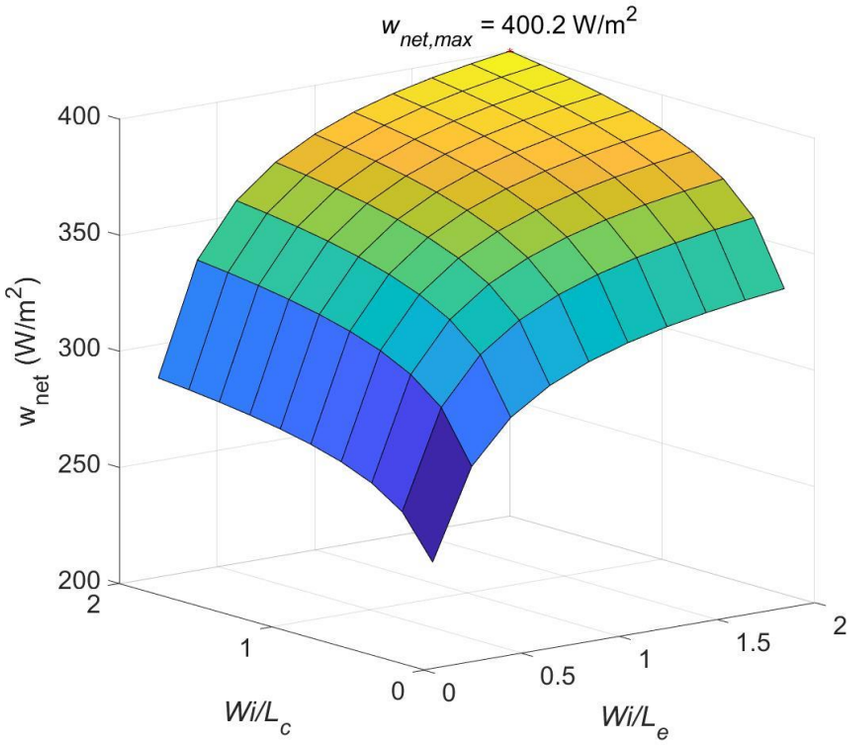

Figure 3-23: Maximum net power output per square meter of heat transfer area as a function of the aspect ratio for both heat exchangers for optimum values of chevron angles, mean channel spacing and corrugation pitch.

Detailed results of the maximum point reached in Figure 3-23 are presented in Table 3-7 in which PHE_{opt} refers to values for the optimum plate heat exchangers with the parameters in Table 3-6 and for aspect ratios of 2. It should be reminded that a finite length is required to drive the heat exchange, and, therefore, more investigations are required concerning actual optimal aspect ratio values. Moreover, actual optimal for both chevron angles is still uncertain and could be higher than the values found previously. Furthermore, the optimum values for the mean channel spacing were found to be at the boundary of the range used within the optimization. Thus, in the condenser, higher values of the mean channel spacing, possibly combined with lower values of the corrugation pitch, might lead to a higher maximum net power output. Similarly, in the evaporator, a higher

maximum net power output might be achieved for lower values of mean channel spacing and/or higher values of the corrugation pitch. These were not investigated as doing so would be too far from the correlations initial validity range.

The maximum net power output for the optimum geometry parameters from Table 3-6 is found to be 400.2 W/m^2, which represent a considerable 59% increase compared with the value obtained for PHE 1. In case of the optimum geometry, except for the working fluid side of the condenser, heat transfer coefficients are higher than those of PHE 1. Also, the seawater and working fluid heat transfer coefficients are more balanced with a ratio of 0.76 and 0.77 compared with 0.54 and 0.42 with PHE 1 for the evaporator and condenser, respectively. The pressure drop of both fluids in the evaporator greatly increases, especially the working fluid side, which is explained by the higher working fluid mass flow rate. The friction factor, however greatly decreased, mainly thanks to the low enlargement factor. In the condenser, as the optimum enlargement factor is high, the friction factor increased. The decrease in the pressure drop is explained by the lower velocity inside the plate as well as the increased hydraulic diameter.

Table 3-7: Optimization result at optimum geometry compared with PHE1.

Parameter	Value	
	PHE_{opt}	**PHE1**
$w_{net,max}$ (W/m^2)	400.2	251.4
m_f (kg/s)	0.0158	0.0098
$m_{w,e}$ (kg/s)	1.481	1.243
$Re_{w,e}$	3273	5 014
$v_{w,e}$ (m/s)	1.378	0.528
$m_{w,c}$ (kg/s)	3.476	1.270
$Re_{w,c}$	4083	2 724
$v_{w,c}$ (m/s)	0.418	0.537
T_e (K)	295.3	295.5
T_c (K)	283.5	283.8
x_e (-)	0.52	0.52
x_c (-)	0.49	0.49
α_{we} (kW.m^{-2}.K^{-1})	18.00	9.825
α_{wc} (kW.m^{-2}.K^{-1})	11.95	7.217
α_{fe} (kW.m^{-2}.K^{-1})	13.68	5.257
α_{fc} (kW.m^{-2}.K^{-1})	15.50	17.27
ΔP_{we} (kPa)	35.04	22.61
ΔP_{wc} (kPa)	11.63	27.25
ΔP_{fe} (kPa)	27.99	5.01
ΔP_{fc} (kPa)	0.013	0.217
f_{we}	0.034	0.286
f_{wc}	0.677	0.331
f_{fe}	3.171	13.48

3.5.4. Conclusion

There were two main goal to this section. The first one was to improve the previous method accuracy by taking into account the working fluid pressure drop and heat transfer coefficient. The second goal was to achieve a comparison of plate heat exchangers design parameters by replacing heat exchanger specific correlations with global correlations. A new objective function was derived and the method in Chapter 2 was adjusted to be applicable to the new optimization specificities. A comparison of the global correlations for seawater was performed and the method was then applied to two of the heat exchangers presented in Chapter 2 for comparison purposes. Afterwards, an optimization of the plate heat exchanger design parameters was performed and the maximum net power output as well as optimum parameters were computed and compared with the original plate, PHE 1.

- A significant difference was found between heat exchanger specific correlations and global correlations. However, these differences did not seem to have a major impact on the maximum net power output of the system.
- The maximum net power output for PHE 1 and PHE 2 were found to be almost halved as the working fluid heat transfer coefficients and pressure drops were considered, and most of the assumptions taken in Chapter 2 were found to be invalid, although the most suitable heat exchanger remained the same. The trend of the variation of the maximum net power output as a function of the temperature difference was also found to be consistent with the optimized values from Chapter 2 and data from the literature.
- The maximum net power output was found to increase along with the chevron angle up to an apparent optimum of 70° and 68° for the evaporator and the condenser, respectively. However, due to the form and validity range of the seawater correlations equations, it was suspected that the maximum net power output was more and more underestimated as the chevron angle increases from 60°, and,

therefore, that the actual optimum, if any, was likely to be at higher chevron angles.

- For the mean channel spacing, results differed for the evaporator and the condenser. The former found an optimum value at the minimal computed value of 1 mm, whereas the latter has an optimum at the maximal computed value of 7.7 mm. Once more, a higher net power output might be achieved for values below 1 mm or 7.7 mm, but the correlations validity range could not allow to investigate it properly.
- Optimum corrugation pitch was found to be highly dependent on the mean channel spacing; drastically different results were found using the mean channel spacing of 4 mm of PHE 1 and other values. In place of an optimum corrugation pitch, an optimum set of corrugation pitch and mean channel for both the evaporator and condenser were found.
- An optimum of 0.9 was found for the aspect ratio of PHE 1 at the evaporator but not for the condenser, because of the negligible pressure drop of the working fluid. The maximum net power output was found to increase without limit along with the width, as it allows for a higher flow rate inside the heat exchanger. For a plate with optimum geometry, no optimum was found, even for the evaporator. as the decrease of the working fluid friction factor diminished the increase rate of the pumping power as the mass flow rate increases.
- OTEC system net power output to heat transfer area ratio appeared to increase as the plate in the evaporator got closer to a smooth plate with an enlargement factor close to 1 because of the relatively high working fluid pressure drop, whereas in the condenser, a high enlargement factor was preferred.
- The plates using the optimum geometry led to an increase in the maximum net power output of 59% compared with the original PHE 1. An increase of almost all heat transfer coefficients was observed with a closer balance between heat transfer coefficient of both sides.

Although an important increase of the maximum net power output was achieved using the optimized plate, more accurate correlations applicable to a wider range of design parameters would allow further investigation, especially when no optimum were found. Namely, an investigation focused on the optimal length to width ratio is required to see to what extend the increase of the width in the condenser would lead to an increase of the maximum net power output. This is also true for the mean channel spacing as experimental data on which correlations are based did not include values higher than 4 mm.

Chapter 4.

BOILING HEAT TRANSFER COEFFICIENT USING COMPUTATIONAL FLUID DYNAMICS

The accuracy of the optimization realized in the previous chapter strongly depends on the accuracy of the heat exchangers' heat transfer coefficient and pressure drop correlations. These correlations were derived from experimental data that cover a certain range of parameters. To get a more accurate optimization, heat exchanger specific correlations are required. However, a study on the effect of each geometry design parameter, as done in the previous chapter, is unrealistic

due to the number of plates that would need to be manufactured to obtain experimental data.

The goal of this section is to suggest a solution to obtain accurate correlations specific to a heat exchanger without the hurdle and the cost of an experiment. Computational Fluid Dynamics (CFD), as described in section 1.3 of Chapter 1, is a promising tool to achieve this goal. A model is firstly developed based on the flow boiling of water in a smooth rectangular duct and compared with the experimental data from Phillips (2014) as well as the model developed by Gilman & Baglietto, (2017). Then, using a slightly modified geometry, and replacing water by ammonia, the model is applied to a flow that is consistent with OTEC conditions.

4.1. Geometry and mesh

The geometry used for the simulation of the flow boiling of water in a smooth rectangular duct is based on the experiment realized by Phillips (2014) and was created using Ansys DesignModeler. The duct is 1.18 m long, 30 mm width and has a clearance of 10 mm as shown in Figure 4-1. At 1.06 m of the duct, a heating surface of 20 mm x 10 mm is used to provide the necessary heat to trigger the boiling phenomena. Such a long geometry is used to be as close as possible to the experiment and to ensure a fully developed flow at the heating surface.

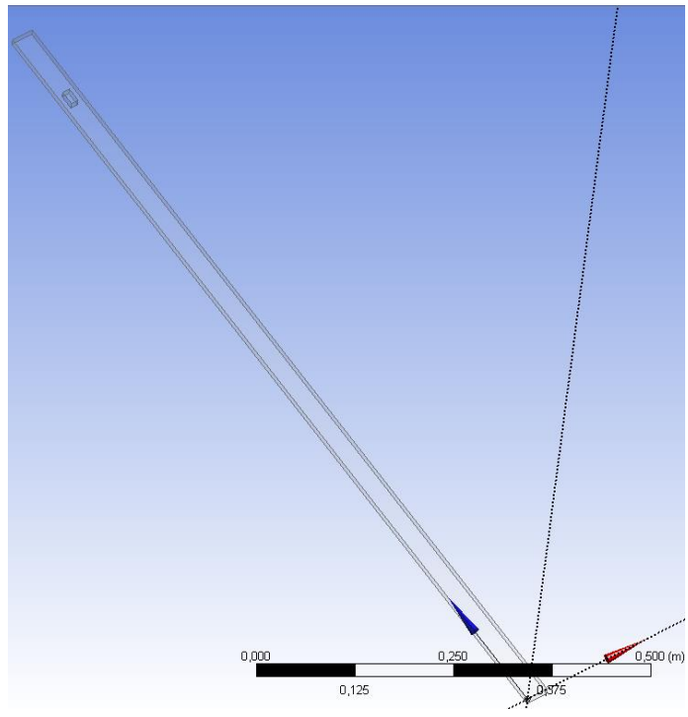

Figure 4-1: Geometry of the rectangular duct.

The mesh is generated through Ansys meshing, and, after a mesh analysis reported in Figure 4-2, a final mesh using a body sizing of 1.2 mm along with a sweep method with 40 divisions and a bias of 10 to better capture the heat transfer phenomena within the boundary layer is selected. The resulting final mesh is shown on Figure 4-3 with 1 050 502 nodes and 984 520 elements. A smaller size mesh was not used as the temperature value started to drastically drop even with a slight change in the mesh size, as seen in Figure 4-2.

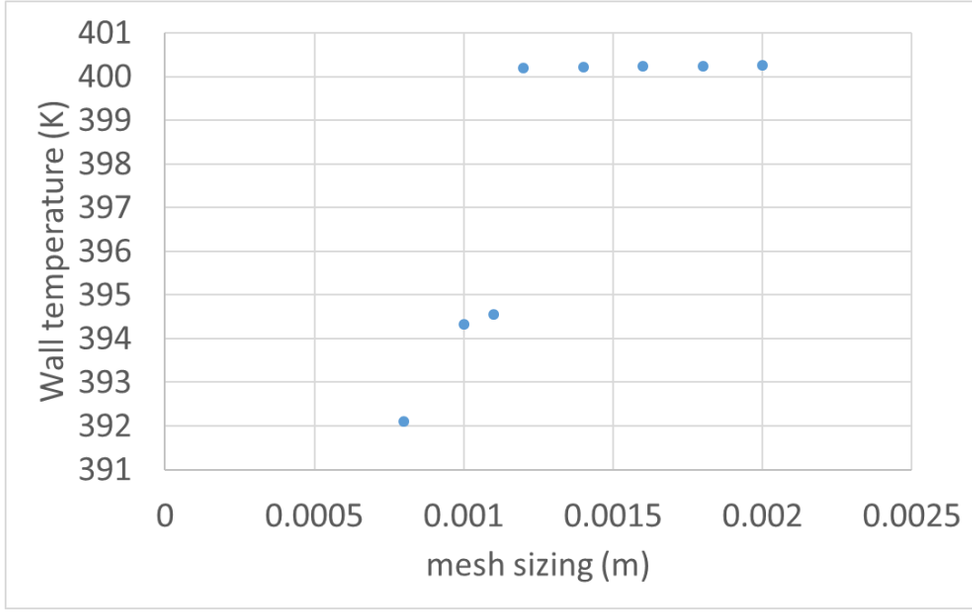

Figure 4-2: Mesh sensitivity analysis.

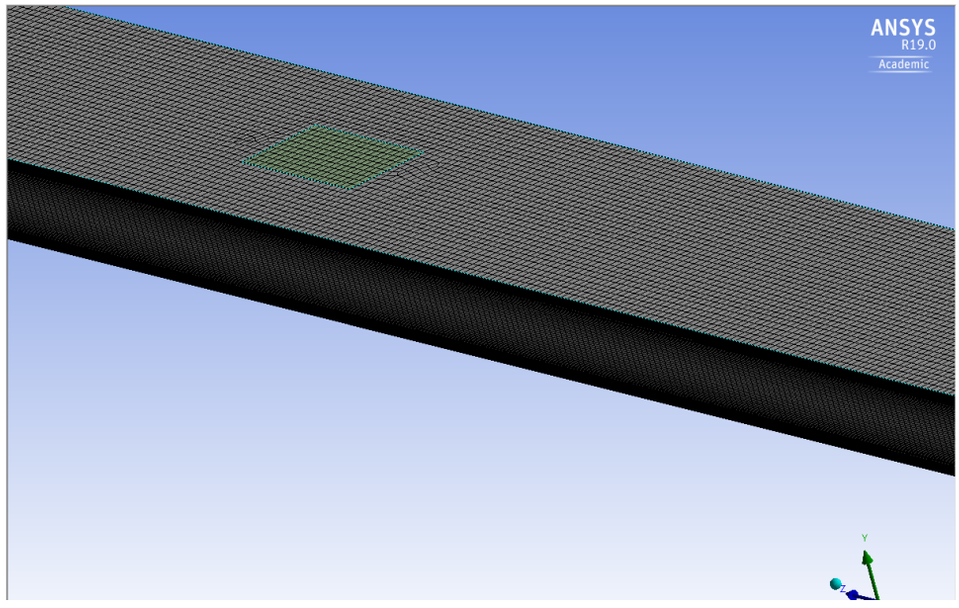

Figure 4-3: Mesh output for the rectangular duct geometry.

4.2. Model description

4.2.1. Mass and momentum conservation equations

The Two phase flow is simulated with a Eulerian – Eulerian approach and uses the RPI wall boiling model for the phase change and phase interactions. As described previously, with the Eulerian – Eulerian approach, momentum and mass conservation equations are solved for each phases. For a given phase p, Equations (4-1) and (4-2) apply (Ansys®, 2018b):

$$\frac{\partial}{\partial t}(\alpha\rho_p) + \nabla \cdot (\alpha_p \rho_p \vec{v}_p) = \dot{m}_r - \dot{m}_g \tag{4-1}$$

with α, the volume fraction, ρ, the density, v, the velocity, $\dot{m}_{g,r}$, the mass given or received to/from the other phase.

$$\begin{aligned}\frac{\partial}{\partial t}(\alpha\rho_p \vec{v}_p) + \nabla \cdot (\alpha_p \rho_p \vec{v}_p \vec{v}_p) \\ = -\alpha_p \nabla P + \nabla \bar{\bar{\tau}}_p + \alpha_p \rho_p \vec{g} + \vec{R} + \dot{m}_r \vec{v}_r - \dot{m}_g \vec{v}_g + \vec{F}_p + \vec{F}_{lift,p} \\ + \vec{F}_{wl,p} + \vec{F}_{td,p}\end{aligned} \tag{4-2}$$

With g, the gravitational acceleration, $\overrightarrow{F_p}$, an external body force equal to zero in the current simulations, $\vec{F}_{lift}$, a lift force, $\vec{F}_{wl}$, a wall lubrication force, $\vec{F}_{td}$, a turbulent dispersion force. The two velocities $\vec{v}_r$ and $\vec{v}_g$ are defined as the velocity of one or the other phase. If $\dot{m}_g$ is positive, $\vec{v}_g$ is equal to the velocity of the phase p, otherwise, it is equal to the velocity of the other phase. If $\dot{m}_r$ is positive, $\vec{v}_r$ is equal to the velocity of the other phase, otherwise, it is equal to the velocity of the phase p. R and τ are defined in Equations (4-3) and (4-4), and are the interaction force between the two phases and the phase stress-strain tensor, respectively(Ansys®, 2018b):

$$\tau = \alpha_p \mu_p \left(\nabla \vec{v}_p + \nabla \vec{v}_p^T\right) + \alpha_p \left(\kappa_p - \frac{2}{3}\mu_p\right) \nabla \cdot \vec{v}_p \bar{\bar{I}} \tag{4-3}$$

where μ_p and κ_p are the shear and bulk viscosity of the phase p, respectively. $\bar{\bar{I}}$ is the identity tensor.

$$\vec{R} = K_{qp}(\Delta \vec{v}) \tag{4-4}$$

With K_{qp} the interphase momentum exchange coefficient for which the definition is given in Equation (4-5), and $\Delta\vec{v}$, the difference between the velocity of the other phase and the phase p.

$$K_{qp} = \frac{3\mathrm{f}A_i\mu_p}{d_q} \tag{4-5}$$

with d_d, the bubble diameter, f the drag function, and A_i, the interfacial area defined by Equation (4-6) in respect to the Ishii model implemented by (Ansys®, 2018b):

$$A_i = \frac{6(1-\alpha_\mathrm{q})min(\alpha_\mathrm{q},\alpha_{\mathrm{q,crit}})}{d_q(1-min(\alpha_\mathrm{q},\alpha_{\mathrm{q,crit}}))} \tag{4-6}$$

Where $\alpha_{q,crit}$ is taken as 0.25.

The drag function f in Equation (4-5) is equal to the product of a drag coefficient by the Reynolds numbers divided by 24. The drag coefficient, CD, is given accordingly to the Ishii model which defines it as the minimum between the drag coefficient for the viscous regime (Equation (4-7)) and the drag coefficient for the distorted regime (Equation (4-8)) (Ansys®, 2018b)

$$\mathrm{C_{D,vis}} = \frac{24}{\mathrm{Re_{part}}}(1+0.15\mathrm{Re_{part}^{0.75}}) \tag{4-7}$$

$$\mathrm{C_{D,dis}} = \frac{2d_q}{3\sqrt{\frac{\sigma}{g(\rho_p-\rho_q)}}} \tag{4-8}$$

With $\mathrm{Re_{part}}$, the particle Reynolds number defined in (4-9) and σ, the surface tension.

$$\mathrm{Re_{part}} = \frac{\rho_p\left|\vec{v}_p-\vec{v}_q\right|d_q}{\mu_q} \tag{4-9}$$

The lift force, $\vec{F}_{lift}$ described in Equation (4-2) is a force that can push the bubbles toward or away from the wall and is given in Equation (4-10) (Ansys®, 2018b).

$$\vec{\mathrm{F}}_{\mathrm{lift}} = -\mathrm{C_{lift}}\alpha_\mathrm{q}\rho_p\left(\vec{v}_p-\vec{v}_q\right)\times(\nabla\times\vec{v}_p) \tag{4-10}$$

Where C_{lift} is the lift coefficient, taken in this simulation as described by Moraga et al. (1999), which depends on the product of the particle Reynolds number and the vorticity Reynolds number given in Equation (4-9) and (4-11), respectively (Ansys®, 2018b).

$$\mathrm{Re}_{\omega} = \frac{\rho_p |\nabla \times \vec{v}_p| d_q^2}{\mu_p} \tag{4-11}$$

The lift coefficient C_{lift} is defined as 0.0767 if the product of the particle and vorticity Reynolds numbers is smaller than 6000, and -0.6353 if this product is higher than $5x10^7$. For values between these two boundaries, the lift coefficient is taken as in Equation (4-12) (Ansys®, 2018b):

$$\mathrm{C_{lift}} = -\left(0.12 - 0.2\mathrm{e}^{\frac{\mathrm{Re_{part}}\mathrm{Re}_{\omega}\times 10^{-5}}{3.6}}\right)\mathrm{e}^{\frac{\mathrm{Re_{part}}\mathrm{Re}_{\omega}\times 10^{-7}}{3}} \tag{4-12}$$

The wall lubrication force, $\vec{F}_{wl}$, described in Equation (4-2) is a force that pushes the bubbles away from the wall and is computed as in Equation (4-13) (Ansys®, 2018b).

$$\vec{\mathrm{F}}_{\mathrm{wl}} = C_{wl}\rho_p\alpha_q|\left(\vec{v}_p - \vec{v}_q\right)_{wall}|^2\vec{n} \tag{4-13}$$

With $|\left(\vec{v}_p - \vec{v}_q\right)_{wall}|$, the phase relative velocity component tangential to the wall surface, $\vec{n}$, the unit vector normal to the wall and pointing away from it, and C_{wl}, a wall lubrication coefficient defined by the closure model from Antal et al. (1991). and given in Equation (4-14) (Ansys®, 2018b):

$$C_{wl} = max\left(0, \frac{\mathrm{C_{w1}}}{d_q} + \frac{\mathrm{C_{w2}}}{y_w}\right) \tag{4-14}$$

With C_{w1} = -0.01 and C_{w2} = 0.05 two non-dimensional coefficients and y_w, the distance to the nearest wall.

The turbulence dispersion force, $\vec{F}_{td}$ in Equation (4-2) tends to push vapor bubble in the main flow stream. It follows the formulation from Lopez de Bertodano given in Equation (4-15) (Ansys®, 2018b):

$$\vec{F}_{td} = \mathrm{C_{TD}}\rho_p k_p \nabla \alpha_{\mathrm{q}} \tag{4-15}$$

With C_{TD} a constant equal to 1 and k, the turbulent kinetic energy.

4.2.2. Turbulence equations

The turbulence is implemented using with the Shear Stress Transport (SST) k – ω model. This model is based on the Reynolds averaged Navier-Stokes equations, in which the time average of the standard Navier-Stokes equations is taken after decomposing the velocity into a time averaged component and a fluctuation component. Doing so results in the appearance of a new variable known as the Reynolds stress. Turbulence model are used to solve this new variable. To do so, in the SST model, two equations (Equations (4-16) and *(4-17)*) are introduced for each phase p. In these equations, q represents the other phase (Ansys®, 2018b).

$$\begin{aligned}\frac{\partial}{\partial t}\left(\alpha_p \rho_p k_p\right) + \nabla\left(\alpha_p \rho_p \vec{U}_p k_p\right) \\ = \nabla\left(\alpha_p\left(\mu_p + \frac{\mu_{t,p}}{\sigma_k}\right)\nabla k_p\right) + \left(\alpha_p G_{k,p} - \alpha_p Y_{k,p}\right) \\ + K_{qp}\left(C_{qp}k_q - C_{pq}k_p\right) - K_{qp}\left(\vec{U}_q - \vec{U}_p\right)\cdot\frac{\mu_{t,q}}{\alpha_q \sigma_q}\nabla\alpha_q \\ + K_{qp}\left(\vec{U}_q - \vec{U}_p\right)\cdot\frac{\mu_{t,p}}{\alpha_p \sigma_p}\nabla\alpha_p + \Pi_{k_p}\end{aligned} \qquad (4\text{-}16)$$

Where μ_t is the turbulent viscosity, G_k is the production of turbulent kinetic energy, Y_k is the dissipation of turbulent kinetic energy, $\vec{U}$ is the time averaged component of the velocity, σ_k is the turbulent Prandtl number for k, and Π_k represents the influence of interphase turbulence interaction.(Ansys®, 2018b, 2018a).

The second equation is defined as:

$$\begin{aligned}\frac{\partial}{\partial t}\left(\alpha_p \rho_p \omega_p\right) + \nabla\left(\alpha_p \rho_p \vec{U}_p \omega_p\right) \\ = \nabla\left(\alpha_p\left(\mu_p + \frac{\mu_{t,p}}{\sigma_\omega}\right)\nabla\omega_p\right) + \left(\alpha_p G_{\omega,p} - \alpha_p Y_{\omega,p}\right) \\ + \frac{\omega_p}{k_p}\left(K_{qp}\left(C_{qp}k_q - C_{pq}k_p\right) - K_{qp}\left(\vec{U}_q - \vec{U}_p\right)\cdot\frac{\mu_{t,q}}{\alpha_q \sigma_q}\nabla\alpha_q\right. \\ \left. + K_{qp}\left(\vec{U}_q - \vec{U}_p\right)\cdot\frac{\mu_{t,p}}{\alpha_p \sigma_p}\nabla\alpha_p\right) + \Pi_{\omega_p}\end{aligned} \qquad (4\text{-}17)$$

where ω is the specific turbulence dissipation rate, G_ω is the generation of ω, Y_ω is the dissipation of ω, and σ_ω is the turbulent Prandtl number for ω (Ansys®, 2018b, 2018a).

For a detailed description of the production and dissipation of k and ω, the turbulent Prandtl numbers as well as turbulent viscosity, the reader is referred to the Chapter 4 of Ansys Fluent Theory guide (Ansys®, 2018a).

In addition to these equations, a turbulence interaction model from Sato & Sekoguchi (1975) is used to account for influence of the dispersed phase on the turbulence equations. Contrarily to other models, in which this influence is given through a source term in the turbulence equations, Sato & Sekoguchi (1975) proposed to include these effect in the velocity decomposition and used the following equation for the kinematic turbulent viscosity of the primary phase p (Ansys®, 2018b).

$$v_p = C_\mu \frac{k^2}{\omega} + 0.6\alpha_q d_q \left|\vec{U}_q - \vec{U}_p\right| \qquad (4\text{-}18)$$

where C_μ is a constant equal to 0.09

4.2.3. Energy Conservation equation

Furthermore, the energy conservation equation also applies (Ansys®, 2018b):

$$\frac{\partial}{\partial t}\left(\alpha_p \rho_p\, h_p\right) + \nabla \cdot \left(\alpha_p \rho_p\, \vec{v}_p h_p\right) = \alpha_p \frac{dP}{dt} + \bar{\tau}_p : \nabla \vec{v}_p - \nabla \cdot \vec{q}_p + S_p + Q_{pex} + \dot{m}_r h_{qp} - \dot{m}_g h_{pq} \qquad (4\text{-}19)$$

With h, the specific enthalpy, q, the heat flux, and Q_{pex}, the intensity of heat exchange between both phase, for which values are opposite from one phase to another. h_{qp} is the interphase enthalpy, defined as the enthalpy of the phase q at the temperature of the phase p.

4.2.4. Heat transfer

The heat transfer is described using the Ranz-Marshall model (Ranz, 1952; Ranz & Marshall, 1952), in which the Nusselt number of a phase p is computed according to Equation (4-20) (Ansys®, 2018b).

$$\mathrm{Nu_p} = 2 + 0.6\mathrm{Re}_{\mathrm{part}}^{0.5}\mathrm{Pr}_{\mathrm{q}}^{\frac{1}{3}} \qquad (4\text{-}20)$$

4.2.5. Wall boiling model

The RPI wall boiling model partitions the heat received from a heating wall into three components, which are the convective heat flux, the quenching heat flux, and the evaporative heat flux (Ansys®, 2018b).

The quenching heat flux is the part of the heat flux driven by the liquid filling the space created by bubble departure. It is given in equation (4-21):

$$q_{quench} = 2\sqrt{\frac{\rho_l c_{P_l} \lambda_l f}{\pi}}(T_w - T_l) \qquad (4\text{-}21)$$

where f is the frequency of bubble departure defined in Equation (4-22),

$$f = \sqrt{\frac{4g(\rho_l - \rho_v)}{3\rho_l D_b}} \qquad (4\text{-}22)$$

D_b is the bubble departure diameter defined according to Kocamustafaogullari & Ishii (1983) in Equation (4-23):

$$D_b = 0.0012\left(\frac{\rho_l - \rho_v}{\rho_v}\right)^{0.9} 0.0208\theta\sqrt{\frac{\sigma}{g(\rho_l - \rho_g)}} \qquad (4\text{-}23)$$

with θ being the contact angle in degree (Ansys®, 2018b).

The evaporative heat flux is the part of the heat flux that is used for the liquid evaporation. It is linked to the volume of the bubble, V_d, the latent heat, L_{heat}, the frequency of bubble departure, f, defined in Equation (4-22), and the active nucleate site density, N_b, which gives the number of site from which bubbles are created and is computed according to Equation (4-24):

$$N_b = \frac{1}{D_b^2} f(\rho^*)\left(\frac{2\mathrm{R_c}}{D_b}\right)^{-4.4} \qquad (4\text{-}24)$$

where R_c is the minimum cavity radius required for bubble generation and is defined as in Equation (4-25) (Ansys®, 2018b):

$$R_c = \frac{2\sigma T_{sat}}{\rho_v L_{heat}(T_{wall} - T_{sat})} \qquad (4\text{-}25)$$

Using (4-24) and (4-25), the evaporative heat flux is expressed as: (Ansys®, 2018b)

$$q_{evap} = V_d N_b \rho_v L_{heat} f \quad (4\text{-}26)$$

Finally, the convective heat flux is the part of the heat flux that is received by the liquid phase moving along the wall. The bubble covered wall area, A_b, does not contribute to this heat transfer, which is therefore expressed as in Equation (4-26)

$$q_{conv} = h_c(T_{wall} - T_l)(1 - A_b) \quad (4\text{-}27)$$

With T_{wall}, the wall temperature, T_l, the liquid temperature and h_c, the single phase heat transfer coefficient (Ansys®, 2018b).

A_b is expressed according to Equation (4-28) :(Ansys®, 2018b)

$$A_b = \min\left(1, \frac{4.8 e^{-\frac{\mathrm{Ja_{TP}}}{80}} N_b \pi D_b^2}{4}\right) \quad (4\text{-}28)$$

Where $\mathrm{Ja_{TP}}$ is the two phase Jacob number defined as:

$$\mathrm{Ja_{TP}} = \frac{\rho_l c_{P_l}(T_{sat} - T_l)}{\rho_v L_{heat}} \quad (4\text{-}29)$$

4.2.6. Solver parameters

4.2.6.1. Time and operating conditions.

Fluent is set to compute the steady state solution of the flow boiling in the duct. Gravity is applied along the inverse of the flow direction. Operating pressure matches the system pressure provided by the experimental data, and the operating density is set to be equal to the vapor density at the saturation temperature. The pressure – velocity coupled method is used, and volume fraction equations are solved independently.

4.2.6.2. Spatial discretization.

In Fluent, the values of the different scalars at the cell faces must be derived from the values computed at the cell centers, which is where spatial discretization schemes are used. Many schemes exist, and, for this simulation, the third order MUSCL spatial discretization is chosen for the momentum turbulent kinetic energy, the specific dissipation rate, and the energy equations, whereas the second order upwind formulation is used for the volume fractions equations (Ansys®, 2018c).

In the third order MUSCL (Monotone Upstream – Centered Schemes for Conservations Laws) scheme, for a scalar ψ, the face value, ψ_f, depends on the upstream cell centered value, ψ_u, as well as the cell centered value of both cells sharing the considered face, noted ψ_0 and ψ_1. Equation (4-30) shows how the face value is computed (Ansys®, 2018c):

$$\psi_f = \theta\left(\frac{1}{2}(\psi_0 + \psi_1) + \frac{1}{2}(\nabla\psi_0 \cdot \vec{r}_0 + \nabla\psi_1 \cdot \vec{r}_1)\right) + (1-\theta)(\psi_u + \nabla\psi_u \cdot \vec{r}_u) \quad (4\text{-}30)$$

With $\vec{r}$ the displacement vector from a cell center toward the cell face. θ is a scalar between 0 and 1, which is internally computed by the solver to prevent a new extremum to appear at cell faces.

The second order upwind scheme is given in Equation (4-31) and only depends on the upstream cell value, ψ_u, its gradient, and the displacement vector $\vec{r}_u$.(Ansys®, 2018c):

$$\psi_f = (\psi_u + \nabla\psi_u \cdot \vec{r}_u) \quad (4\text{-}31)$$

4.2.6.3. Gradients evaluation

The least Squares Cell-based gradient evaluation method is used because of its superior accuracy and low computational cost. The gradient between the values of two consecutive cell centroids c_0 and c_1 at positions r_0 and r_1, respectively follows the Equation (4-32) (Ansys®, 2018c):

$$\nabla\psi_{c_0} \cdot \Delta r = \psi_{c_1} - \psi_{c_0} \quad (4\text{-}32)$$

4.2.7. Boundary conditions

4.2.7.1. Walls and heating surface

All the walls are considered smooth and a no-slip condition is applied. A constant and uniform heat flux is applied at the heating surface, whereas the remaining walls are considered adiabatic.

4.2.7.2. Inlet and outlet

The inlet is situated at a coordinate, z, equal to zero and a constant velocity as well as constant temperature are supplied. A pressure outlet condition is applied at the other end of the duct with a null gauge pressure, and a backflow temperature equal to the inlet temperature. For the inlet and outlet backflow, and

for both phases, the turbulence is given by specifying the hydraulic diameter of the geometry, 0.015 m – 0.008 m in case of ammonia – and an intensity of 4%. The fluid that enters the computational domain is either water or ammonia.

4.3. Result and discussion

4.3.1. Model validation

To compare the computed data to the experimental data from Phillips (2014) and simulation data from Gilman & Baglietto (2017), the wall temperature has been plotted as a function of the wall superheat as shown in Figure 4-4, Figure 4-5, and Figure 4-6. Throughout all the simulated data, the most important difference between the experimental and simulated wall temperature is of 4.1%, whereas this percentage becomes 2.2% in the simulation realized by Gilman & Baglietto (2017). The present model presents the highest difference with the experiment with larger heat fluxes whereas the model of Gilman & Baglietto's (2017) maximum error is located at low heat fluxes, specifically, their model does not provide negative values of the wall superheat; the wall temperature in their simulations is always higher than the saturation temperature. In OTEC, however, the heat flux is rather low and do not exceed 100kW/m^2. By neglecting all values for a heat flux greater than 1000kW/m^2, the maximum difference with the experiment becomes 1.8%, which is obtained at a heat flux of 1000 kW/m^2. Moreover, the increase precision in the low heat flux range compared to the Gilman & Baglietto’s model (2017) can be interesting in the case of an OTEC simulation.

Besides, Gilman & Baglietto's model (2017) uses an experimentally derived density function in its nucleation site density closure model, which cannot be applied with other fluid than water. Another difference between the present model and the one used by Gilman & Baglietto (2017) lies in the bubble departure diameter computation which is based on a force balance applied to the bubble rather than an experimental correlation used in the present model. Doing so they could differentiate sliding bubbles with departing bubbles and apply the different effect they have on the boiling flow.

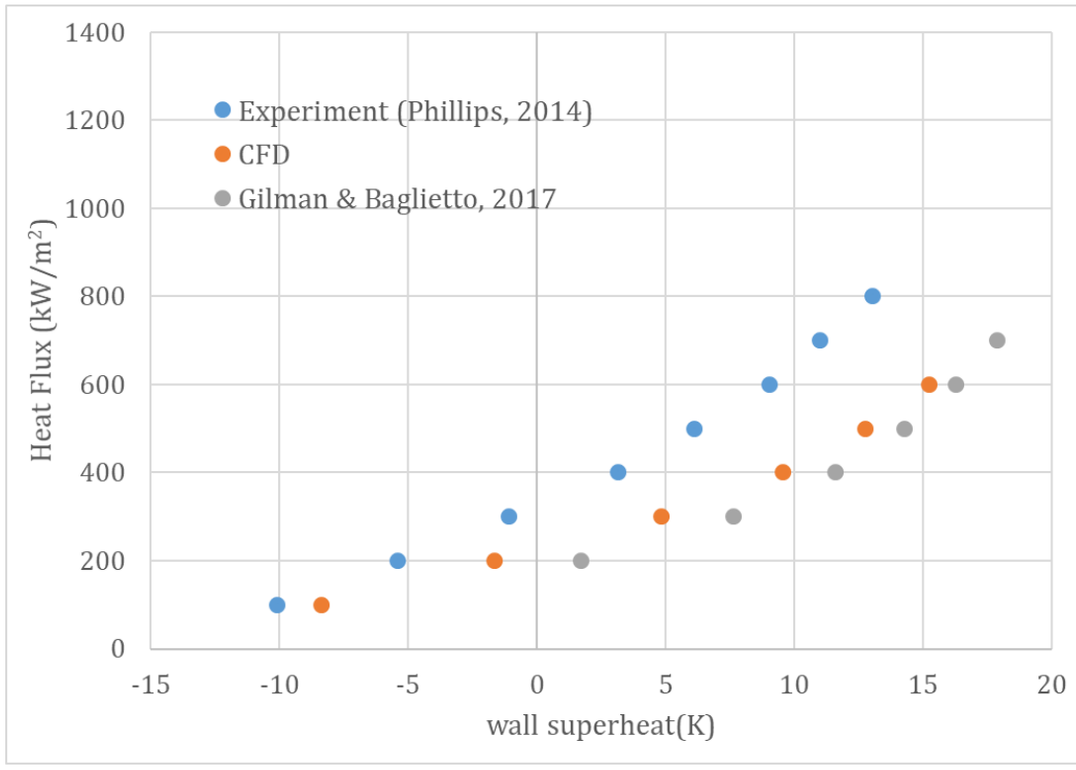

Figure 4-4: Heat flux as a function of the wall superheat for a velocity of 1.0 m/s, a pressure, P = 2 bar, an inlet temperature, T_{in} = 378.36 K and a saturation temperature, T_{sat} = 393.36 K.

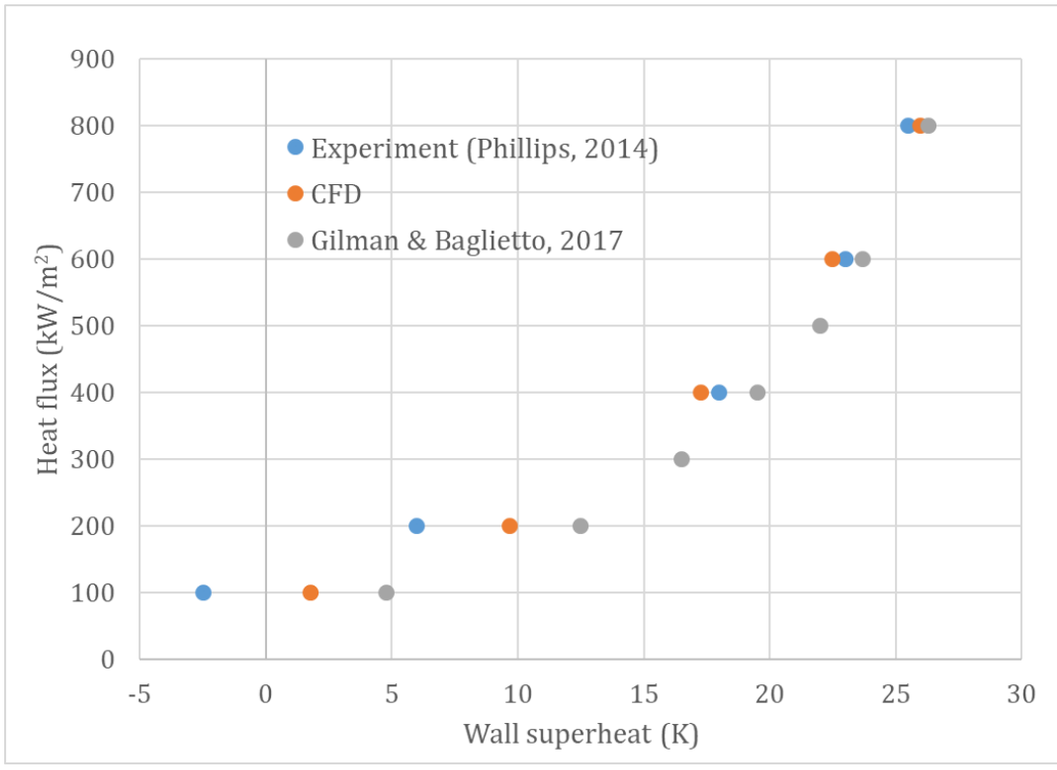

Figure 4-5: Heat flux as a function of the wall superheat for a velocity of 0.5 m/s, a pressure, P = 1.05 bar, an inlet temperature, T_{in} = 364.13 K and a saturation temperature, T_{sat} = 374.13 K.

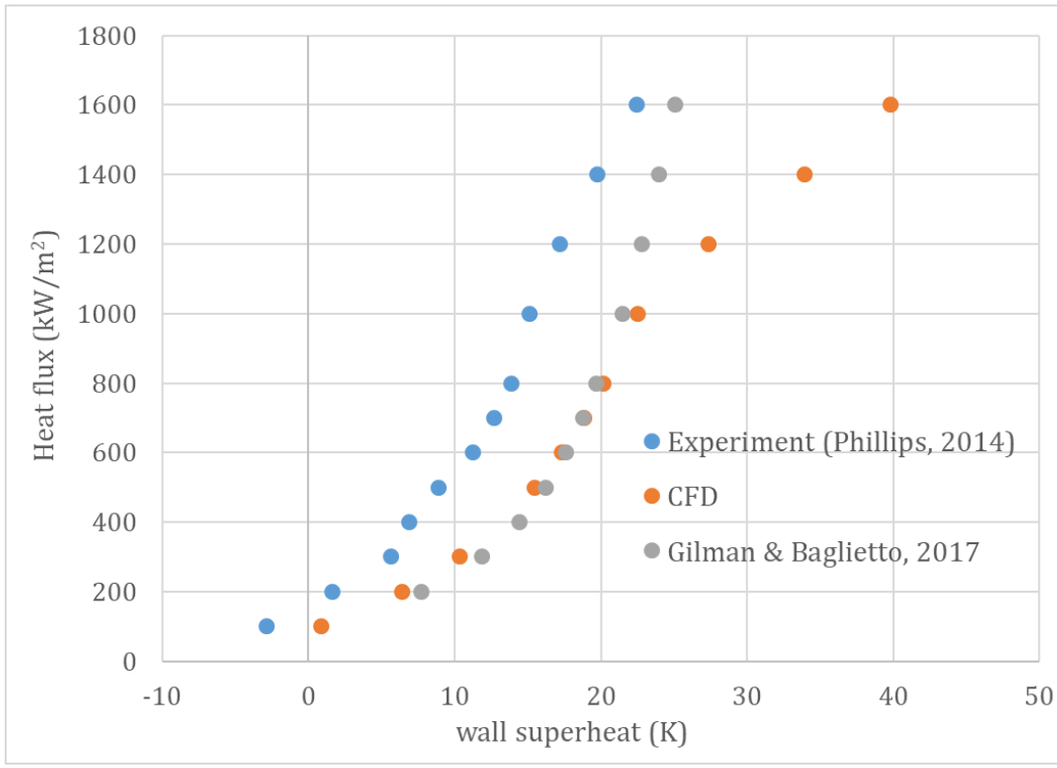

Figure 4-6: Heat flux as a function of the wall superheat for a velocity of 1.25 m/s, a pressure, P = 2 bar, an inlet temperature, T_{in} = 388.36 K and a saturation temperature, T_{sat} = 393.36 K.

4.3.2. Ammonia at OTEC operating conditions

In this section, results of the CFD analysis using ammonia at OTEC operating conditions are given and analyzed. The geometry of the duct is slightly modified to reduce its hydraulic diameter from 15 mm to 8 mm, which is closer to plate heat exchangers values. It should be noted that the model should be improved as its stability was found to decrease, and eventually diverge, as the heat transferred to the fluid increased. This prevented from taking the whole duct length as a heated surface, as it should be the case for heat exchangers. Nonetheless, heat transfer coefficients found with CFD are compared with experimental correlations developed by Amalfi et al. (2016b), Ayub et al. (2019) and Mostinski (1963) which are described in Table 4-1. In this section, the boiling temperature is set to be equal to the inlet temperature, as it is assumed that ammonia enters the heat exchanger at saturation temperature.

Table 4-1: Boiling heat transfer coefficient correlations.

	Correlation
Amalfi et al., (2016b)	$\begin{cases} \mathrm{Nu} = 982\beta^{*1.101}\mathrm{We}^{0.315}\mathrm{Bo}^{0.320}\rho^{*-0.224} & \mathrm{Bd} < 4 \\ \mathrm{Nu} = 18.495\beta^{*0.248}\,\mathrm{Re}_{\mathrm{v}}^{0.135}\mathrm{Re}_{\mathrm{lo}}^{0.351}\mathrm{Bd}^{0.235}\mathrm{Bo}^{0.198}\rho^{*-0.223} & \mathrm{Bd} > 4 \end{cases}$
Ayub et al., (2019)	$\mathrm{Nu} = \left(1.8 + 0.7\frac{\beta}{\beta_{max}}\right)\mathrm{Re}_{\mathrm{eq}}^{0.49-0.3\frac{\sigma}{\sigma_{ammonia}}}\mathrm{Bo}_{\mathrm{eq}}^{-0.2}$ $\mathrm{Re}_{\mathrm{eq}} = \frac{G_{eq}D_h}{\mu_l}$ $\mathrm{Bo}_{\mathrm{eq}} = \frac{q}{G_{eq}L_{heat}}$ and $G_{eq} = G(1 - x + x\rho^*)^{0.5}$
Mostinski, (1963), from Spindler, (2010)	$\alpha = 0.10605P_{cr}^{0.69}q^{0.7}f\left(\frac{P}{P_{cr}}\right)$ $f\left(\frac{P}{P_{cr}}\right) = 1.8\left(\frac{P}{P_{cr}}\right)^{0.17} + 4\left(\frac{P}{P_{cr}}\right)^{1.2} + 10\left(\frac{P}{P_{cr}}\right)^{10}$

P_{cr} being ammonia critical pressure.

The heat transfer coefficient is computed using Equation (4-33). Vapor quality is computed using the volume average of the vapor quality in each cells within the heated part.

$$\alpha = \frac{q}{T_{wall} - T_{in}} \qquad (4\text{-}33)$$

The correlation from Amalfi et al. (2016b) and Ayub et al. (2019) were computed using a chevron angle of 70°. The vapor quality was taken as the mean vapor quality for all the computed mass flux at a given heat flux. The correlation from Mostinski (1963) is for pool boiling and is included here because of the low mass flux at which the simulations were realized. Results are given in Figure 4-7 and Figure 4-8, and boundary conditions for these simulations are given in Table 4-2.

Table 4-2: Boundary conditions for simulated data.

Boundary conditions	Values
G (kg.m^{-2}.s^{-1})	3~12
T_{in} (= T_{evap}) (K)	297.15
q (W.m^{-2})	10000;20000

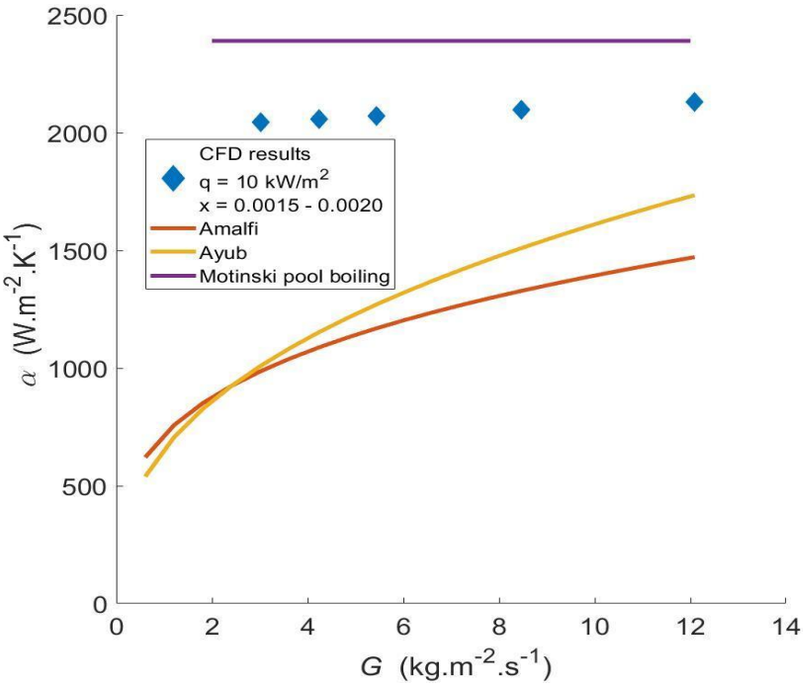

Figure 4-7: Comparison of heat transfer coefficients between CFD results and correlation from the literature at a heat flux q = 10kW/m² and a mean quality of 0.0018.

As seen in the graphs, there is a high discrepancy between CFD results and the correlations. This inconsistency is due to the low heating surface area used in the CFD simulations. With such a small surface, the vapor quality within the heated part remains rather low; around 0.003 for a heat flux of 10 kW/m², which is highly likely to be outside the correlations applicability range. Amalfi et al. (2016b) compared their correlations with experimental data of vapor quality ranging from 0.002 to 0.035 and also found that their correlation highly underestimated the heat transfer coefficient at these low vapor qualities. More specifically, their correlation was found to give heat transfer coefficient values 15% to 40% lower than the experiment on the whole range, with a decreasing accuracy along with the vapor volume fraction. For comparison, their correlation gave a heat transfer coefficient 32% to 46% lower than the presented CFD simulation results using the mean vapor quality of each separate data point, rather than the mean value of all data points. In Figure 4-8, experimental data from Khan et al. (2012) are included as it is the closest match found in the literature in terms of operating conditions, although the saturation and inlet temperatures, as well vapor quality do not match. Further investigation is required, either by conducting experiments with the same

operating conditions of the simulated data or applying the model to conditions matching experimental data.

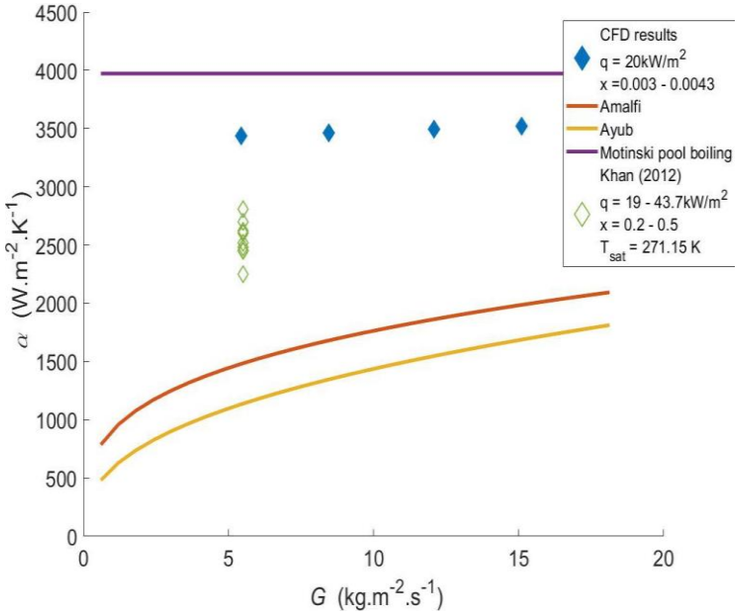

Figure 4-8: Comparison of heat transfer coefficients between CFD results and correlations from the literature at a heat flux q = 20kW/m² and a mean quality of 0.0036.

In addition to the data shown in Figure 4-7 and Figure 4-8, simulations were also made for an inlet temperature of 293.15 K and a heat flux of 10 kW/m². Using all data, it is possible to generate a simple correlation using the inlet velocity, heat flux, and inlet temperature. Indeed, as only ammonia is used in the simulation, and as it is assumed to be at saturation temperature within the whole geometry, fluid properties only depends on the inlet temperature. Also, although the volume fraction has a significant impact on the heat transfer coefficient, it is a function of the mass flux, heat flux, and inlet temperature. More complex correlation can be derived in an attempt to fit data outside of the CFD simulation range, or if good fitting cannot be achieved using the simple correlation.

Assuming that the heat transfer coefficient can be written as the product of a constant times the inlet velocity, heat flux, and inlet temperature at different exponents, a multiple regression analysis can be used to determine the different coefficients. However, poor quality results were achieved and data had to be centered and scaled to provide a good fit. This also presented issues for data point equal to zero after scaling, therefore, an arbitrary scalar value of 1 was added to all centered and scaled variables. Doing so, Equation (4-34) was found:

$$\alpha_{cen,sca} = 1.078 V_{in,cen,sca}^{0.0699} q_{cen,sca}^{0.924} T_{in,cen,sca}^{-0.098} \quad (4\text{-}34)$$

where the subscripts *cen* and *sca* refers to centered and scaled data. Minimums, maximums, means and standards deviations of all variables are given in Table 4-3, and predicted data are plotted against CFD results in Figure 4-9. Minimums and maximums in Table 4-3 refers to those of the centered variables.

Table 4-3: Mean, standard deviation, minimum and maximum of variable used in the correlation.

Variable	Mean	Standard deviation	Minimum	Maximum
v_{in} (m.s^{-1})	0.0132	0.0065	-1.26	1.82
q (kW.m^{-2})	13.08	4.80	-0.64	1.44
T_{in} (K)	295.9	1.92	-1.44	0.64
α (kW.m^{-2}.K^{-1})	2.55	650.62	-0.77	1.50

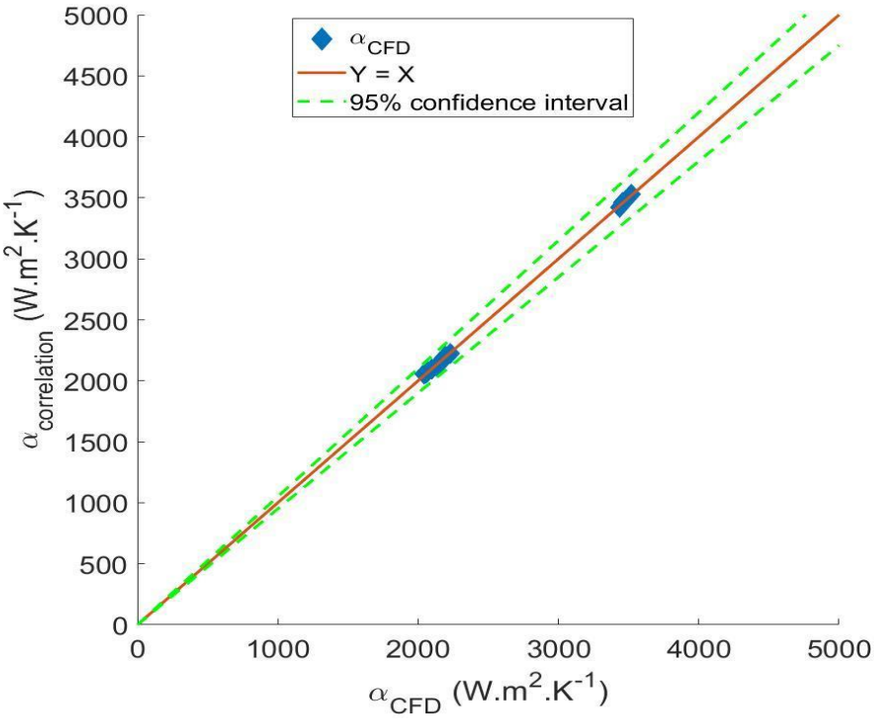

Figure 4-9: Predicted heat transfer coefficient against heat transfer coefficients computed using CFD.

Although a good fit has been achieved, it must be noted that the number of data points are rather scarce, and more simulations points should be simulated using CFD to get a more reliable correlation. Specifically, these data only contain

two heat flux values – 10 kW/m² and 20 kW/m² – and two inlet temperatures – 297.15 K and 293.15 K – which might not be enough to generate a reliable correlation. It should also be noted that increasing the number of simulation points might require a more complex fitting model to properly describe the heat transfer coefficient.

4.4. Conclusion

The main goal of this chapter was to show the possibility of using Computational Fluid Dynamins to compute correlations that can be used for an accurate optimization of various heat exchanger geometries.

- A simple flow boiling model was developed and was successful at predicting wall temperature at low enough heat fluxes using a small heating surface on a vertical duct with water as the fluid.
- The model was applied to a similar geometry using OTEC heat flux, inlet velocities, and ammonia. Data were compared to correlations from the literature but showed poor agreement due to the low volume fraction achieved using such a small heating surface as correlations were found to greatly underestimate heat flux at such low volume fraction. Moreover, it was found that the model requires further refinement as the stability decreased together with the increase of the amount of heat transferred to the fluid, thus, simulation with larger heating surface, and, therefore, larger vapor volume fraction could not be achieved.
- A simple method for computing a fairly accurate correlation from CFD results was demonstrated, although more simulation data points are required to get a reliable correlation.

Many obstacle remains for accurately derive a boiling heat transfer coefficient correlation using CFD results. However, by taking a large enough sample to cover the range that can occur in the optimization of the previous chapter, coupled with more accurate flow boiling model, it is possible, for each heat exchanger, to provide a simple, yet accurate correlation to be used in the

optimization. This has a great importance for the accurate comparison of OTEC performance based on heat exchanger geometry.

Chapter 5.

CONCLUSION

This chapter presents the goal of this study, a summary of the different achievements realized in this thesis, as well as future research objective in the OTEC optimization field regarding heat exchangers.

5.1. Goal and achievements

Given the high computational cost of standard computation methods, the lack of studies concerning optimal plate heat exchanger geometry, and the high dependency

on experimental data for accurate prediction of heat transfer coefficient and pressure drop, this thesis had three goals:

- The simplification of the optimization process considering both fluids heat transfer coefficients and pressure drops.
- The optimization of heat exchanger design parameters for a maximum net power output to heat transfer area ratio.
- Showcase the possibility of obtaining accurate boiling heat transfer coefficients using CFD.

First, using seawater side heat transfer coefficient and pressure drop correlations of a given heat exchanger, a simplified method for computing and maximizing the net power output to heat exchanger surface area ratio was achieved. This allowed for the comparison of the performances of an OTEC system using different heat exchangers. Results clearly showed the importance of the heat exchanger selection as the net power output by unit of heat exchanger area was more than doubled from the least suitable heat exchanger to the most suitable one, just among the three tested in this study. The importance of finding the best trade-off between heat transfer coefficient and pressure drop was also highlighted. Moreover, it was pointed out that some heat exchangers' characteristics beyond the scope of the optimization could play a role in the heat exchanger selection. Indeed, heat exchangers with high heat transfer coefficients and high pressure drop were find to require a smaller mass flow rate, and, thus, smaller pipes diameters to achieve the optimum OTEC performance.

Then, the method accuracy was improved by including the working fluid side heat transfer coefficient and pressure drop correlations, which led to values that were almost halved compared to what was found when only considering seawater side, but closer to what was found in the literature. Global correlations were also introduced to allow for a comparison of different heat exchangers design parameters. Consequently, the effect of chevron angle, mean channel spacing, corrugation pitch, and length to width ratio on the net power output per unit of heat exchanger area

were investigated. The optimization of the OTEC system using heat exchangers with optimum design parameters was realized, and it was found that OTEC performances were increased as chevron angles got closer to 70° and 68° for the evaporator and condenser, respectively. Regarding mean channel spacing and corrugation pitch, the combination that led to the highest enlargement factor in the condenser was found to lead to the highest OTEC performances whereas for the evaporator, the combination leading to smallest enlargement factor was found to be more suitable. Finally, no optimum aspect ratios were found, as the net power output to heat transfer area ratio seemed to increase along with the aspect ratio without limits. Further investigations are required as a finite length is needed to drive the heat transfer.

Despite the overall greater accuracy, the method was found to be limited by the global correlations accuracy as well as their applicability. Knowing this, and as using heat exchanger specific experimental correlations would not be easily achievable, the last achievement of this thesis was to show the possibility of using CFD to compute boiling heat transfer coefficient correlations to be used in the optimization. A rather simple model to compute water flow boiling was used and compared with experimental and simulation data. It was then applied to ammonia flow boiling at OTEC conditions. While water results, except at very high heat fluxes, showed good agreement with literature data, a rather significant discrepancy was found using ammonia, mainly due to a low volume fraction that was achieved with the tested geometry. Nonetheless, it was shown that CFD results could be used to derive simple heat exchanger specific heat transfer coefficient correlations of great accuracy, provided that a more accurate flow boiling model can be achieved.

5.2. Future research recommendations

Considering this thesis work, two main research axis should be investigated. The first axis would be to focus on developing further CFD simulations, while the other consists in improving optimization and cycle analysis.

5.2.1. CFD investigations

The work presented in this thesis merely points out the possibility and potential of using CFD simulation to derive heat exchangers characteristics. The model developed in this work was found to rapidly decrease in stability and eventually diverged as the volume fraction increased, making it impossible to simulate an actual corrugated plate heat exchanger heated through the whole surface. Moreover, pressure drop was largely underestimated by the simulations. A more robust model capable of accurately predict both the heat transfer coefficient and pressure drop need to be developed. From there, the effect of a non-uniform heat flux, as it is the case in OTEC system, should also be investigated. The condensation heat transfer coefficient and pressure drop should be investigated in the same fashion. It is highly important to be able to rely on accurate CFD analysis so that a wide range of geometries can be tested for OTEC applications.

5.2.2. Optimization and cycle analysis

In this work the objective function was defined as the net power output to heat exchanger surface area ratio. Switching to the Levelized Cost Of Energy or any other relevant economic indicator as the objective function could be a great improvement and more appealing to industries. Such an optimization needs to consider, in addition to what was provided in this work, the cost of the different components according to the heat exchangers characteristics and optimum operating point. This includes the price of seawater pipes, for which the length can vary significantly depending on the site. Moreover, as stated in Chapter 1, the most suitable closed cycle for OTEC has not been clearly identified yet. An optimization of all cycles, considering heat transfer coefficients and pressure drops of both fluids is essential for the future of OTEC technology.

REFERECENCES

1990 -2019 The MathWorks, Inc. (n.d.). *Matlab*®.

Amalfi, R. L., Vakili-Farahani, F., & Thome, J. R. (2016a). Flow boiling and frictional pressure gradients in plate heat exchangers. Part 1: Review and experimental database. *International Journal of Refrigeration*, *61*, 166–184. https://doi.org/10.1016/j.ijrefrig.2015.07.010

Amalfi, R. L., Vakili-Farahani, F., & Thome, J. R. (2016b). Flow boiling and frictional pressure gradients in plate heat exchangers. Part 2: Comparison of literature methods to database and new prediction methods. *International Journal of Refrigeration*, *61*, 185–203. https://doi.org/10.1016/j.ijrefrig.2015.07.009

Amano, M., & Tanaka, T. (2006). Open-cycle OTEC systems with freshwater product: Effects of noncondensable gases on performance of condenser. *Electrical Engineering in Japan*, *154*(1), 29–35. https://doi.org/10.1002/eej.20179

Anowar Hossain, Md., Onaka, Y., Afroz, H. M. M., & Miyara, A. (2013). Heat transfer during evaporation of R1234ze(E), R32, R410A and a mixture of R1234ze(E) and R32 inside a horizontal smooth tube. *International Journal of Refrigeration*, *36*(2), 465–477. https://doi.org/10.1016/j.ijrefrig.2012.10.009

Ansys®. (2018a). *Academic Research Fluent, release 19.1, Help System, Fluent Theory Guide, Chapter 4, Turbulence*. Ansys Inc.

Ansys®. (2018b). *Academic Research Fluent, release 19.1, Help System, Fluent Theory Guide, Chapter 17, Multiphase flow*. Ansys inc.

Ansys®. (2018c). *Academic Research Fluent, release 19.1, Help System, Fluent Theory Guide, Chpater 21, Solver Theory*. Ansys inc.

Antal, S. P., Lahey, R. T., & Flaherty, J. E. (1991). Analysis of phase distribution in fully developed laminar bubbly two-phase flow. *International Journal of Multiphase Flow*, *17*(5), 635–652. https://doi.org/10.1016/0301-9322(91)90029-3

AREVA NP et Tranter, Inc. Associent leur expertise pour le remplacement des échangeurs thermiques dans les installations nucléaires. (2017, September 12). framatome. https://www.framatome.com/FR/businessnews-750/areva-np-et-tranter-inc-associent-leur-expertise-pour-le-remplacement-des-exhangeurs-thermiques-dans-les-installations-nucleaires.html

Avery, W. H., & Wu, C. (1994). Introduction and overview. In *Renewable Energy from the Ocean. A Guide to OTEC*. Oxford university Press.

Ayub, Z. H., Khan, T. S., Salam, S., Nawaz, K., Ayub, A. H., & Khan, M. S. (2019). Literature survey and a universal evaporation correlation for plate type heat exchangers. *International Journal of Refrigeration*, *99*, 408–418. https://doi.org/10.1016/j.ijrefrig.2018.09.008

Azzolin, M., Berto, A., Bortolin, S., & Del Col, D. (2017). Heat transfer degradation during condensation of non-azeotropic mixtures. *Journal of Physics: Conference Series*, *923*, 012017. https://doi.org/10.1088/1742-6596/923/1/012017

Bartolemej, C. G., & Chanturiya, V. M. (1967). Experimental study of true void fraction when boiling subcooled water in vertical tubes. *Thermal Engineering*, *14*, 123–128.

Bernardoni, C., Binotti, M., & Giostri, A. (2019). Techno-economic analysis of closed OTEC cycles for power generation. *Renewable Energy*, *132*, 1018–1033. https://doi.org/10.1016/j.renene.2018.08.007

Braz Filho, F. A., Ribeiro, G. B., & Caldeira, A. D. (2016). Prediction of subcooled flow boiling characteristics using two-fluid Eulerian CFD model. *Nuclear Engineering and Design*, *308*, 30–37. https://doi.org/10.1016/j.nucengdes.2016.08.016

Chih Wu. (1987). A Performance Bound for Real OTEC Heat Engines. *Ocean Engineering*, *14*(4), 349–354. https://doi.org/10.1016/0029-8018(87)90032-1

Colombo, M., & Fairweather, M. (2016). Accuracy of Eulerian–Eulerian, two-fluid CFD boiling models of subcooled boiling flows. *International Journal of Heat and Mass Transfer*, *103*, 28–44. https://doi.org/10.1016/j.ijheatmasstransfer.2016.06.098

Colombo, M., Thakrar, R., Fairweather, M., & Walker, S. P. (2019). Assessment of semi-mechanistic bubble departure diameter modelling for the CFD simulation of boiling flows. *Nuclear Engineering and Design*, *344*, 15–27. https://doi.org/10.1016/j.nucengdes.2019.01.014

d'Arsonval, A. (1881). Utilisation des forces naturelles. Avenir de l'électricité. *La Revue Scientifique de La France et de l'étranger*, *12*, 370–372.

Dijoux, A., Sinama, F., Marc, O., & Clauzade, B. (2017). *1 Working fluid selection general method and sensitivity analysis of an 2 Organic Rankine Cycle (ORC): Application to Ocean Thermal Energy 3 Conversion (OTEC)*.

E. W. Lemmon, I. H. Bell, M. L. Huber, & M. O. McLinden. (2018). *NIST Standard Reference Database 23: Reference Fluid Thermodynamic and Transport Properties-REFPROP, Version 10.0, National Institute of Standards and Technology*.

ETM : La centrale NEMO développée en Martinique est mise en Stand by. (2018, April 4). https://www.energiesdelamer.eu/. https://www.energiesdelamer.eu/2018/04/04/etm/

Frank P. Incropera, David P. DeWitt, Theodore L. Bergman, & Adrienne S. Lavine. (2006a). Boiling and Condensation. In *Fundamentals of Heat and Mass Transfer* (6th ed., pp. 619–668). John Wiley & Sons.

Frank P. Incropera, David P. DeWitt, Theodore L. Bergman, & Adrienne S. Lavine. (2006b). Heat exchangers. In *Fundamentals of Heat and Mass Transfer* (6th ed., pp. 669–722). John Wiley & Sons.

Garnier, J., Manon, E., & Cubizolles, G. (2001). Local measurements on flow boiling of refrigerant 12 in a vertical tube. *Multiphase Science and Technology*, *13*, 1–111.

Gilman, L., & Baglietto, E. (2017). A self-consistent, physics-based boiling heat transfer modeling framework for use in computational fluid dynamics. *International Journal of Multiphase Flow*, *95*, 35–53. https://doi.org/10.1016/j.ijmultiphaseflow.2017.04.018

Hibiki, T., & Ishii, M. (2003). Active nucleation site density in boiling systems. *International Journal of Heat and Mass Transfer*, *46*(14), 2587–2601. https://doi.org/10.1016/S0017-9310(03)00031-0

Ikegami, Y., Yasunaga, T., & Morisaki, T. (2018). Ocean Thermal Energy Conversion Using Double-Stage Rankine Cycle. *Journal of Marine Science and Engineering*, *6*(1), 21. https://doi.org/10.3390/jmse6010021

Johnson, D. (1983). The exergy of the ocean thermal resource and analysis of second-law efficiencies of idealized ocean thermal energy conversion power cycles. *Energy*, *8*(12), 927–946. https://doi.org/10.1016/0360-5442(83)90092-0

Kalina Alexanfer I. (1982). *Generation of energy by means of a working fluid, and regeneration of a working fluid* (Patent No. US 4346561).

Khan, M. S., Khan, T. S., Chyu, M.-C., & Ayub, Z. H. (2012). Experimental investigation of evaporation heat transfer and pressure drop of ammonia in a 30° chevron plate heat exchanger. *International Journal of Refrigeration*, *35*(6), 1757–1765. https://doi.org/10.1016/j.ijrefrig.2012.05.019

Klausner, J. F., Mei, R., Bernhard, D. M., & Zeng, L. Z. (1993). Vapor bubble departure in forced convection boiling. *International Journal of Heat and Mass Transfer*, *36*(3), 651–662. https://doi.org/10.1016/0017-9310(93)80041-R

Kocamustafaogullari, G., & Ishii, M. (1983). Interfacial area and nucleation site density in boiling systems. *International Journal of Heat and Mass Transfer*, *26*(9), 1377–1387. https://doi.org/10.1016/S0017-9310(83)80069-6

Končar, B., & Matkovič, M. (2012). Simulation of turbulent boiling flow in a vertical rectangular channel with one heated wall. *Nuclear Engineering and Design*, *245*, 131–139. https://doi.org/10.1016/j.nucengdes.2012.01.013

Krepper, E., & Rzehak, R. (2011). CFD for subcooled flow boiling: Simulation of DEBORA experiments. *Nuclear Engineering and Design*, *241*(9), 3851–3866. https://doi.org/10.1016/j.nucengdes.2011.07.003

Kushibe, M., & Ikegami, Y. (2006). EVAPORATION HEAT TRANSFER OF AMMONIA AND PRESURE DROP OF WARM WATER FOR PLATE TYPE EVAPORATOR. *RENEWABLE ENERGY*, 2.

Li, X., Wang, R., Huang, R., & Shi, Y. (2006). Numerical investigation of boiling flow of nitrogen in a vertical tube using the two-fluid model. *Applied Thermal Engineering*, *26*(17–18), 2425–2432. https://doi.org/10.1016/j.applthermaleng.2006.02.011

Makai Ocean Engineering. (n.d.). Retrieved November 23, 2021, from https://www.makai.com/ocean-thermal-energy-conversion/

Manon, E. (2000). *Contribution à l'analyse et à la modélisation locale des écoulements boillants sous-saturés dans les conditions des Réacteurs à Eau sous Pression.* Ecole Centrale Paris.

Martin, B., Okamura, S., Nakamura, Y., Yasunaga, T., & Ikegami, Y. (2016). Status of the "Kumejima Model" for advanced deep seawater utilization. *2016 Techno-Ocean (Techno-Ocean)*, 211–216. https://doi.org/10.1109/Techno-Ocean.2016.7890648

Massachusetts Institute of Technology. (2016). *SEAWATER properties Software* (3.1.2) [Computer software]. http://web.mit.edu/seawater/

MathWorks®. (n.d.). *Constrained Nonlinear Optimization Algorithms*. https://fr.mathworks.com/help/optim/ug/constrained-nonlinear-optimization-algorithms.html#f26965

Moraga, F. J., Bonetto, F. J., & Lahey, R. T. (1999). Lateral forces on spheres in turbulent uniform shear ¯ow. *International Journal of Multiphase Flow*, 52.

Morisaki, T., & Ikegami, Y. (2013). Performance Evaluation of Heat Exchangers in OTEC Using Ammonia/Water Mixture as Working Fluid. *Open Journal of Fluid Dynamics*, *03*(04), 302–310. https://doi.org/10.4236/ojfd.2013.34037

Mostinski, I. L. (1963). Application of the rule of corresponding states for calculation of heat transfer and critical heat flux. *Teploenergetika*, *4*, 66–71.

Muley, A., & Manglik, R. M. (1999). Experimental Study of Turbulent Flow Heat Transfer and Pressure Drop in a Plate Heat Exchanger With Chevron Plates. *Journal of Heat Transfer*, *121*(1), 110–117. https://doi.org/10.1115/1.2825923

Nayar, K. G., Sharqawy, M. H., Banchik, L. D., & Lienhard V, J. H. (2016). Thermophysical properties of seawater: A review and new correlations that include pressure dependence. *Desalination*, *390*, 1–24. https://doi.org/10.1016/j.desal.2016.02.024

Nemitallah, M. A., Habib, M. A., Ben Mansour, R., & El Nakla, M. (2015). Numerical predictions of flow boiling characteristics: Current status, model setup and CFD modeling for different non-uniform heating profiles. *Applied Thermal Engineering*, *75*, 451–460. https://doi.org/10.1016/j.applthermaleng.2014.09.036

Nilpueng, K., & Wongwises, S. (2010). Two-phase gas–liquid flow characteristics inside a plate heat exchanger. *Experimental Thermal and Fluid Science*, *34*(8), 1217–1229. https://doi.org/10.1016/j.expthermflusci.2010.05.001

O. M. Ibrahim, S. A. Klein, & J. M. Mitchell. (1992). Effects of Irreversibility and Economics on the Performance of a Heat Engine. *Journal of Solar Energy Engineering*, *114*, 267–271.

Phillips, B. A. (2014). *Experimental Investigation of Subcooled Flow Boiling Using Synchronized High Speed Video, Infrared Thermography, and Particle Image Velocimetry*.

Rajagopalan, K., & Nihous, G. C. (2013a). Estimates of global Ocean Thermal Energy Conversion (OTEC) resources using an ocean general circulation model. *Renewable Energy*, *50*, 532–540. https://doi.org/10.1016/j.renene.2012.07.014

Rajagopalan, K., & Nihous, G. C. (2013b). An Assessment of Global Ocean Thermal Energy Conversion Resources With a High-Resolution Ocean General Circulation Model. *Journal of Energy Resources Technology*, *135*(4), 041202. https://doi.org/10.1115/1.4023868

Ranz, W. E. (1952). Evaporation From drops, part II. *Chemical Engineering Progress*, *48*, 173–180.

Ranz, W. E., & Marshall, W. R. (1952). Evaporation From Drop, Part I. *Chemical Engineering Progress*, *48*(3), 141–146.

Roche, S. (2018). « L'énergie thermique des mers dans les Outre-mer français: Un enjeu stratégique de territoire? ». *Études caribéennes (Online)*, *1*. https://doi.org/10.4000/etudescaribeennes.11971 [in French]

Sato, Y., & Sekoguchi, K. (1975). LIQUID VELOCITY DISTRIBUTION IN TWO-PHASE BUBBLE FLOW. *International Journal of Multiphase Flow*, *2*, 79–95.

Seungtaek, L., Hosaeng, L., Junghyun, M., & Hyeonju, K. (2020). Simulation Data of Regional Economic Analysis of OTEC for Applicable Area. *Processes*, *8*(9), 1107. https://doi.org/10.3390/pr8091107

Sharqawy, M. H., Lienhard, J. H., & Zubair, S. M. (2010). Thermophysical properties of seawater: A review of existing correlations and data. *Desalination and Water Treatment*, *16*(1–3), 354–380. https://doi.org/10.5004/dwt.2010.1079

Sinama, F., Martins, M., Journoud, A., Marc, O., & Lucas, F. (2015). Thermodynamic analysis and optimization of a 10MW OTEC Rankine cycle in Reunion Island with the equivalent Gibbs system method and generic optimization program GenOpt. *Applied Ocean Research*, *53*, 54–66. https://doi.org/10.1016/j.apor.2015.07.006

Solotych, V., Lee, D., Kim, J., Amalfi, R. L., & Thome, J. R. (2016). Boiling heat transfer and two-phase pressure drops within compact plate heat exchangers: Experiments and flow visualizations. *International Journal of Heat and Mass Transfer*, *94*, 239–253. https://doi.org/10.1016/j.ijheatmasstransfer.2015.11.037

Spindler, K. (2010). Overview and discussion on pool boiling heat transfer data and correlations of ammonia. *International Journal of Refrigeration*, *33*(7), 1292–1306. https://doi.org/10.1016/j.ijrefrig.2010.06.012

Sun, F., Ikegami, Y., Jia, B., & Arima, H. (2012). Optimization design and exergy analysis of organic rankine cycle in ocean thermal energy conversion. *Applied Ocean Research*, *35*, 38–46. https://doi.org/10.1016/j.apor.2011.12.006

Takahashi, M. M. (2000). Ocean Water and Its Wonderful Potential. In *DOW Deep Ocean Water as Our Next Natural Resource* (pp. 9–30). Terra Scientific Publishing Company.

Tao, X., Dahlgren, E., Leichsenring, M., & Ferreira, C. A. I. (2020). NH3 condensation in a plate heat exchanger: Experimental investigation on flow patterns, heat transfer and frictional pressure drop. *International Journal of Heat and Mass Transfer*, *151*, 119374. https://doi.org/10.1016/j.ijheatmasstransfer.2020.119374

Tao, X., & Ferreira, C. A. I. (2019). Heat transfer and frictional pressure drop during condensation in plate heat exchangers: Assessment of correlations and a new method. *International Journal of Heat and Mass Transfer*, *135*, 996–1012. https://doi.org/10.1016/j.ijheatmasstransfer.2019.01.132

Tao, X., & Ferreira, C. A. I. (2020). NH3 condensation in a plate heat exchanger: Flow pattern based models of heat transfer and frictional pressure drop. *International Journal of Heat and Mass Transfer*, *154*, 119774. https://doi.org/10.1016/j.ijheatmasstransfer.2020.119774

Thakrar, R., Murallidharan, J., & Walker, S. P. (2017). CFD investigation of nucleate boiling in non-circular geometries at high pressure. *Nuclear Engineering and Design*, *312*, 410–421. https://doi.org/10.1016/j.nucengdes.2016.08.020

Uehara, H., & Ikegami, Y. (1990). Optimization of a Closed-Cycle OTEC System. *Journal of Solar Energy Engineering*, *112*, 247–256.

Uehara, H., Ikegami, Y., & Nishida, T. (1995). OTEC System Using a New Cycle With Absorption and Extraction Process. *Physical Chemistry of Aqueous Systems: Meeting the Needs of Industry*, 862–869.

Utilizing deep sea water in remote island areas. Regional revitalization feasibility study. (Translated). (2017). Okinawa General Bureau Cabinet Office. http://www.gosea.info/en/infomation/dswusefs/

VanZwieten, J. H., Rauchenstein, L. T., & Lee, L. (2017). An assessment of Florida's ocean thermal energy conversion (OTEC) resource. *Renewable and Sustainable Energy Reviews*, *75*, 683–691. https://doi.org/10.1016/j.rser.2016.11.043

Wu, Z., Feng, H., Chen, L., & Ge, Y. (2020). Performance Optimization of a Condenser in Ocean Thermal Energy Conversion (OTEC) System Based on Constructal Theory and

a Multi-Objective Genetic Algorithm. *Entropy*, *22*(6), 641. https://doi.org/10.3390/e22060641

Wu, Z., Feng, H., Chen, L., Tang, W., Shi, J., & Ge, Y. (2020). Constructal thermodynamic optimization for ocean thermal energy conversion system with dual-pressure organic Rankine cycle. *Energy Conversion and Management*, *210*, 112727. https://doi.org/10.1016/j.enconman.2020.112727

Wu, Z., Feng, H., Chen, L., Xie, Z., & Cai, C. (2019). Pumping power minimization of an evaporator in ocean thermal energy conversion system based on constructal theory. *Energy*, *181*, 974–984. https://doi.org/10.1016/j.energy.2019.05.216

Yasunaga, T., Noguchi, T., Morisaki, T., & Ikegami, Y. (2018). Basic Heat Exchanger Performance Evaluation Method on OTEC. *Journal of Marine Science and Engineering*, *6*(2), 32. https://doi.org/10.3390/jmse6020032

Yasuyuki Ikegami & Adrian Bejan. (1998). On the thermodynamic Optimization of Power Plants With Fluid Transfer and Fluid Flow Irreversabilities. *ASME Journal of Solar Energy Engineering*, *120*, 139–144.

Yeh, R.-H., Su, T.-Z., & Yang, M.-S. (2005). Maximum output of an OTEC power plant. *Ocean Engineering*, *32*(5–6), 685–700. https://doi.org/10.1016/j.oceaneng.2004.08.011

Yeoh, G. H., Vahaji, S., Cheung, S. C. P., & Tu, J. Y. (2014). Modeling subcooled flow boiling in vertical channels at low pressures – Part 2: Evaluation of mechanistic approach. *International Journal of Heat and Mass Transfer*, *75*, 754–768. https://doi.org/10.1016/j.ijheatmasstransfer.2014.03.017

Yun, B.-J., Splawski, A., Lo, S., & Song, C.-H. (2012). Prediction of a subcooled boiling flow with advanced two-phase flow models. *Nuclear Engineering and Design*, *253*, 351–359. https://doi.org/10.1016/j.nucengdes.2011.08.067

Zhang, X., He, M., & Zhang, Y. (2012). A review of research on the Kalina cycle. *Renewable and Sustainable Energy Reviews*, *16*(7), 5309–5318. https://doi.org/10.1016/j.rser.2012.05.040